

A NUMERICAL STUDY ON DEPENDENT ABSORPTION AND SCATTERING BY
INTERACTING NANO-SIZED PARTICLES

A THESIS SUBMITTED TO
THE GRADUATE SCHOOL OF NATURAL AND APPLIED SCIENCES
OF
MIDDLE EAST TECHNICAL UNIVERSITY

BY

FATMA NAZLI DÖNMEZER

IN PARTIAL FULFILLMENT OF THE REQUIREMENTS
FOR
THE DEGREE OF MASTER OF SCIENCE
IN
MECHANICAL ENGINEERING

JUNE 2009

Approval of the thesis:

**A NUMERICAL STUDY ON DEPENDENT ABSORPTION AND SCATTERING BY
INTERACTING NANO-SIZED PARTICLES**

submitted by **FATMA NAZLI DÖNMEZER** in partial fulfillment of the requirements for the degree of
Master of Science in Mechanical Engineering Department, Middle East Technical University by,

Prof. Dr. Canan Özgen
Dean, Graduate School of **Natural and Applied Sciences**

Prof. Dr. Süha Oral
Head of Department, **Mechanical Engineering**

Assist. Prof. Dr. Tuba Okutucu
Supervisor, **Mechanical Engineering, METU**

Prof. Dr. Pınar Mengüç
Co-supervisor, **Mechanical Engineering, Özyeğin University**

Examining Committee Members:

Prof. Dr. Faruk Arınç
Mechanical Engineering, METU

Assist. Prof. Dr. Tuba Okutucu
Physics Department, METU

Prof. Dr. Pınar Mengüç
Mechanical Engineering, Özyeğin Üniversitesi

Prof. Dr. Raşit Turan
Mechanical Engineering, METU

Assist. Prof. Dr. İlker Tari
Mechanical Engineering, METU

Date:

I hereby declare that all information in this document has been obtained and presented in accordance with academic rules and ethical conduct. I also declare that, as required by these rules and conduct, I have fully cited and referenced all material and results that are not original to this work.

Name, Last Name: FATMA NAZLI DÖNMEZER

Signature :

ABSTRACT

A NUMERICAL STUDY ON DEPENDENT ABSORPTION AND SCATTERING BY INTERACTING NANO-SIZED PARTICLES

DÖNMEZER, FATMA NAZLI

M.S., Department of Mechanical Engineering

Supervisor : Assist. Prof. Dr. Tuba Okutucu

Co-Supervisor : Prof. Dr. Pinar Mengüç

June 2009, 99 pages

Understanding and manipulating nanosized particles is crucial for the advancement of nanotechnology research. Dependent light scattering of noble metals can be used to achieve new material responses that can be used in different applications. Dependent light scattering of nanoparticles allows the understanding of orientation and location of closely positioned particles. Besides, dependently scattering metallic particles create significantly enhanced near fields and high absorption rates when excited at their plasmon resonance. It is used for spectrally selective heating and melting of nanosized particles as a nanomanufacturing method. With numerical methods dependent scattering properties of particles can be obtained. In this study, the dependent optical absorption efficiencies of metallic nanoparticles are obtained with the newly developed Integrated Poynting Vector Approach (IPVA). This is used in conjunction with a numerical light scattering solution tool DDSCAT. Results indicate that IPVA and DDSCAT together can be used for the estimation of scattering and absorption of nanoparticles affected by the near field of other particles in their close vicinity. The method is suggested to be suitable for the understanding of physical mechanisms behind dependent scattering prior to experiments that require lots of effort and resources.

Keywords: Surface plasmon, gold nanoparticles, dependent scattering, DDSCAT, nanomanufacturing

ÖZ

NANO BOYUTLU PARÇACIKLARIN ETKİLEŞİMLİ SAÇILIM VE EMİLİM ÖZELLİKLERİNİN NÜMERİK OLARAK İNCELENMESİ

DÖNMEZER, FATMA NAZLI

Yüksek Lisans, Makina Mühendisliği Bölümü

Tez Yöneticisi : Y. Doç. Dr. Tuba Okutucu

Ortak Tez Yöneticisi : Prof. Dr. Pınar Mengüç

Haziran 2009, 99 sayfa

Nanoboyutlu parçacıkların anlaşılması ve işlenmesi nanoteknoloji araştırmalarının gelişimi için çok önemlidir. Metalik nanoparçacıkların ışığı bağımlı saçma özellikleri farklı uygulamalar için yeni materyal özellikleri elde etmede kullanılabilir. Nanoparçacıkların bağımlı saçılımları yakın konumdaki parçacıkların yerleri ve dizilimlerinin anlaşılmasını sağlar. Bununla birlikte, bağımlı saçılım yapan nanoparçacıklar yüzey plasmon rezonansında uyarıldıklarında yarattıkları artan yakın elektromanyetik alanlarla yüksek ışık emilimine neden olurlar. Bu, nanoparçacıkların nano üretim amacıyla spektral yöntemlerle seçici ısıtma ve eritilmesi için kullanılabilir. Nümerik modellerin kullanılmasıyla nanoparçacıkların bağımlı saçılım özellikleri incelenebilir. Bu çalışmada metalik nanoparçacıkların bağımlı optik emilim verimleri yeni geliştirilen İntegral Poynting Vektör Yaklaşımı (IPVA) ile incelenecektir. Bu yöntem saçılım problemlerini nümerik olarak çözen DDSCAT ile birlikte kullanılmaktadır. Sonuçlar IPVA ve DDSCAT kullanarak başka yakın parçacıkların elektromanyetik alanlarından etkilenen nanoparçacıkların ışık emilim ve saçılımlarının incelenebildiğini göstermiştir. Bu yöntem çok zaman ve kaynak gerektiren deneysel çalışmalardan önce, bağımlı saçılımın arkasındaki fiziksel mekanizmanın anlaşılması için önerilmektedir.

Anahtar Kelimeler: Yüzey Plasmonları, altın nanoparçacıklar, bağımlı saçılım, DDSCAT, nanoüretim

To Mom and Dad

ACKNOWLEDGMENTS

I wish to thank my supervisor Assist. Prof. Dr. Tuba Okutucu who helped me select such an interesting topic and supported me in every stage of my thesis and to my co-supervisor Prof. Dr. M. Pınar Mengüç, who made a wonderful timing in returning Turkey, for providing me an excellent working atmosphere at Özyegin University during the last months of my thesis research.

At this point I want to thank Özyegin University that gave me the opportunity to work with my co-supervisor and letting me use their resources.

I would also like to thank my supervisors for encouraging me to spend time at conferences, and a two-month summer school of Nano-Initiative Munich at Ludwig Maximilian University. I want to thank my summer research mentor Calin Hrelescu from LMU Photonics and Optoelectronics Group, for sharing his knowledge on experimental studies with me.

Moreover, the financial support of TÜBİTAK is greatly acknowledged.

I would like to thank my wonderful family for believing in me and supporting my decisions and making my life easier and to my sister who has been and always will be the color of my life.

I want to express my gratitude to my dearest friends, who were ready to help me wherever they are, especially to Barış Akgün. I greatly appreciate his brilliant computer knowledge and patience, not to mention his support about the decisions I make, without him nothing would be so meaningful and no obstacle would be so easy to overcome.

TABLE OF CONTENTS

ABSTRACT	iv
ÖZ	vi
DEDICATION	viii
ACKNOWLEDGMENTS	ix
TABLE OF CONTENTS	x
LIST OF TABLES	xiii
LIST OF FIGURES	xiv
NOMENCLATURE	xvii
CHAPTERS	
1 INTRODUCTION	1
1.1 Scattering of Light By Small Particles	4
1.1.1 Absorption, Scattering and Extinction of Light	5
1.2 Optical Properties of Noble Metals	6
1.3 Surface Plasmon Resonance (SPR)	8
1.3.1 Modeling SPR	9
1.3.2 Factors Affecting SPR	10
1.3.2.1 Size Effects	11
1.3.2.2 Effects of Dielectric Constant	11
1.3.2.3 Shape Effects	12
1.3.2.4 Effects of Physical Environment	13
1.3.3 Dependent Scattering by Nanoparticles	16
1.4 Application Areas of SPR	17
1.4.1 Characterization of Nanoparticles	17

	1.4.2	Nanomanufacturing	18
	1.5	Objective and Overview of the Present Study	19
2		DISCUSSION OF LIGHT SCATTERING PROBLEMS	20
	2.0.1	Analytical Methods	20
	2.0.2	Numerical Methods	22
	2.1	Discrete Dipole Approximation: The Selected Method	25
	2.1.1	Sample DDA codes	28
	2.2	DDSCAT: The Selected DDA Software	30
	2.2.1	DDSCAT: What does it Calculate?	31
	2.2.2	Testing DDSCAT7.0	33
3		SOLUTION METHODOLOGY	36
	3.1	Problem Definition	36
	3.2	Methodology	38
	3.3	Governing Equations	40
	3.4	Integrated Poynting Vector Approach (IPVA): Does the approach work?	42
4		CASE STUDIES	44
	4.1	Case I: Capped Gold Nanocylinders: Comparison with an Experiment	44
	4.2	Case II: Two Identical Gold Spheres	47
	4.3	Case III: Two Gold Spheres with Different Sizes: An Insight to Surface Effects	48
	4.4	Case IV: A Gold Nanosphere and a Gold or Silicon AFM Tip	48
5		RESULTS AND DISCUSSION	52
	5.1	Case I: Capped Gold Nanocylinders: Comparison with an Experiment	52
	5.2	Case II: Two Identical Gold Spheres	56
	5.3	Case III: Two Gold Spheres with Different Sizes: An Insight to Surface Effects	56
	5.4	Case IV: A Gold Nanosphere and a Gold or Silicon AFM Tip	61
6		CONCLUSIONS	66
	6.1	Summary	66
	6.2	Limitations	67

7	RECOMMENDATIONS	68
7.1	Solutions to the Limitations	68
7.2	Possible Improvements for the Numerical Procedure	69
7.3	Future Prospects	70
7.4	Final Remarks	70
	BIBLIOGRAPHY	71
	APPENDICES	
A	DIELECTRIC CONSTANTS	78
A.1	Gold	78
A.2	Silicon	81
B	PARAMETER AND OUTPUT FILES OF DDSCAT7.0	84
B.1	Sample Parameter File (ddscat.par)	84
B.2	Sample Output Files	85
B.2.1	wxxxryy.avg Files	85
B.2.2	wxxxryyykzzz.sca Files	87
B.2.3	wxxxryyykzzz.poln Files	89
B.3	DDFIELD files	89
B.3.1	Sample DDFIELD.in file	89
B.3.2	Sample DDfield.E file	90
C	FORTRAN CODES	92
C.1	The Fortran Code for BHMIE Algorithm	92

LIST OF TABLES

TABLES

Table 2.1 DDA A Historical Outlook	24
Table A.1 Dielectric Function of gold (Au) [51]	78
Table A.2 Dielectric Function of silicon (Si) [52]	81

LIST OF FIGURES

FIGURES

Figure 1.1 Resolution (R)-throughput (T) trade-off of lithographic techniques [44].	3
Figure 1.2 Rose window of Notre Dame Cathedral [43].	4
Figure 1.3 The comparison of the dielectric function of gold molecules obtained by experiments and calculated with the Drude-Sommerfeld model including one interband transition [48].	7
Figure 1.4 Spectral dependence of the real and imaginary parts of the refractive index of bulk gold (according to references) [31, 25, 50, 58, 10, 51, 68, 37].	8
Figure 1.5 Schematic plasmon oscillation for a sphere, showing the displacement of the conduction electron charge cloud relative to the nuclei [35].	10
Figure 1.6 Different sized gold colloid solutions [1].	11
Figure 1.7 Absorption (C_{abs}) of gold (a) and silver (b) particles on glass versus wavelength [28].	12
Figure 1.8 Extinction efficiency spectra of a silver cube, different truncated cubes, and a spherical particle [47].	13
Figure 1.9 Absorption efficiency of a $D = 20$ nm gold sphere in ambients of various refractive indices obtained with DDSCAT adapted from [34]	14
Figure 1.10 Scattering matrix elements from a $D = 10$ nm gold particle above gold substrate [66].	15
Figure 1.11 Near field of a gold tip (5 nm tip radius) in water illuminated by two different monochromatic waves ($\lambda = 810$ nm) [48].	17
Figure 2.1 Dipole representation of a $D = 20$ nm sphere.	29
Figure 2.2 Scattering and absorption for a sphere with refractive index $m = 1.33 + 0.01i$	32

Figure 2.3 The effect of total dipole number N on the accuracy of DDSCAT7.0 (compared with Lorenz-Mie Theory)	35
Figure 3.1 Representations of the four problem cases investigated in this study: (a) capped gold nanocylinders: comparison with an experiment,(b) two identical gold spheres,(c) two gold spheres with different sizes: an insight to surface effects and (d) gold and silicon AFM tip and a gold nanosphere	37
Figure 3.2 The algorithm of Integrated Poynting Vector Approach	39
Figure 3.3 The model of the imaginary grid surface enclosing the investigated target geometry	41
Figure 3.4 Testing the accuracy of Integrated Poynting Vector Approach	43
Figure 4.1 Real image of gold nanorods (<i>private communication with Todd Hastings and M. Pinar Mengüç from University of Kentucky research program</i>).	45
Figure 4.2 Non-periodic model of gold cylinders used in DDSCAT.	46
Figure 4.3 The model of two identical $D = 20$ nm gold nanospheres in interaction when the incident light is polarized parallel and perpendicular to the axis connecting them.	47
Figure 4.4 Two spheres next to each other. The small sphere with 20 nm diameter and the bigger sphere 30 nm (cases b and e), 50 nm (cases c and f) and 60 nm (cases d and g) diameter	49
Figure 4.5 Dipole representation of a 20 nm diameter sphere and 100 nm diameter half sphere.	50
Figure 4.6 A representation of the AFM tip and nanosphere modeled in DDSCAT	51
Figure 5.1 Scattering, absorption and extinction efficiencies of capped gold nanocylinders illuminated with light with polarization parallel to the long axis.	53
Figure 5.2 Scattering, absorption and extinction efficiencies of capped gold nanocylinders illuminated with light with polarization perpendicular to the long axis.	53
Figure 5.3 Scattering, absorption and extinction efficiencies of capped gold nanocylinders illuminated with light with polarization 45 degrees to the long axis.	54

Figure 5.4	Experimental reflection percent of rounded gold rectangle array illuminated with light with parallel, perpendicular and 45 degrees (to the long axis) polarizations.	55
Figure 5.5	Dependent absorption spectra of two identical gold nanospheres with varying interparticle distance (g) when the incident light is polarized parallel and perpendicular to the axis connecting the spheres.	57
Figure 5.6	Absorption spectra of one of the spheres calculated with Integrated Poynting Vector Approach when the incident light is polarized parallel and perpendicular to the axis connecting the spheres as the gap (g) between the particle changes.	58
Figure 5.7	Absorption spectra of the small spheres calculated with Integrated Poynting Vector Approach when the incident light is polarized perpendicular to the axis connecting two spheres having different sizes.	60
Figure 5.8	Q_{abs} of a $D = 15$ nm Au nanosphere calculated with IPVA when the Au tip is 10 nm away.	62
Figure 5.9	Q_{abs} of a $D = 15$ nm Au nanosphere calculated with IPVA when the Au tip is 20 nm away.	62
Figure 5.10	Q_{abs} of a $D = 15$ nm Au nanosphere calculated with IPVA when the Au tip is 30 nm away.	63
Figure 5.11	Q_{abs} of a $D = 15$ nm Au nanosphere calculated with IPVA when the Si tip is 10 nm away.	63
Figure 5.12	Q_{abs} of a $D = 15$ nm Au nanosphere calculated with IPVA when the Si tip is 20 nm away.	64
Figure 5.13	Q_{abs} of a $D = 15$ nm Au nanosphere calculated with IPVA when the Si tip is 30 nm away.	64

NOMENCLATURE

a_{eff} effective radius [m]
 D diameter of the particle [m]
 g inter particle separation [m]
 d size of the dipole [m]
 c speed of light in vacuum [m/s]
electrical field vector [V/m]
magnetic induction vector [Wb=V.s]
magnetic field vector
Poynting vector
 M_{ij} scattering matrix elements
 q local time averaged absorption
 m refractive index
 n real part of the refractive index
 k imaginary part of the refractive index
 P_{abs} total absorption
 Q_{abs} absorption efficiency factor
 Q_{sca} scattering efficiency factor
 Q_{ext} extinction efficiency factor
wavevector
 x size parameter
 l_{mfp} length of mean free path
 l_r local thermodynamic equilibrium length

Greek Symbols:

λ wavelength of light in medium [m]
 α_{CM} Clasius-Mossotti dipole polarizability
 α_{LDR} lattice dispersion relation polarizability
 ϵ complex dielectric function
 ϵ_R real part of ϵ
 ϵ_I imaginary part of ϵ
 ϵ_0 permittivity of free space, 8.8542×10^{-12} [$C^2/N.m^2$]
 μ_0 permeability of free space, $4\pi \times 10^{-7}$ [$N.s^2/C^2$]

Abbreviations:

SPR Surface Plasmon Resonance
IPVA Integrated Poynting Vector Approach
CM Clasius Mossotti
LDR Lattice Dispersion Relation

CHAPTER 1

INTRODUCTION

In the past few years nanotechnological research showed that when matter is confined to very small sizes it loses some of its well known properties, instead these small particles create new types of unique responses to their environment. These responses started to be used for the solution of some problems that has not been solved because the material properties were limited with the bulk material properties. Today nanotechnology serves to this need, it solves the real life problems that has not been solved before. Besides it opens the doors of new applications that has not been dreamed before, where these properties can be used efficiently.

According to the National Nanotechnology Initiative (NNI) introduced back in 1998 by the National Science Foundation of the U.S.A., the definition of the nanotechnology includes three elements [57]:

- Exploiting the new phenomena and processes at the intermediate length scale between single atom or molecule and about 100 molecular diameters, in the range of about 1 to 100 nanometers.
- With the same principles and tools to establish a unifying platform for science and engineering at the nanoscale.
- Using the atomic and molecular interactions to develop efficient manufacturing methods

Thus, for applications of nanoscale sciences and nanotechnology to engineering practices we need to understand, control and manipulate matter at the level of individual atoms or molecules .It is widely accepted that nanotechnology revolution was first heralded by Feynman at his 1959 lecture [22]. Yet, the extensive practice of it started with the invention of scanning tunneling microscopy (STM) at IBM Zurich in 1981; an invention that radically changed the ways people interact with and perceive single atoms and molecules [24]. Today,

there are many microscopy techniques for the exploration of behavior of nanoscale particles and processes. An equally important topic, which is perceived as the heart of the nanostructure science and technology by some scientists [44], is the control and manipulation of those particles.

The nanomanufacturing methods are classified as **Top Down**, **Bottom Up** and **Combined Top Down and Bottom Up** approaches [9]. The lithography techniques such as *e-beam lithography*, *directed beams* and *replication of nanostructures like volume manufacturing and imprint lithography* are the examples of **Top Down** Approaches. Figure 1.1 shows the resolution vs. throughput trends for some of the lithographic techniques. This figure also shows that techniques invented for nanomanufacturing purposes require considerable amount of time and resource especially when the precision gets more important. To supply the demand in an economical manner it is required to move to the bottom-left corner of the figure by novel engineering approaches. This can be done by using hybrid bottom-up or combined approaches. **Bottom Up** methods such as *directed self assembly* and *self assembly* or hybrid methods like *directed self assembly of nanoelements with the help of nanotemplates* can be given as examples invented to minimize the problems explained above [44].

Therefore determining the unique properties of these particles that can be used for novel applications such as nanomachining, nanopatterning and diagnostics is required.

The optical properties of nanoparticles are among the most important special properties. Light scattering and absorption by these small particles can be used as a tool for diagnosis, as both processes strongly depend on size, geometry, composition and orientation of particles. Diagnosis of soot agglomerates in combustion systems [33], interstellar graphite grains in astrophysics [15], aerosols in environmental research and atmospheric science [60] can be performed by the information obtained from the scattered light. Optical imaging of biological cells (including cancer cell imaging with resonance scattering) [30] and diagnosis of the self-assembly of nanosized particles [66] are other characterization approaches. The popularity of the light scattering approach for the characterization is because it is possible to perform fast, low-cost, and rapid measurements [37].

The optical properties of the noble metals such as gold and silver particles have fascinated scientists since middle ages. Due to their exciting colors, the solutions including the colloids of gold were used for decoration purposes in coloring Chinese vases and other ornaments, and

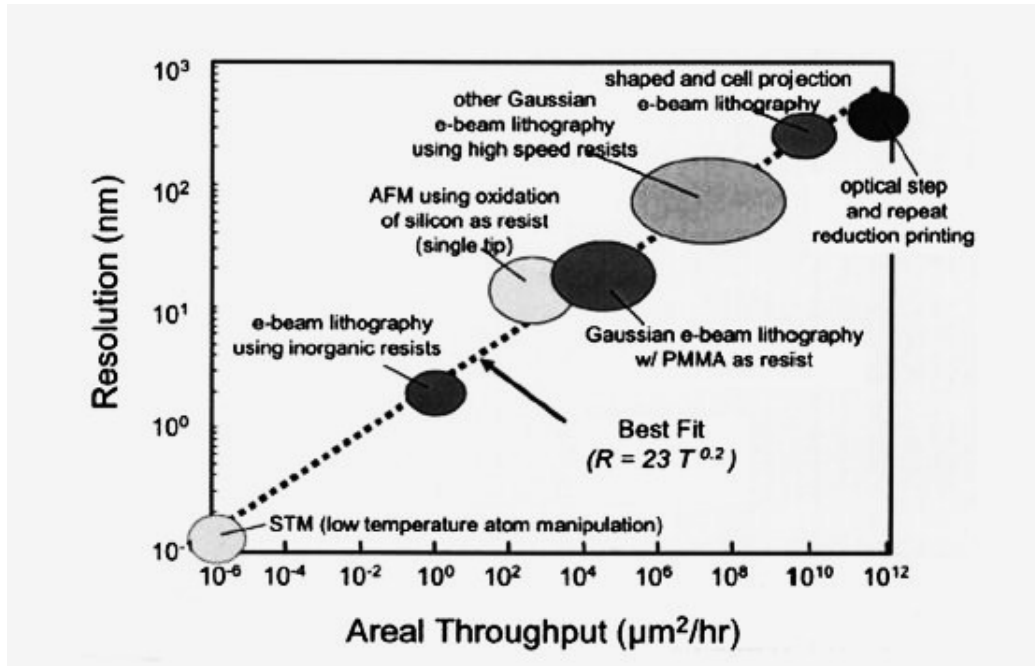


Figure 1.1: Resolution (R)-throughput (T) trade-off of lithographic techniques [44].

on stained glass windows as shown in Figure 1.2 [8].

Metallic nanoparticles are also important because some of their main physical properties might be completely different than the corresponding ones in either molecules or bulk solids [61]. The unique properties of metal particles are the real reasons for them becoming the ideal components of technological applications like waveguides, photonic circuits, chemical/biological sensors [59]. Today the science of optical phenomena related to the electrodynamic response of metals is so popular that it has a special name "Plasmonics" and "Nanoplasmonics" [7, 38].

In addition, selective absorption and emission of metallic nanoparticles make them favorable for manipulation purposes such as therapy of diagnosed cancer cells [30] and precise patterning of nanoparticles by spectrally selective heating [28].

Today noble metals such as silver and gold particles in various morphologies are used mostly for molecular plasmonic devices and biosensing [7]. The latest research on this area shows the usage of these particles in solar devices [11]. This marks the strong need for tracking the optical property behaviors of noble metal particles. In this thesis, the objective is to present a numerical procedure for the light scattering and absorption properties of noble metal particles

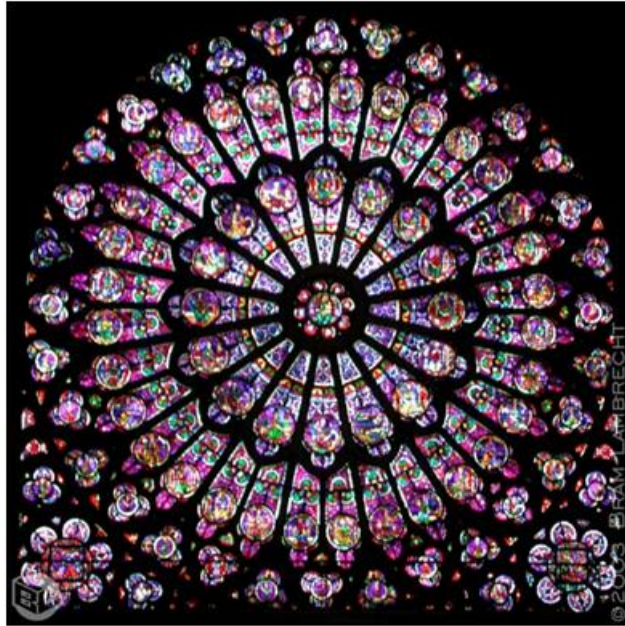


Figure 1.2: Rose window of Notre Dame Cathedral [43].

that will be used for further characterization or manufacturing purposes.

1.1 Scattering of Light By Small Particles

Scattering of light by small particles has been taken into consideration because they explain many physical phenomena as well as being very important for scientific and even engineering applications. As stated by Mischenko et al. [46] the scattered sunlight incident on the earth's atmosphere by gas molecules and suspended particles gives rise to blue skies, white clouds, and various optical displays such as rainbows, coronas, glories. The effects are not only visual because the earth's radiation budget is also affected by the absorption and scattering due to these particles. These particles are very small compared to the wavelength of incident light and can be treated with Rayleigh approximation, hence they are called Rayleigh scatterers [5]. Aforementioned applications involving the concept of electromagnetic light scattering from particles such as particle characterization are good examples for engineering applications. At this point, the interaction of light, an electromagnetic wave, with the small particles become very important. Thus, it is important to solve the electromagnetic scattering problem for small particles in order to determine the absorption, scattering and reflection profiles and use

them for useful characterization approaches. An example for this kind of characterization is the study of Aslan et al. for monitoring the self-assembly process of metallic particles on metallic surfaces in real time [3].

1.1.1 Absorption, Scattering and Extinction of Light

In this thesis, we consider **monochromatic light** which is an electromagnetic plane wave oscillating at a single frequency. When a parallel monochromatic beam of light propagating in vacuum without any change in its intensity or polarization state hits a small particle, it causes several effects. First one is the **absorption** which occurs when the particle converts some of the energy contained in the beam into other forms of energy such as heat. Second, it extracts some of the incident energy and scatters it in all directions at the frequency of the incident beam which is called **elastic scattering**. This, in general, gives rise to light with a polarization state different from that of the incident beam which is defined by the term **depolarization**.

Absorption and scattering of light causes a reduction of the energy of the incident beam. This reduction is called **extinction**. The extinction rates for different polarization components of the incident beam can be different. This phenomenon is called dichroism and may cause a change in the polarization state of the beam after it passes the particle. Moreover the particle might emit radiation in all directions if its absolute temperature is not equal to zero. This is called **thermal emission** [46].

The particles can be thought of as an aggregation of a large number of discrete relatively small electric charges. However, the number of elementary charges forming even in a micrometer-sized particle would be extremely large, and the solution of the scattering problem by computing and superposing all secondary waves is nearly impractical. It is for this reason that the problem is solved by using the concepts of macroscopic electromagnetic theory in which the large collection of charges is considered as a macroscopic body with a specific distribution of the refractive index. Then by using the Maxwell's equations for the macroscopic electromagnetic field the scattered field can be computed [46].

Hence, one of the most important parameters for the solution of the Maxwell's equations is to define a refractive index to macroscopically define the particles. It is known that, the proper-

ties of a material depend on the type of motion its electrons can execute. In a metal, electrons that are also called free conduction electrons are highly delocalized over large space [21]. The unique interaction of metals with electromagnetic radiation which is largely dictated by these free conduction electrons and has been used for many applications since the Middle Ages. The following section is devoted to the discussion of optical properties or more specifically dielectric function of noble metallic particles as these are the particles of interest in this study.

1.2 Optical Properties of Noble Metals

The optical properties of metallic particles are described by a complex dielectric function that changes with the frequency of light. According to Novotny and Hecht these properties are defined mainly by the facts that [48]:

- i. The conduction electrons can move freely within the bulk of material.
- ii. Inter-band excitations can take place if the energy of the photons exceeds the band gap energy of the respective metal.

The complex dielectric function (permittivity) has the form

$$\epsilon(\omega) = \epsilon_R(\omega) + \epsilon_I(\omega)$$

where $\epsilon_R(\omega)$ and $\epsilon_I(\omega)$ are the real and imaginary parts of the complex dielectric function (permittivity) $\epsilon(\omega)$.

Another optical property is called refractive index and is equal to the square root of complex dielectric function:

$$m = n + ik$$

where n is the real and k is the imaginary part of the refractive index m .

The dielectric function obtained by Drude-Sommerfeld model that considers only the effects of free electrons is accurate only in the infrared region ($\lambda > 700\text{nm}$) [48]. In the visible range

of the optical properties must be obtained by considering the response of bound electrons. This is due to higher energy photons that can promote electrons of lower lying bands in the conduction band, or in other words inter-band excitations [48].

The experimentally obtained optical constants of noble metals (silver, gold and copper) are given by Johnson and Christy [51]. Figure 1.3 shows the comparison of the constants obtained by the combination of free electron gas model and bound electrons when one inter band transition is taken into account with the experimental values.

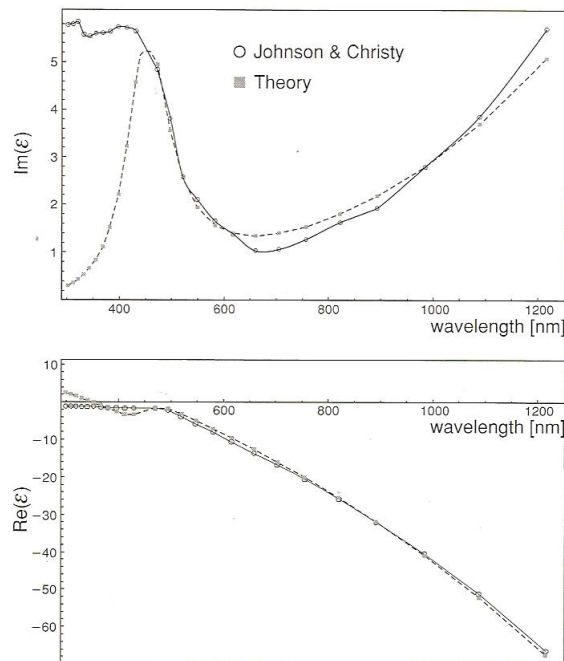


Figure 1.3: The comparison of the dielectric function of gold molecules obtained by experiments and calculated with the Drude-Sommerfeld model including one interband transition [48].

Figure shows how the model does not represent the data for wavelengths below $\sim 500\text{nm}$. Therefore, to eliminate any kind of error due to the usage of wrong dielectric constants for the particles investigated, experimentally obtained dielectric constants are used. Besides since the purpose of this thesis is to investigate the scattering trends of gold particles, thus from now on, only the dielectric constants of gold particles are considered.

Several groups presented wavelength dependent optical constants for Au polycrystalline films and for mono crystalline samples. Figure 1.4 shows the spectral dependence of the optical constants found by those groups. Khlebtsov et al. worked on these dielectric constants and

found that while some of them are good estimates for shorter wavelengths others are good estimates for longer wavelengths. Thus they came up with a spline fit shown in Figure 1.4 that best describes the spectral dependence of the dielectric constants [37].

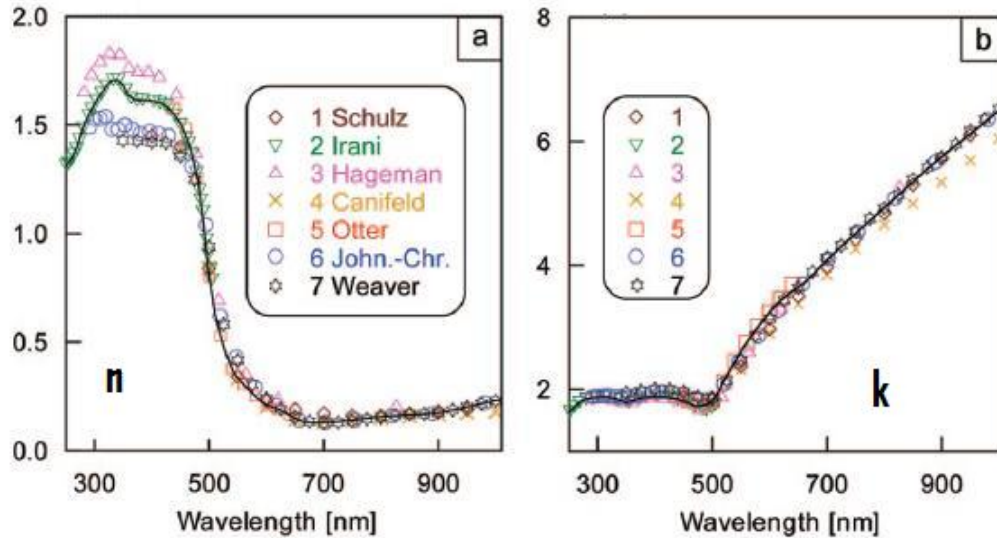


Figure 1.4: Spectral dependence of the real and imaginary parts of the refractive index of bulk gold (according to references) [31, 25, 50, 58, 10, 51, 68, 37].

Gold dielectric constants taken from the work of Johnson and Christy [51] that are presented in Appendix A. They are used in this thesis, since considering the spectral range that is investigated, the dielectric constants listed are not very different from the spline Sp1. Besides, the analysis about the size effects showed that the change of dielectric constants with varying size close to their original values and the numerical method used in this thesis consider the size effects automatically while calculating the polarizabilities of each dipole, hence size corrections are omitted as well.

Dielectric constants for silicon is also required. These are taken from Palik's book [52] and listed in Appendix A.

1.3 Surface Plasmon Resonance (SPR)

Perhaps the most interesting property of metal particles at nanometer scale is their surface plasmon resonances. Although by definition surface plasmons are surface-charge-density

oscillations, the same terminology is used for collective oscillations in the electron density at the surface of a metal [48].

Surface plasmon resonance (SPR) is the resonance at which a strong absorption is observed. In the case of noble metals, strong absorption in the visible - near ultraviolet (UV) occurs if the size of the particle is below the electron mean free path [21].

The mean free path (or the mean free time) is a measure of the average distance between successive collisions of energy carriers [69]. For metals electron mean free path l_{mfp} is important because electrons are the dominant energy carriers. This property depends on the medium and the energy of the energy carriers.

According to Wong and Menguc [69] in addition to mean free path there exist another critical length scale that lead to appropriate simplification of particle theories, called characteristic size of a volume over which local thermodynamic equilibrium is defined l_r . They claim that generally l_r is greater than l_{mfp} and it is calculated to exceed 20 nm for electrons assuming that the velocity of electrons is 10^6 m s^{-1} . Thus for metal particles at sizes close to this length thermodynamic equilibrium cannot be assumed and the strange behaviors such as SPR is observed.

At SPR the electrons begin to oscillate coherently under the restoring force of nuclei as shown in Figure 1.5 when there is a strong coupling between them and the electromagnetic radiation of light. Interestingly, this occurs at the visible to near UV region. Hence, depending on their shape or sizes nanoparticles are observed in brilliant colors.

1.3.1 Modeling SPR

Surface (or dipole) plasmon resonance (SPR) has a direct relation with the frequency dependent dielectric constant of the metal. It is possible to determine the SPR wavelength of the particles by several models. One such model involves a quasi-static approximation [35]. If the particle is much smaller than the wavelength of the incident light, the electric field can be considered constant and the problem is solved by the equations of electrostatics. The particles generally have different resonance modes such as dipole and quadrupole, where half of the electron cloud moves parallel to the applied field and half moves anti-parallel. When the size of a particle gets larger, higher multi poles become important [35]. For such cases it

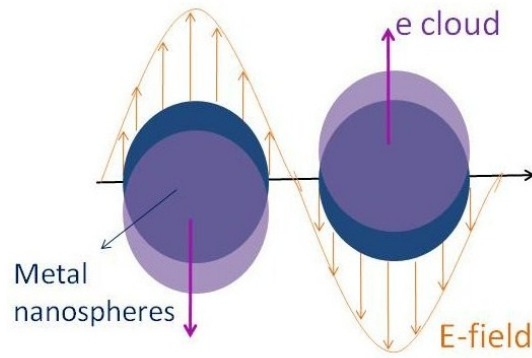


Figure 1.5: Schematic plasmon oscillation for a sphere, showing the displacement of the conduction electron charge cloud relative to the nuclei [35].

is essential to solve the electrostatic equations for higher multipoles. Moreover, for a metal like silver, the SPR frequency is also influenced by other electrons such as those in d-orbitals. This prevents the plasmon frequency from being easily determined using electronic structure calculations [35].

Behavior of the metal particles, hence, the plasmon resonance is strongly influenced by several factors such as particle size and the particle composition. Other factors influencing the SPR of particles will be discussed in the next section.

1.3.2 Factors Affecting SPR

Kelly et al. defines the essential functions that determines the SPR frequency [35]:

- the density of electrons,
- the effective electron mass,
- the shape and the size of the charge distribution.

These properties can be classified as size, shape and dielectric function effects and they are defined by the functions listed above. These effects as well as the effects of the physical environment on the absorption spectra of metallic particles are explained in the following sections.

1.3.2.1 Size Effects

The size of the particles also influence SPR. It is known that bulk gold has a popular yellow color; but as the size gets smaller the color changes and shifts to the red. This is due to the surface plasmon resonance of the gold particles. Cortie's explanation is that when the gold particles are small enough their color is ruby red due to their strong absorption of the green light at about 520 nm, corresponding to the plasmon resonance frequency. Moreover, their color can be systematically varied from pink through violet to blue as shown in Figure 1.6 if such tiny particles are allowed to coalesce in a controlled fashion [13].

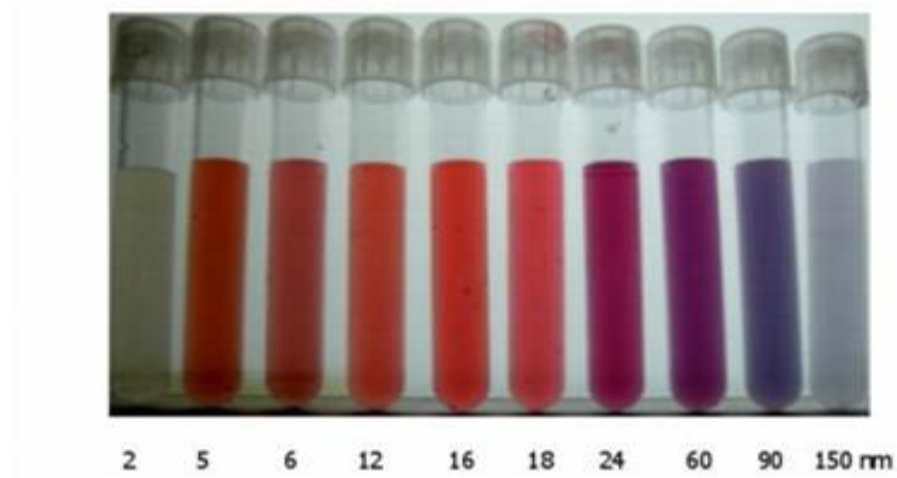


Figure 1.6: Different sized gold colloid solutions [1].

Link et al. [43] explained this color variation by the effect of higher-order modes becoming dominant with increasing particle size causing the absorption band to redshift with an increased bandwidth .

1.3.2.2 Effects of Dielectric Constant

The plasmon resonance is strongest and shifted into the visible part of electromagnetic spectrum for noble metals such as: copper, silver and gold [66]. However, for each of these metals the frequency dependent dielectric constant is different. The Figure 1.7 shows the absorption of gold and silver particles on glass when particle-substrate separation increases from 1 to 10

nm. Gold spheres show maximum absorption and scattering at wavelengths near 500 nm in air or vacuum. On the other hand, silver nanostructures display similar behavior at resonances occurring at about 350 nm [28].

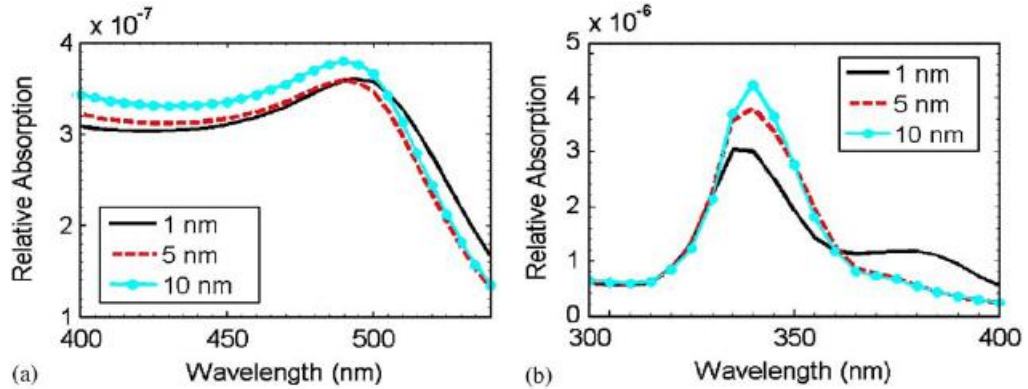


Figure 1.7: Absorption (C_{abs}) of gold (a) and silver (b) particles on glass versus wavelength [28].

This difference is because of the different electronic charge distributions and density for different types of metals.

1.3.2.3 Shape Effects

The effects of shape on SPR have been investigated by many researchers. According to Noguez, the shape effects differ for particles with different sizes as follows[47].

- a. Small Particles ($d < 40$ nm): The displacement of the charges are homogeneous if the particles are smaller than about 40 nm in diameter this results in a dipolar charge distribution on the surface. Therefore, the particle has only one resonance that is determined by the shape and the electric density of the particle. Ellipsoids and cubes for example have more than one dipolar mode or may have extra higher resonance modes due to their anti-symmetry and directional polarizabilities (Figure 1.8) [47].
- b. Large Particles ($d > 40$ nm): If the particle diameter exceeds 40 nm, the higher modes become more important. Because of the accelerated electrons an additional polarization

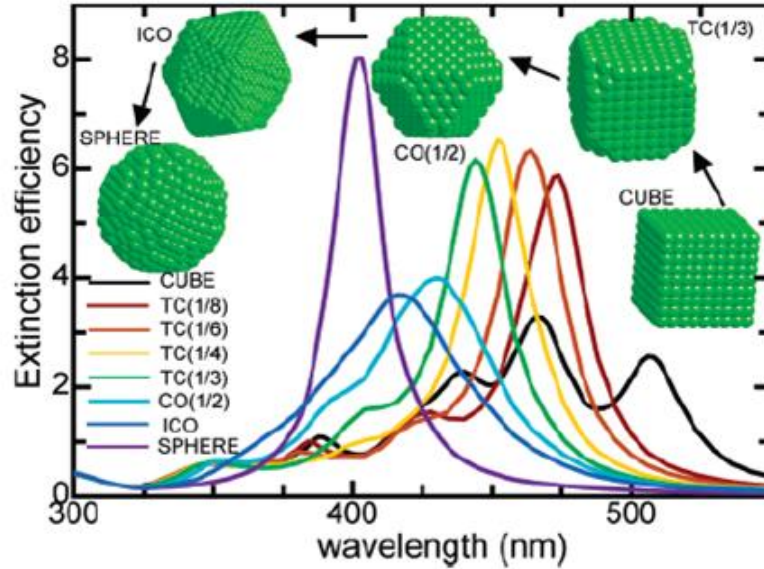


Figure 1.8: Extinction efficiency spectra of a silver cube, different truncated cubes, and a spherical particle [47].

field that depends on the ratio of the size of the particle and the wavelength of the incident light is produced. This additional radiation causes the loss of energy of the electrons with its damping effect and widens the SPRs. This secondary field, which is also known as the near field, reacts against the quasi-static polarization field shifting the position of the modes to longer wavelengths. Hence, the radiation damping reduces the intensity and makes broader and asymmetric red-shifted SPR peaks [47].

1.3.2.4 Effects of Physical Environment

Similar to dielectric constant of the particles dielectric constants of the environment and what is present in the environment influences the SPR from nanoparticles. According to Noguez, SPR in a medium with refractive index $n > 1$ is red-shifted with respect to those in vacuum [47].

This is presented with the results obtained by a numerical method DDSCAT, in Figure 1.9. Details about this program will be given later in this study.

Moreover, the surfaces which play significant roles in technological applications like surface

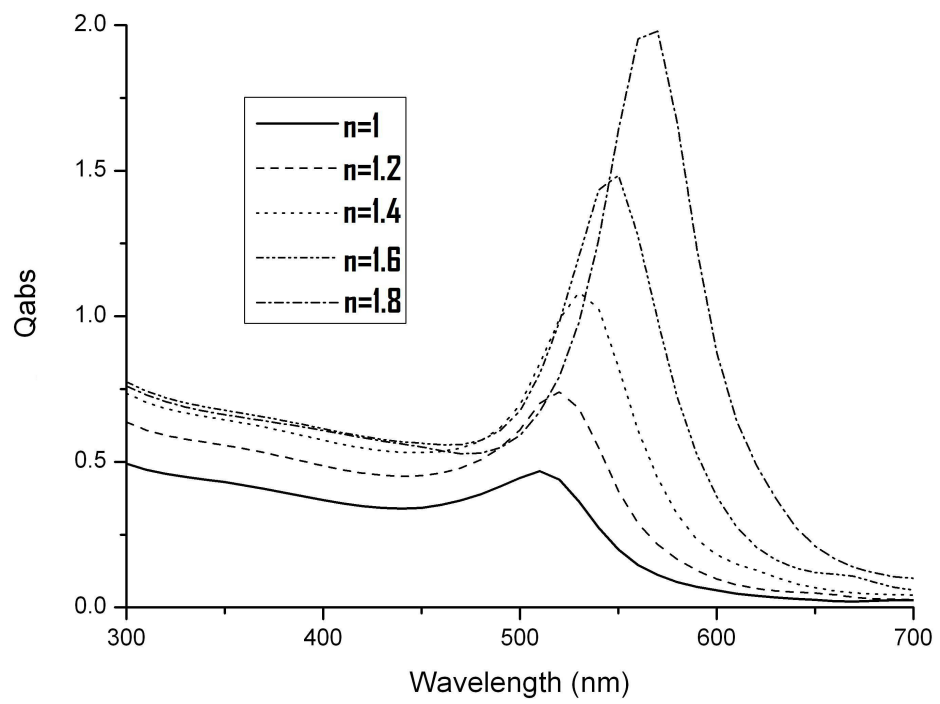


Figure 1.9: Absorption efficiency of a $D = 20$ nm gold sphere in ambients of various refractive indices obtained with DDSCAT adapted from [34]

enhanced Raman scattering (SERS), catalytic processes, plasmonic devices and others has great influence on SPR of nanoparticles. This is illustrated in Figure 1.10. Just like surface effects other particles present in the medium and close enough to each other influences the optical absorption spectra of each other. The distance between the particles and surface, particle material and morphology and the direction of electromagnetic field all play great roles in this interaction [47, 28, 66]. This kind of scattering can be named *dependent scattering* and will be explained in the next section.

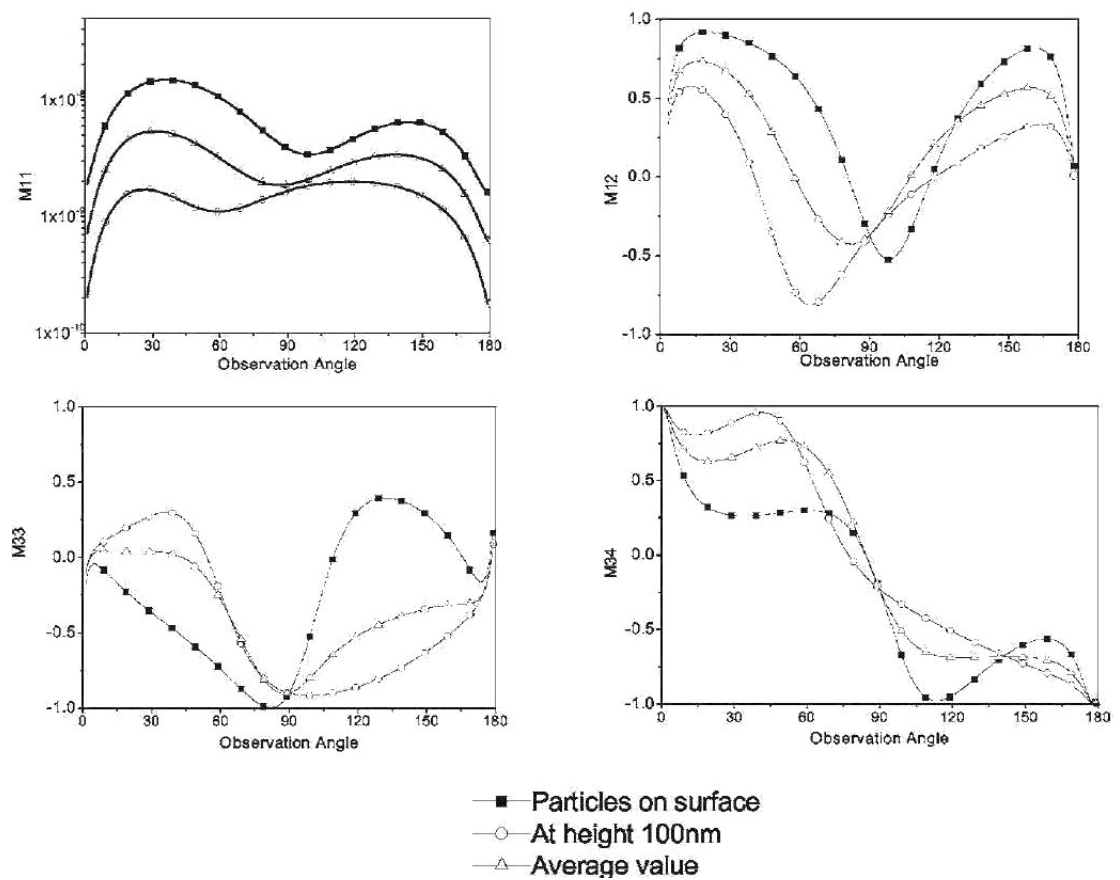


Figure 1.10: Scattering matrix elements from a $D = 10$ nm gold particle above gold substrate [66].

1.3.3 Dependent Scattering by Nanoparticles

Physical environment affects absorption spectra hence SPR of metal particles. The scattering of particles experiencing the effects of physical environment can also be called dependent scattering.

Spatially localized light can be achieved near the surface of the particles and it is called near field [49]. Small metal structures create near field when irradiated. This near field is localized to the surface of the material and depending on the material properties, the near field intensity can be enhanced over the intensity of the irradiating light [48].

This light is responsible for the dependent scattering of nanoparticles. Because, as the distance between the particles decrease electromagnetic near fields become comparable to the exciting field and the particles are electromagnetically coupled [7]. The simplest cases where the near field effects can be seen are the two particles located close to each other and an array of closely packed particles.

To explain the physical mechanism behind the near field enhancements Novotny and Hecht [48] gives the example of field enhancement at the tip of an AFM probe. Figure 1.11 shows the near field enhancement of a gold tip. In the book it is explained as:

Consider a metal tip made of a gas of free electrons. The external driving field, polarized along the tip axis, drives the free electrons up and down along the axis with the same frequency as the exciting field. Since the surface area near the tips are small the oscillation of the gas of free electrons results in the accumulation at the tip. These charges generate a secondary field that is seen as the enhanced field.

Figure 1.11 illustrates this concept graphically with the contours of E^2 . In the figure direction of polarization of the incident wave are indicated by the \mathbf{k} and \mathbf{E} . While the intensity near the tip is highly enhanced for the incident light is polarized parallel to the tip axis no significant enhancement is observed for the incident field with perpendicular polarization [48].

This effect of dependent scattering must be carefully analyzed because it may lead to significant enhancements of optical absorption of nanoparticles and thus be used for different engineering applications. For example, Hawes et al. used this concept to selectively melt and evaporate the nanosized particles [27].

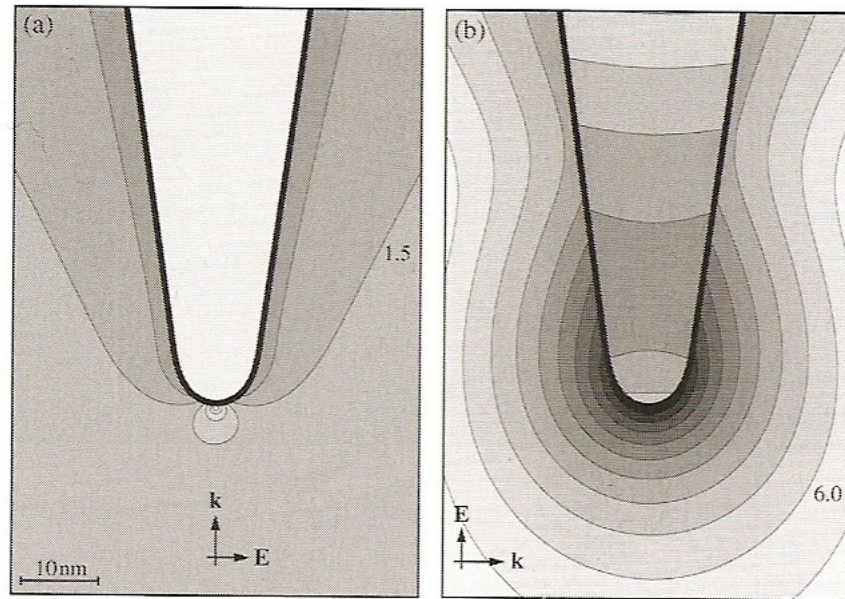


Figure 1.11: Near field of a gold tip (5 nm tip radius) in water illuminated by two different monochromatic waves ($\lambda = 810$ nm) [48].

1.4 Application Areas of SPR

The strong coupling between light and surface plasmons in nanostructures leads to novel phenomena such as optical force enhancement in nanoaggregates, transport and storage of energy, as well as its localization and guiding, surface-enhanced sensing and spectroscopy, controlling the anisotropic growth of nanoparticles, and measuring intra molecular and conformational distances in molecules [47]. Applications which utilize these unique properties of the noble metal particles can be listed under two broadly defined implementation areas: characterization and nanomanufacturing. These concepts are briefly discussed in the next sections.

1.4.1 Characterization of Nanoparticles

According to Noguez, “*a clear and general interpretation of SPR in metal nanoparticles is not available today*” [47]. Although there is still lack of information about the direct relation between the SPR and the morphology, the influence of the geometry and size on the optical properties of metal nanoparticles can be used for characterization purposes. This is verified by the works on the optical response of spherical, spheroidal, cubic and other geometrical shapes

like rods and triangular prisms [47]. Figure 1.8 illustrates SPR wavelength, or in other words the wavelength at which the maximum extinction occur, for different particle geometries. In theory, by examining these spectral optical responses one can non-destructively define the particle morphologies. In practice, however, this is more difficult since there would be a distribution of shapes in a solution.

Although characterization of particles can be achieved using advanced microscopy techniques such as SEM (scanning electron microscopy), TEM (transmission electron microscopy), or AFM (atomic force microscopy), these methods have several disadvantages as being limited to 2-D observations, having the risk of altering particle shapes and agglomeration during handling, and the potential of orientational biasing. Spectral methods can only be good complementary tools for characterization since they can sample relatively high number of particles non-destructively at a time [47]. As an example, Charnigo et al. suggested a new statistical methodology based on derivatives of scattering profiles for nanoparticle characterization and does not require the visual inspection of profile estimates by a human operator [12].

1.4.2 Nanomanufacturing

In addition to its use in characterization, SPR can also be used for nanomanufacturing purposes. Basically it is a method using light in positioning atoms but it is highly important to differentiate it from other techniques using light to position atoms such as lithography.

Most of the conventional lithography techniques involve a light exposure of a light sensitive resist to transfer pattern from a mask to a substrate. This method can be used to produce mass of products at a time because a mask can be used to expose millions of features at the same time. It is noted that the minimum size of the features that can be obtained with this technique is of the order of half the wavelength of the light used for the lithography. There are other exposure techniques such as electron beam lithography and x-ray lithography that are capable of producing smaller structures but they have some disadvantages like being slow and destroying the mask and substrate because of being highly energetic [63]. Hawes et al. proposed the method *Spectrally Selective Heating of Nanosized Particles* for the solution of the problems arising from the usage of lithographic techniques and can again be treated as a novel lithographic technique that uses a slightly different light exposure technique but no mask this time [26].

The particles experiencing SPR strongly absorb the incident light. This absorbed quantity of energy is sometimes enough to fuse particles or the matrix surrounding it. Next step is to heat particles locally in a selective manner, as recommended by Hawes et al. [28]. Since the SPR wavelength depends on particle shape and size, the light sent at a correct frequency is capable of fusing the particles as described above. Besides, with the combined effect of strong absorption at SPR and the enhancement of electromagnetic field due to an AFM tip in proximity to the particle, faster and better results can be obtained [26].

1.5 Objective and Overview of the Present Study

The objective of this study is to investigate the dependent absorption and scattering efficiencies and surface plasmon resonance of noble metals, specifically gold, having different shapes, sizes and compositions with the help of a numerical light scattering solution program (DDSCAT) [18]. The physical environment effects such as the insertion of other particles and an AFM tip to the medium, are considered in this work.

The above mentioned analysis is performed for better understanding of the behavior of the closely positioned particles or the particles near an AFM tip when subjected to light at different frequencies and polarizations. Besides, it will make the efficient and proper design and use of nanomachining and nanopatterning efforts. Simulations will be performed to understand if numerical methods can be used to understand the physical processes prior to experiments. This is important because such experiments require too many resources.

CHAPTER 2

DISCUSSION OF LIGHT SCATTERING PROBLEMS

Although the light scattering properties for noble metal particles were known since middle ages, it was Faraday who first explained it theoretically in 1700s. Later, in 1908, Gustav Mie managed to solve the Maxwell's equations analytically in order to analyze the scattering from particles with spherical shape [43]. This study was widely recognized, although 1891 Lorenz presented a similar solution methodology. Since that time there have been strong interest in the solution of light scattering problems either analytically or numerically. The next two sections are devoted to these methods.

2.0.1 Analytical Methods

As mentioned before the electromagnetic scattering problems are governed by a set of equations called Maxwell equations when the target is described in terms of various dielectric constants. Maxwell equations describe the wave nature of the radiation in terms of magnetic and electric fields [39]. The following four equations that are also known as Maxwell equations describe radiative transfer at the nanoscale [5].

$$\nabla \times E = -\frac{\partial B}{\partial t} \quad (2.1)$$

$$\nabla \times H = J + \frac{\partial D}{\partial t} \quad (2.2)$$

$$\nabla \cdot D = \rho \quad (2.3)$$

$$\nabla \cdot B = 0 \quad (2.4)$$

The variables in Maxwell equations are linked to each other by the following equations:

$$D = \epsilon E \quad (2.5)$$

$$B = \mu H \quad (2.6)$$

$$J = \sigma E \quad (2.7)$$

and by continuity equation

$$\nabla \cdot J = -\frac{\partial \rho}{\partial t} \quad (2.8)$$

However, the analytical solution becomes technically demanding when particles with complex geometries are investigated [34]. This is why the best known analytical solution method, the **Lorenz-Mie** theory is restricted to the spherical particles with arbitrary sizes immersed in a homogeneous medium and subjected to a plane monochromatic wave.

For nanoparticles whose sizes are much smaller than the wavelength ($d \ll \lambda$) of the interacting light, only the dipole oscillation contributes significantly to the extinction cross section. The Lorenz-Mie theory then reduces to the following expression which is also called the dipole approximation [43].

$$C_{abs} = \frac{8\pi^2 a^3 \sqrt{\epsilon_1}}{\lambda} \text{Im} \frac{\epsilon - \epsilon_m}{\epsilon + 2\epsilon_m} \quad (2.9)$$

The dipole approximation results in a resonance condition that is independent of size. Yet, as mentioned earlier SPR changes with size. Therefore, for small particles (<20nm) the bulk dielectric constant can not be used for defining the particle [2]. The reason for this deviation is explained earlier as the smaller mean free path for conduction electrons.

The Lorenz-Mie theory fails to explain the scattering mechanism when particles aggregate and tend to deviate from their spherical shape, and to explain why the bulk dielectric constant does not apply to nanoparticles ranging from 5 to 20 nm.

Several groups have proposed useful extensions to Lorenz-Mie theory using size dependent dielectric constants to account for quantum size effects and surface scattering. Of course, interest also moved to more complicated geometries like ellipsoids and non-spherical particles. For example, **Rayleigh-Gans-Debye** theory is an approximate method that models the scattering body as a collection of Rayleigh scatterers (scatterers that are small when compared to the wavelength of incident light) that do not interact with each other [40].

Another theoretical solution method, the **T-matrix** method, proposed by P. C. Waterman in 1965 [67] is a general formulation where the incident and scattered electric fields are expanded in series of vector spherical wave functions and the relation between the columns of the respective expansion coefficients is established by means of a transition matrix (or T matrix). This method can be used to compute the scattering from particles with arbitrary shapes, but it is the most efficient with axially symmetric particles. The applicable regime of this methods is limited since the matrices used can easily become ill-conditioned when the surface corrugation is deep or when the corrugation depth divided by the period is large [64].

Thus, analytical solutions for non-spherical cases exist only for particles having specific geometries. For this reason scattering problems of particles having a variety of shapes must be solved by numerical methods. Although some of these solutions are technically demanding, the developing computers and programs render the numerical solutions favorable.

In this study we restrict ourselves to the elastic or coherent case, where the frequency of the absorbed and scattered light is the same as the frequency of the incident light. This is because solving the scattering problem directly by computing and superposing all secondary waves is not possible even with the aid of modern computers.

2.0.2 Numerical Methods

Although theoretical solutions are possible for particles of certain shapes, optical behavior of nanoparticles with other arbitrary shapes can only be found using approximate or numerical techniques. The numerical techniques must be efficient to deal with complex systems and produce reliable results [47]. The mostly used numerical methods to solve the problem of light scattering by non-spherical particles maybe listed as:

1. Ray-tracing
2. Finite Difference Time Domain (FDTD)
3. Finite Element Method (FEM)
4. Fast Multipole Method (FMM) and Multi Level Fast Multipole Algorithm(MLFMA)
5. Discrete Dipole Approximation (DDA) Method

Ray-tracing is used for particles much larger than the wavelength. The particle is discretized and on each facet (of the discretized particle) one applies the Fresnel equation to the incident rays [45].

The **FDTD** consists in writing the Maxwell equations in discrete form and solving them in the time domain.

Similarly **Finite Element Method** is a standard tool for solving differential equations in many disciplines. The disadvantage of the Finite Element Method compared to the FDTD is the necessity for the solution of the whole system of equations at each time step [6].

If the boundary value problems can be formulated as integral equations they can be solved by one of the methods that will be described below. These methods are all used for the solution of integral equations derived by the use of Green's function. The Method of Moments is another used by electromagnetic community instead of integral formulation [64]. In integral equations number of unknowns is small yet the matrix is very dense making computational efforts quite involved.

The **Fast Multipole Method** (FMM) and **Multi Level Fast Multipole Algorithm** (MLFA) are the two methods that solve dense matrix problems coming from integral equations and they are superior to differential equation solvers for large problems.

The **Discrete Dipole Approximation** (DDA) is a flexible approach that discretize and solve the integral equations numerically [64]. It consists of dividing a particle into dipolar subunits arranged in a cubical lattice. This method has been used to compute optical properties of irregularly shaped particles.

Table 2.1: DDA A Historical Outlook

Year	Reference	Scattering Medium	Property Computed	Character of the Medium	Major Findings
1988	Draine [15]	spheres	$Q_{ext}, Q_{abs}, Q_{sca}$	graphite grains	DDA checked with exact results from Mie. Validity criteria are: N must be large enough and dipole array provide a satisfactory approximation: $ka_{eq} < ka_{crit}$.
1993	Flatau [23]	2 spheres in contact	$Q_{ext}, Q_{abs}, Q_{sca}$	ice	DDA with CGFFT makes accurate calculations of scattering and absorption of dielectric particles.
1993	Taubenblatt & Tran [62]	Surfaces	S_{11}	Si and SiO_2	Coupled Dipole method can be used to take into account the presence of a surface when the reflected dipole waves are included in the matrix.
1994	Draine & Flatau [16]	spheres	Q_{abs}, S_{11}, S_{12}	ice	Presented DDSCAT.
1995	Yang [70]	isolated spheroid, tetrahedron, spheroids	Extinction Raman intensities	silver	Solved interaction of electromagnetic fields with small metal particles.
1996	Ivezic & Menguc [32]	2 separated spheres, agglomerates of up to 12 spheres	Absorption, Scattering	soot	Mutual interaction of 2 spheres does not affect absorption when the ratio of their distance to the radius is greater than 3. For agglomerates dependent effects cannot be neglected when $0.2 \leq x_0 \leq 2$ where dependent effects cannot be neglected.
2003	Kelly [35]	truncated tetrahedron, prisms	$Q_{ext}, Q_{abs}, Q_{sca}$	silver	Many optical properties of silver nanoparticle having complex shapes in complex environments analyzed.
2003	Sosa [61]	nanosphere, cube, spheroid, cylinder, tetrahedra	$Q_{ext}, Q_{abs}, Q_{sca}$	silver and gold	Extinction efficiency is not enough to elucidate the size and shape of a nanoparticle, in depth study of Q_{abs} and Q_{sca} is required.

Continued on Next Page...

Year	Reference	Scattering Medium	Property Computed	Character of the Medium	Major Findings
2006	Prescott & Mulvaney [55]	capped cylinders $r = 5 - 40nm$ aspect $ratio = 1 - 8$	Extinction Spectra	gold	Rod width, end-cap geometry and size distribution affects the position of peak absorbance. Spectrometric characterization of nanorods is possible.
2007	Ayranci et al. [4]	-	Performance of DDSCAT analyzed	-	Errors strongly depend on the complex refractive index.
2007	Yurkin [72]	spheres	integral and angle resolved spectra	$x = 160, 40$ $m = 1.05 - 2$	Errors generally increase with m. Show no systematic dependence on x. Computational times increase with m and x.
2007	Pentilla [53]	-	Different DDA codes compared	-	DDSCAT and ZDD produce accurate results, ADDA is fast and SIRRI is very flexible to use allowing e.g. user-specified list of orientation angles.
2008	Draine & Flatau [17]	infinite cylinder infinite slab etc.	$S_{11}, S_{12}...$	ice	DDA can be extended to targets that are singly- or doubly-periodic

Once a numerical method is chosen, it is important to select a realistic dielectric function that better resembles the material properties of the system, in this case, particles of nanometric sizes [47].

2.1 Discrete Dipole Approximation: The Selected Method

In this thesis DDA is chosen as a solution tool. The major advantage of this method is its success in handling virtually every particle shape. Besides, light scattering solution programs based on DDA method such as ADDA and DDSCAT that will be covered in the next section are publicly available. For this reason these programs and DDA are tested by many scientist coming from a variety of backgrounds. Therefore, DDA can be used as a reliable tool for our research.

DDA (Discrete Dipole Approximation or Coupled Dipole Moment) was introduced by Purcell and Pennypacker for calculating optical properties of interstellar grains. Since its introduction in 1973, has remained almost unchanged.

For spherical particles the Lorenz-Mie theory of scattering readily yields exact solutions. Yet a reliable method for calculating scattering and extinction cross-section of grains of arbitrary shape and arbitrary complex refractive index is still needed [56] and DDA serves to this need.

Purcell and Pennypacker define their method as follows [56]:

“Consider a plane electromagnetic wave incident on a rectangular parallelepiped made of material of dielectric constant ϵ . Think this as a brick as an assemble of polarizable atoms in a vacuum. Yet number of atoms even in a submicroscopic grain, would be very large. So we replace the brick by a much coarser array of polarizable elements.”

Each dipole is represented by its complex polarizability α which is given by Clasius - Mossotti relation given by equation [19]:

$$\alpha_{CM} = \frac{3}{N} \frac{\epsilon(r_i) - 1}{\epsilon(r_i) + 2} \quad (2.10)$$

where N is the number of polarizable elements per unit volume.

Each of the N atoms is exposed to the field of the incident wave and to the field of every atom. Thus the starting point is the equation [45]

$$E_i(r) = E_o(r) + \sum_{j \neq i=1}^N E_{ij}(r), \quad r \in V_i, i = 1 \dots N. \quad (2.11)$$

There are N dipoles. The $E_i(r)$ can be thought as equal over the particles' volume. Thus the equation can be written as:

$$E_i = E_{0,i} + \sum_{j \neq i=1}^N E_{ij}, \quad i = 1 \dots N. \quad (2.12)$$

E_{ij} can be represented as a function of the local electric field on the particle j .

$$E_{ij} = C_{ij} \cdot E_j \quad (2.13)$$

where

$$C_{ij} = \begin{cases} [A_{ij}I + B_{ij}(n_{ji} \otimes n_{ji})] \cdot \alpha_j & i \neq j \\ 0 & i = j \end{cases} \quad (2.14)$$

In this equation n_{ji} is the unit vector pointing from particle j to particle i, \otimes is the tensor product and α_j is the polarizability tensor of particle j.

A_{ij} and B_{ij} are defined as:

$$A_{ij} = \frac{\exp(ikr_{ij})}{r_{ij}} \left(k^2 - \frac{1}{r_{ij}^2} + \frac{ik}{r_{ij}} \right) \quad (2.15)$$

$$B_{ij} = \frac{\exp(ikr_{ij})}{r_{ij}} \left(\frac{3}{r_{ij}^2} - k^2 - \frac{3ik}{r_{ij}} \right) \quad (2.16)$$

The matrix representation of $E_{0,i}$ and E_j and C_{ij} are as below:

$$\mathbf{E}_0 = \begin{pmatrix} E_{0,1} \\ \cdot \\ \cdot \\ E_{0,N} \end{pmatrix} \quad \mathbf{E} = \begin{pmatrix} E_1 \\ \cdot \\ \cdot \\ E_N \end{pmatrix} \quad (2.17)$$

$$\mathbf{C} = \begin{pmatrix} O & C_{12} & \dots & C_{1N} \\ C_{21} & O & \cdot & \cdot \\ \cdot & \cdot & \cdot & \cdot \\ \cdot & \cdot & \dots & \cdot \\ C_{N1} & \dots & \cdot & O \end{pmatrix} \quad (2.18)$$

Equation 2.11 can be shown in matrix representation as

$$\mathbf{E} = \mathbf{E}_0 + \mathbf{C} \cdot \mathbf{E} \quad (2.19)$$

Equation 2.19 can be solved to obtain local electric fields at each dipole.

$$\mathbf{E} = (\mathbf{I} - \mathbf{C})^{-1} \mathbf{E}_0 \quad (2.20)$$

Since electric field is calculated for each particle total scattered field can easily be calculated using the relation

$$E_s = \frac{1}{4\pi} \sum_{i=1}^N [A_i I + B_i (n \otimes n)] \cdot \alpha_i E_i \quad (2.21)$$

To test their method, Purcell and Pennypacker applied it to spheres. The solutions obtained by the method is very close to the Lorenz-Mie solution.

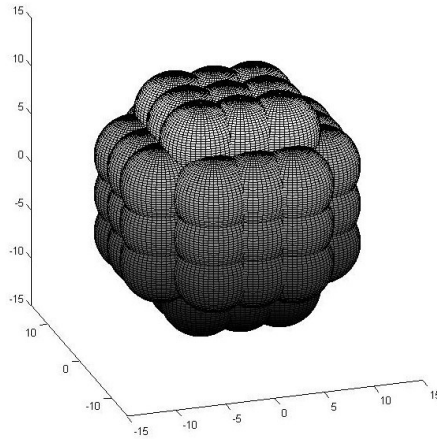
Draine and Flatau [16] stated that there are two obvious criteria for the validity of the DDA:

- i. $|m|kd \leq 1$ (so that the lattice spacing d is small compared with the wavelength of a plane wave in the target material)
where d is the inter dipole spacing and $k = \omega/c$
- ii. d must be small enough (N must be large enough) to describe the target shape satisfactorily. This is illustrated in figure 2.1. As the size of the dipoles decrease the number of dipoles representing the target increases, hence the dipole representation approaches the real target geometry.

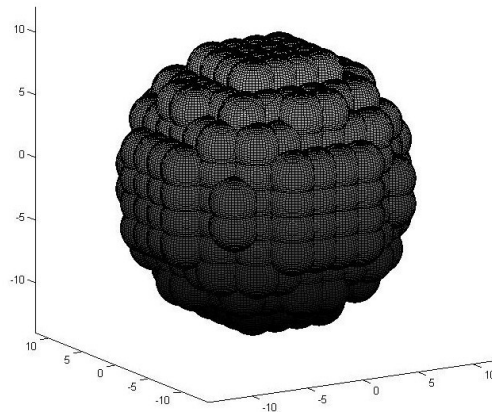
2.1.1 Sample DDA codes

Four DDA codes written by different groups and researchers are listed below. These codes are compared by A. Pentilla et al. in detail [53]. Here, a brief explanation for each of them as well as their advantages and disadvantages are given.

1. **SIRRI**: Written in Fortran, this code is a fast code for single orientation and can calculate the scattering from anisotropic materials. Yet it is not publicly available and it is one of the least accurate methods.
2. **DDSCAT**: It is written in Fortran and is publicly available. It gives the best overall accuracy when compared to other codes.
3. **ZDD**: The code is written by C++. It uses some of the features of DDSCAT but it is the slowest on the supercomputer environment with single orientation and not publicly available.



(a) When 81 dipoles are used



(b) When 552 dipoles are used

Figure 2.1: Dipole representation of a $D = 20$ nm sphere.

4. **ADDA:** Amsterdam DDA (ADDA) is another code that simulates elastic light scattering from finite 3D objects using DDA. It is publicly available and most of the code is written in ANSI C. The advantage of ADDA is its capability of running on cluster of computers that allows unlimited number of dipoles in scattering calculations. Yet only a few predefined shapes are currently available.

Because of the above listed advantages and accuracy of DDSCAT, the computations in this thesis are performed by this code. The details related with this code are explained in the next section.

2.2 DDSCAT: The Selected DDA Software

DDSCAT is a Fortran software package to calculate scattering and absorption of electromagnetic waves by targets with arbitrary geometries using the *DDA*. DDSCAT is developed by Draine and coworkers [16].

It is intended to be a versatile tool, suitable for a wide variety of light scattering problems of interstellar dust to atmospheric aerosols [15].

Draine and Flatau mainly discussed two computational methods for the solution of Equation 2.20 in their paper:

1. Complex- Conjugate Gradient Method (CCG);
2. Fast Fourier Transform (FFT).

Moreover they defined a new polarizability α_{LDR} ($LDR \equiv$ *latticedispersionrelation*) other than the α_{CM} ($CM \equiv$ *Clasius – Mossotti*) by stating that the assumption of the uniform electric field over cubical regions is not totally valid.

As stated before there are several restrictions on the dipole size and the size of the target for the accuracy of DDA. These restrictions hold for the code DDSCAT since it uses DDA codes in principle. Draine and Flatau presented the DDSCAT results obtained by using different number of point dipoles, new computational methods (CCG, FFT) and the new polarizability factor α_{LDR} and their comparison with the exact Lorenz-Mie solution. Relative error is equal to the absolute value of the difference between the DDSCAT results and Lorenz-Mie theory results divided with the Lorenz-Mie theory results.

Figure 2.2 is created to investigate the effect of size parameter, $x = ka = 2\pi a/\lambda$ on the DDA solution. This analysis is done by comparing the results obtained by DDSCAT7.0 with the results obtained from MiePLOT which is a computer software that calculates the exact Lorenz-Mie Theory results for spheres. This analysis is also for the comparison of the results with the results of a similar analysis present in the User’s manual of DDSCAT7.0 [18]. When ka increases the results diverge from the exact Lorenz-Mie solutions even though the N (Number of point dipoles) is increased. Figure 2.2 also summarizes the effect of N (number of point dipoles) on the convergence of the DDA solution with DDSCAT. From Figure 2.2 it

can be observed that as N increases to 17904 total scattering and absorption can be computed to accuracies of a few percent.

From similar observations about N , m (refractive index) and ka the following restrictions of DDSCAT are obtained.

As stated by Draine and Flatau [18] DDSCAT is not suitable for :

1. Large values of the size parameter x
 - a) $x = 2\pi a_{eff}/\lambda$
where $a_{eff} = (3V/4\pi)^{1/3}$
2. Very large values of the refractive index m

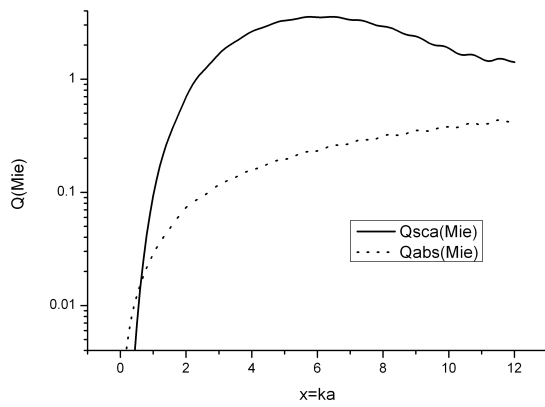
2.2.1 DDSCAT: What does it Calculate?

By using DDSCAT we can investigate many particle geometries under different conditions. More specifically the program calculates parameters that can give us idea about the properties of the system investigated. The problem is introduced to the program by the input parameter files such as:

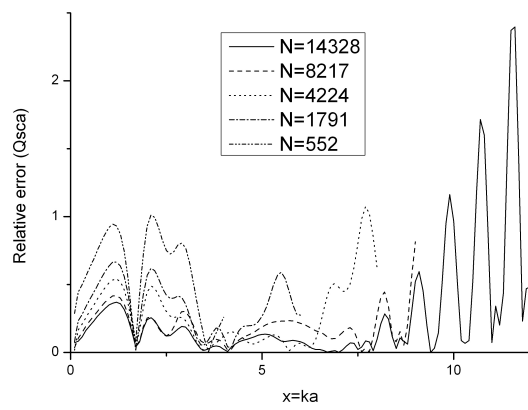
1. **ddscat.par** that includes information about:
 - a) Solution method (FFTW,GPFA), Tolerance;
 - b) Geometry, number of dipoles;
 - c) Orientation of geometry with respect to incident radiation;
 - d) Wavelength and polarization of incident radiation.
2. **diel.par**: Complex refractive index of target and the surrounding environment with respect to the wavelength.

The quantities calculated by DDSCAT are listed below:

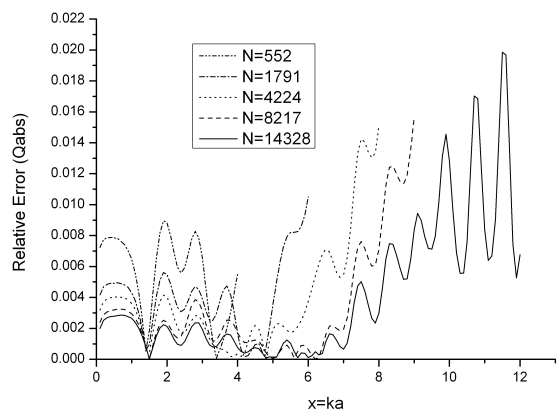
1. Absorption (Q_{abs}), scattering (Q_{sca}) and extinction (Q_{ext}) efficiency factors;
2. Phase lag efficiency factor;



(a) Exact values of Q_{sca} and Q_{abs} from the Lorenz Mie Theory



(b) Relative Error in Q_{sca} obtained by DDSCAT7.0



(c) Relative Error in Q_{abs} obtained by DDSCAT7.0

Figure 2.2: Scattering and absorption for a sphere with refractive index $m = 1.33 + 0.01i$

3. 4×4 Mueller scattering intensity matrix;
4. Radiation force, torque efficiency vector.

From the above listed quantities we will concentrate mainly on absorption (Q_{abs}), scattering (Q_{sca}) and extinction (Q_{ext}) efficiency factors. These are equal to absorption, scattering and extinction cross sections divided by πa_{eff}^2 . Moreover extinction efficiency factor is equal to the sum of absorption and scattering efficiency factors.

The program also makes spectral calculations, and calculations for multiple target orientations and varying particle sizes. It lists the above mentioned quantities for each wavelength, target size, target orientation. Besides, it gives orientationally averaged quantities. The sample input and output files are included in the Appendix B. Moreover, detailed information regarding the input and output of the program DDSCAT is given in the **User Guide for the Discrete Dipole Approximation Code DDSCAT7.0** [18].

When compared with the older versions of DDSCAT latest version of the DDSCAT: DDSCAT7.0 released in October 2008 has several additional capabilities like solving the light scattering problems from periodic targets and computing the electric field \mathbf{E} and magnetic field \mathbf{B} at desired locations [18]. The latter will be utilized actively in this thesis for the analysis of the near field effects.

2.2.2 Testing DDSCAT7.0

DDSCAT is a numerical tool hence the validity of it must be tested before using it for more complex geometries. Besides, the efficient use of the program is related with the correct modification of input parameter files. For all these reasons and to become more confident with DDSCAT7.0 some benchmark solutions are performed. It is widely known that due to their complexity analytical solutions of the scattering problems of particles with arbitrary shapes other than spheres are not available. Although, the state of the art of this field lays out plenty of experimental results for different geometries and analytical solutions for geometries slightly different than spheres the easiest method still goes along with the spheres.

For this purpose gold spheres with 60 nm diameter are modeled using DDSCAT7.0 and the results are compared with the results obtained from MiePLOT [42]. MiePLOT was originally

designed to provide a simple user interface (for PCs using Microsoft Windows) to the classic BHMIE algorithm for Lorenz-Mie scattering from a sphere given by Bohren & Huffmann in *Absorption and Scattering of Light by Small Particles* [5]. The BHMIE code is provided in Appendix C.

Figure 2.3 shows that the results obtained numerically by DDSCAT is different from the analytical solutions obtained by MiePLOT when the total number of dipoles representing the target is small. This is because when the number of dipoles decrease the size of each dipole increase and the geometry can not be modeled exactly. Moreover when the size of the dipoles increase it will not act like a dipole and modeling this small volume with a dipole polarizability will no longer be a valid assumption.

Therefore validity of the DDSCAT results strongly depend on the number of dipoles used to represent the target as well as the tolerance. However, it is observed that when dipole size is at about 1 nm which makes up a target composed of 113104 dipoles as shown with $N=113104$ in Figure 2.3 results become very close to values obtained by the Lorenz-Mie solutions.

Considering the size of the targets that is analyzed in this study and because of the reasons associated with the accuracy of the numerical method the dipole size is chosen to be 1 nm for the simulations.

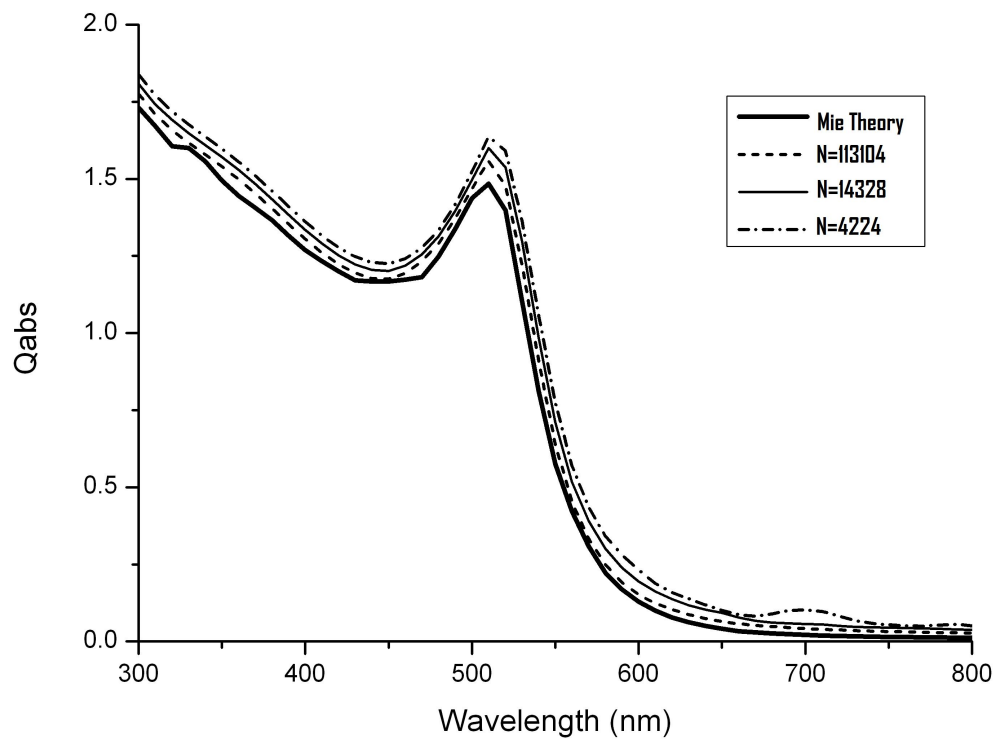


Figure 2.3: The effect of total dipole number N on the accuracy of DDSCAT7.0 (compared with Lorenz-Mie Theory)

CHAPTER 3

SOLUTION METHODOLOGY

3.1 Problem Definition

In this thesis dependent scattering of nanoparticles is investigated by a numerical tool. The information about dependent scattering of particles can be used in characterization of particles and their medium as well as the orientation of particles with respect to each other. Moreover, the enhanced fields due to near-field effects that are the main reasons of dependent scattering of particles cause the high absorption rates for some particles. This might be used in melting or fusing nanoparticles for a variety of applications.

With this motivation and the previously stated goal of the thesis which is to *investigate the dependent scattering of the nanoparticles in interaction* four problem cases are created:

1. Capped Gold Nanocylinders: Comparison with an Experiment,
2. Two Identical Gold Spheres,
3. Two Gold Spheres with Different Sizes: An Insight to Surface Effects,
4. Gold and Silicon AFM Tip and a Gold Nanosphere.

These cases are shown in Figure 3.1

These four cases are selected to basically investigate the performance of DDSCAT in estimating the absorption efficiency of closely positioned particles, the particles that are close to a surface like structure and finally the particles that are influenced by an AFM tip that is brought near them.

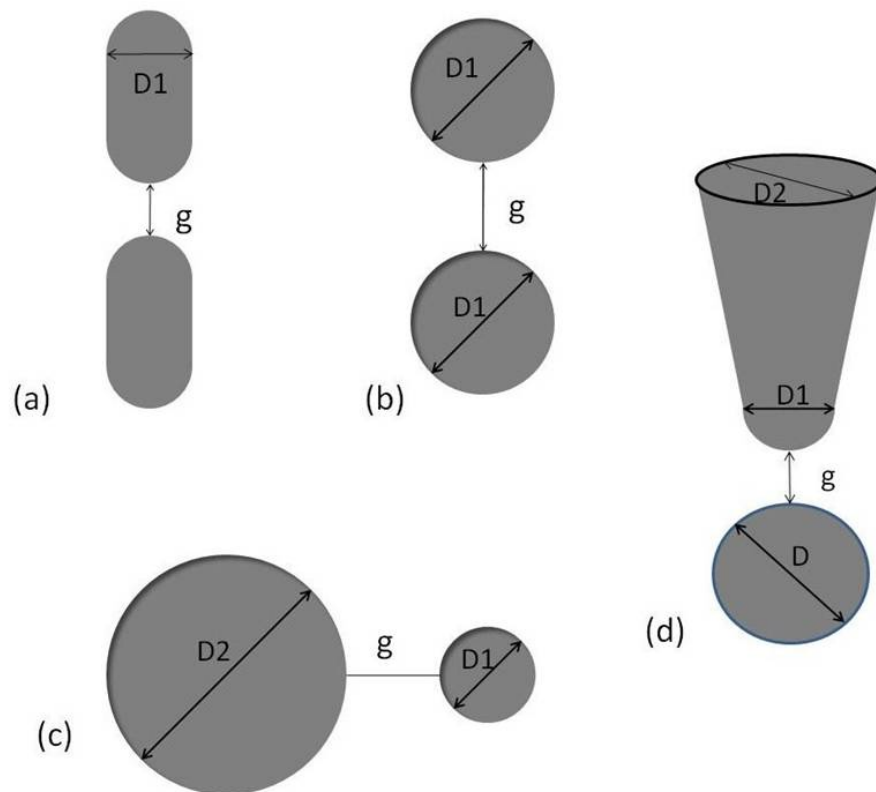


Figure 3.1: Representations of the four problem cases investigated in this study: (a) capped gold nanocylinders: comparison with an experiment, (b) two identical gold spheres, (c) two gold spheres with different sizes: an insight to surface effects and (d) gold and silicon AFM tip and a gold nanosphere

The case studies are to be discussed in detail in Chapter 4. Here we will focus to the solution methodology.

3.2 Methodology

In order to understand the dependent scattering and absorption regimes of the interacting particles a new method is used. DDSCAT gives the far field solutions, such as far field absorption, extinction and scattering efficiencies of the target particles. However, since the objective is to find how the scattering or absorption of any particle changes with the other particles in close proximity, near field scattering properties must be investigated. This will be done through the following steps:

1. **Target Generation:** DDSCAT7.0 is capable of producing the dipole representation of various geometries like spheres, cubes and ellipsoids. To investigate the targets with different geometries that are listed in the DDSCAT manual the codes included in the program can be modified. Besides to put targets having different geometries next to each other in a single target frame the files containing the dipole locations of individual targets are superposed in a single text file by giving an appropriate offset distance.
2. **Target Check:** Once the dipole representation of the target particle or particles are ready as a text file it must be checked. To check if the target generation is accurate the dipole locations of the target geometries are plotted in MATLAB. This gives the image of the target generated.
3. **Solution of Light Scattering Problem:** The location of each dipole composing the target is read by the program DDSCAT with the command FROM_ FILE. DDSCAT7.0 will be executed with the desired geometry and incident light with the desired wavelength, direction and polarization.
4. **Near Field Analysis:** DDFIELD, which is a new routine inserted in DDSCAT7.0 to calculate Electrical and Magnetic Fields at desired points inside and outside the particles, is executed for the incident light with the desired polarization file. This will provide the electric and magnetic fields on selected locations. By using it **E** and **B** vectors on the grids of the imaginary surface (see Figure 3.3) enclosing the investigated geometry are obtained.

5. **Poynting Vector:** Profiles of electric field and magnetic fields are used to obtain Poynting vector, that represents the radiative flux.
6. **Integrated Poynting Vector:** The Poynting vector is integrated on the imaginary surface enclosing only the investigated geometry.
7. **Dependent Scattering:** The integrated Poynting vector gives the absorbed energy by the absorbing geometries in the enclosed volume.

Detailed information about the target generation will be given in the next chapter. The algorithm used for the above explained procedure except for the target generation is given in Figure 3.2. The governing equations used in the described method are given in the next section.

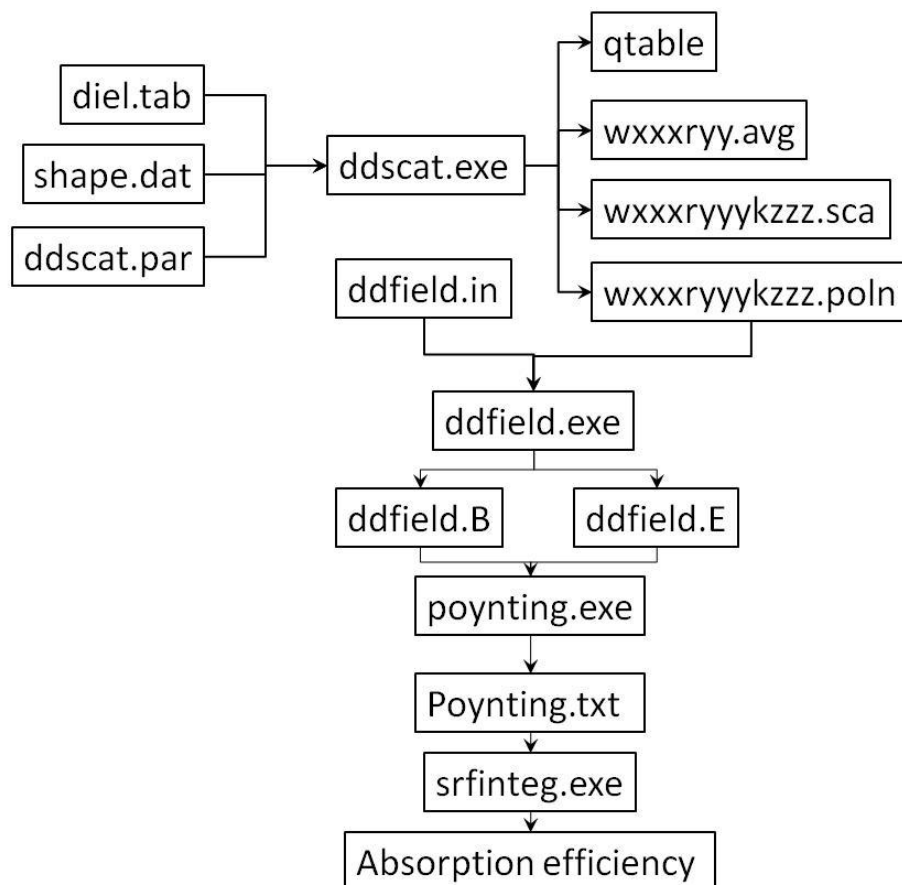


Figure 3.2: The algorithm of Integrated Poynting Vector Approach

3.3 Governing Equations

As stated before the behavior of electromagnetic waves are governed by the Maxwell equations. Energy conservation obtained over the modification of the Maxwell equations leads to the Poynting's theorem that represents *the power balance or conservation of energy for electromagnetic fields* [65].

In other words, Poynting's theorem is nothing but the continuity equation for the electromagnetic fields. It simply states that the power supplied to a given volume is equal to the rate of change in the stored energy and the power leaving the volume as represented by the following equation [29, 41].

$$\vec{q} + \nabla \cdot \vec{S} = 0 \quad (3.1)$$

with [14]

$$\vec{q} = \frac{1}{2} \omega \epsilon'' \epsilon_0 \vec{E} \vec{E}^* \quad (3.2)$$

and the Poynting vector

$$\vec{S} = \frac{1}{2} \text{Re}[\vec{E} \times \vec{H}^*]. \quad (3.3)$$

The magnetic field vector is related to magnetic induction vector through

$$\vec{H} = \frac{\vec{B}}{\mu_0} \quad (3.4)$$

From the divergence theorem

$$\iiint_V \nabla \cdot \vec{S} dV = \iint_A \vec{S} \cdot \vec{n} dA. \quad (3.5)$$

Hence, the total absorption becomes

$$P_{abs} = - \iint_A \vec{S} \cdot \vec{n} dA. \quad (3.6)$$

Therefore, in order to calculate the total absorption rate or efficiency of a specified target it is possible to integrate the Poynting vector over the surface of the target itself. If the target is located in a non absorbing medium it is also possible to obtain the absorption of the target by simply integrating the Poynting vector over any surface fully enclosing the target geometry. This imaginary surface enclosing the target geometry is shown in Figure 3.3.

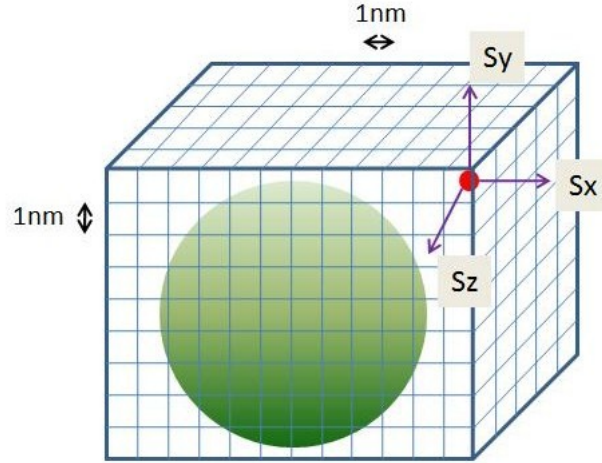


Figure 3.3: The model of the imaginary grid surface enclosing the investigated target geometry

To calculate the efficiency the amount of incident power is also required. Remembering that for plane electromagnetic waves

$$\vec{B}_0 = \frac{\vec{E}_0}{c}$$

incident electromagnetic power entering the volume can be calculated as

$$P_{inc} = \frac{E_o^2}{2 \times c \times \mu_o} \times A_{cs}$$

where A_{cs} is the cross sectional area of the target with the normal vector parallel to the incident field.

This section summarized the physical theory behind the Integrated Poynting Vector Approach. To be more confident about the accuracy of this approach several trials have been performed.

3.4 Integrated Poynting Vector Approach (IPVA): Does the approach work?

By using the governing equations a method has been developed to calculate the absorption efficiencies of individual particles in the existence of other particles in its neighborhood. This method is based on the numerical integration of the Poynting Vector on an imaginary surface enclosing the absorbing medium. Thus it can be named *Integrated Poynting Vector Approach*, based on Equation 3.6.

In order to check the accuracy of the numerical integration, the absorption efficiency of a single isolated sphere has been calculated, and the results are compared with those obtained by the Lorenz-Mie theory. Another procedure for testing the accuracy of this new method is to use it for an empty volume. Since an empty volume, either atmosphere or vacuum, does not absorb, the absorption efficiency is expected to be zero. Figure 3.4 shows the accuracy of the proposed method in calculating the absorption efficiency of spherical nanoparticles and a non-absorbing media.

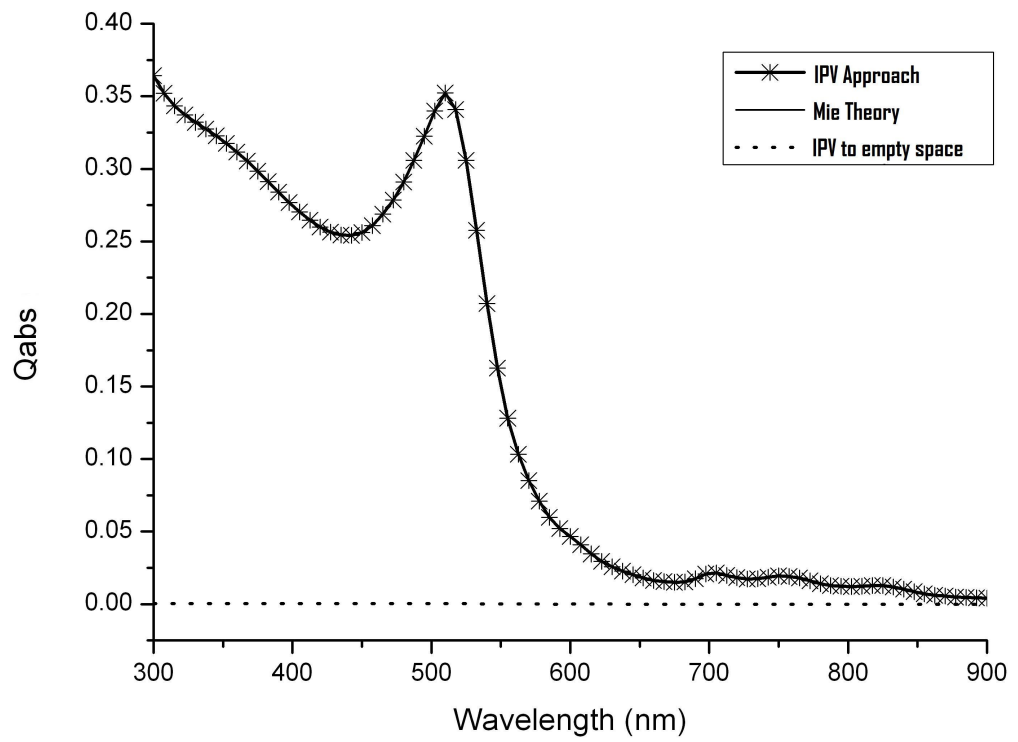


Figure 3.4: Testing the accuracy of Integrated Poynting Vector Approach

CHAPTER 4

CASE STUDIES

The idea is to test the effectiveness of DDSCAT in dependent scattering calculations. For this purpose four different case studies are designed.

The first one is the study of optical scattering properties of capped gold nanocylinders. This case is designed to check if DDSCAT solutions give similar trends with the experiments. The second case study, *two identical gold nanospheres*, is selected for the better understanding of limits of dependent scattering and the polarization effects of incident light. The third study, *two gold spheres having different sizes*, is developed to analyze the influence of size and shape of the particles on the scattering characteristics of each other as well as to gain an insight to surface effects. Finally the last study is the modeling of a gold nanoparticle and an AFM tip scattering which is selected to investigate if it is possible to observe the tip effects on the nanoparticle by using DDSCAT.

4.1 Case I: Capped Gold Nanocylinders: Comparison with an Experiment

The scattering of nanorods, nanocylinders and ellipsoids are investigated both experimentally and numerically by different researchers [20, 30, 36, 54]. They are important in scattering experiments because due to their geometry they have unique scattering characteristics. Unlike spheres they contain two plasmon resonance modes: one along the axis and other perpendicular to the axis.

Hence, these particles are easy to recognize from their scattering behaviors when the light with the right polarization is incident on them. Moreover, when more than one of these particles are placed next to each other it is easier to understand the dependent scattering effects due to

multiple resonance modes that are so distinct from each other.

The experimental work is performed by Hastings et al. (Private Communication with Todd Hastings from University of Kentucky). They investigated gold nanorods that are 110 nm long by 40 nm wide and situated on BK7 (optical glass) substrate with a 30 nm thick layer of indium tin oxide (ITO). From Figure 4.1 it is seen that the gold nanorods are actually rounded rectangles. They are arranged in a 2D array with a pitch of 150 nm along the length of the rods and a pitch of 250 nm along the short axis.

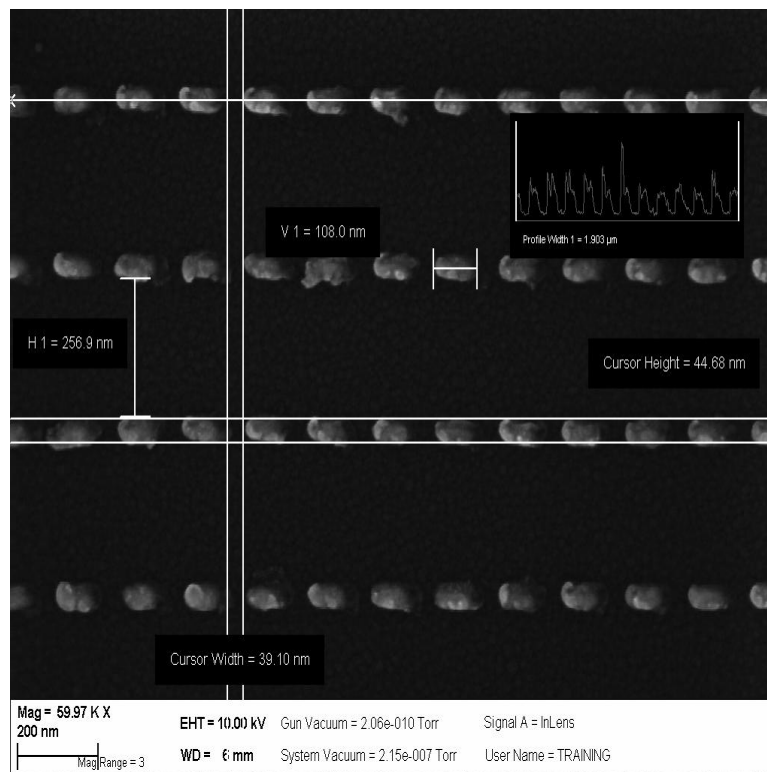


Figure 4.1: Real image of gold nanorods (*private communication with Todd Hastings and M. Pinar Mengüç from University of Kentucky research program*).

This results in electromagnetic coupling along the long axis, but not the short axis. To observe the coupling, light having three different polarizations: parallel, perpendicular and 45 degrees (to the long axis) is sent to the target.

To check if a similar trend is obtained with DDSCAT7.0 gold capped nanocylinders that best describe the rounded rectangles are chosen as shown in Figure 4.2. Since there is no existing routine of DDSCAT that creates the dipole representation of multiple capped nanocylinders the following procedure is followed:

1. By using the *CALLTARGET* (which allows the user to generate targets interactively by leaving behind an ASCII file *target.out* which is a list of occupied lattice sites in the last generated target) and *CYLNDRCAP* (routine that creates the dipole representations of capped cylinders) the dipole array representing a capped cylinder with desired dimensions is generated.
2. The dipole array for a single cylinder is copied and moved with a certain offset. The dipole arrays of the two cylinders are placed in a single file.
3. By using this file and the command *FROM_ FILE*, that causes DDSCAT to read the target geometry and composition information from a file instead of automatically generating it, the target is introduced to the program DDSCAT7.0.

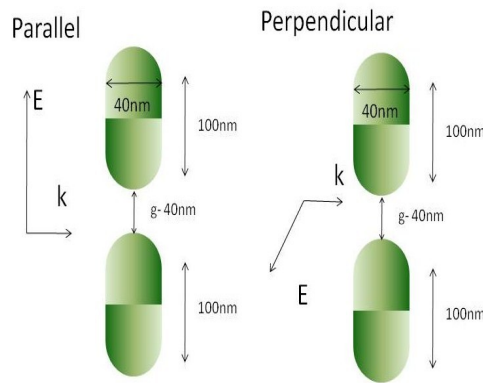


Figure 4.2: Non-periodic model of gold cylinders used in DDSCAT.

The capped gold nanocylinders are positioned as shown in Figure 4.2 and the incident light is sent with the previously explained polarizations: parallel, perpendicular and 45 degrees to the long axis of cylinders. The information about the incident light, orientation of target with respect to incident light and the solution method are all given by the file *ddscat.par* and the information about the target's dielectric constant is given by *diel.tab*.

Due to several restrictions about the dipole number it is not possible to model surfaces using DDSCAT. Thus, it is not expected to obtain the same results with DDSCAT. However, we may still expect similar behavior even if the incident light hits directly the particles and does not get scattered by a surface first.

4.2 Case II: Two Identical Gold Spheres

It has been a long time since Ivezic and Menguc made a similar research on dependent and independent scattering regimes using DDA . They used DDSCAT for their DDA calculations and found that the dependent scattering exists for a system of two particles when the distance between them, d , is larger than three times the radius of a of a single sphere [32]. They noted that the dependent scattering of particles can be used for the investigation of agglomeration rates of nanoparticles.

Here in this part of the thesis similar analysis is performed. The purpose is to observe the limits of dependent scattering just as Ivezic and Menguc did and to investigate the effects of the polarization (in this case parallel and perpendicular) of the incident light on the absorption efficiency of individual particles. The scattering target is illustrated in Figure 4.3.

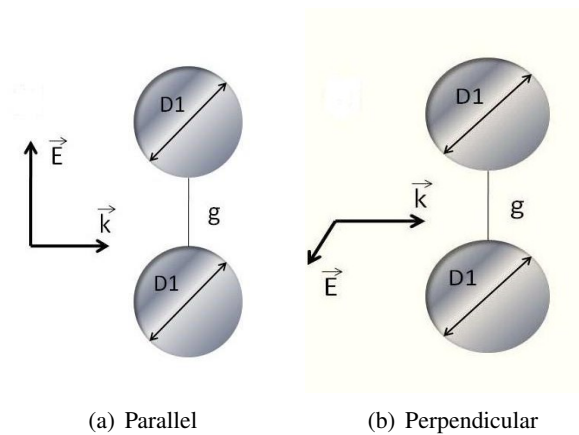


Figure 4.3: The model of two identical $D = 20$ nm gold nanospheres in interaction when the incident light is polarized parallel and perpendicular to the axis connecting them.

The targets are generated by using one of the routines supplied by DDSCAT7.0. The routine is named SPHERES_N and allows the dipole modeling of multiple spheres with a certain offset as the target. Therefore, for this case study the CALLTARGET option and the superposition of dipole locations files are not used.

Again the information about the incident light like parallel or perpendicular polarization, orientation of target with respect to incident light and the solution method are all given by the file *ddscat.par* and the information about the target's dielectric constant is given by *diel.tab*.

4.3 Case III: Two Gold Spheres with Different Sizes: An Insight to Surface Effects

After investigating the effects of identical gold nanospheres on each other, the next step is to investigate what happens if the size of one of the spheres increases compared to the other and starts acting like a surface. This is important in simulating the applications where particles must rest on a substrate. Although modeling particles in vacuum or air is suitable for some scattering experiments where particles are in solutions, for the intended applications of the present study such as AFM tip assisted nanomanufacturing or spectrally selective heating of nanoparticles where particles rest on a substrate, this will not be sufficient.

This case study is for investigating the effects of a surface like nanoparticle on other nanoparticles. The analysis is performed by gradually increasing the size of the bigger sphere. Moreover, it is aimed to see the effect of the position of the bigger sphere relative to the smaller one and the incident light. The dimensions of the spheres considered in the DDSCAT solution are presented in Figure 4.4.

The targets in Figure 4.4 are generated with the command SPHERES_ N, which was also explained in the previous section.

When the diameter of the larger sphere reaches 100 nm, half of the sphere is omitted. This reduces the number of dipoles significantly which will increase the speed of the calculations considerably and by this way the second sphere looks much like a curved surface as shown in Figure 4.5.

This kind of targets are generated by a similar approach as explained in Section 4.1 but this time instead of cylinders spheres are generated separately with ELLIPSOID command and the dipoles making up the half of the bigger sphere are omitted.

4.4 Case IV: A Gold Nanosphere and a Gold or Silicon AFM Tip

The field enhancement of a metallic probe is caused mainly by the localized surface plasmon mode excited at the apex of the probe by an evanescent field.

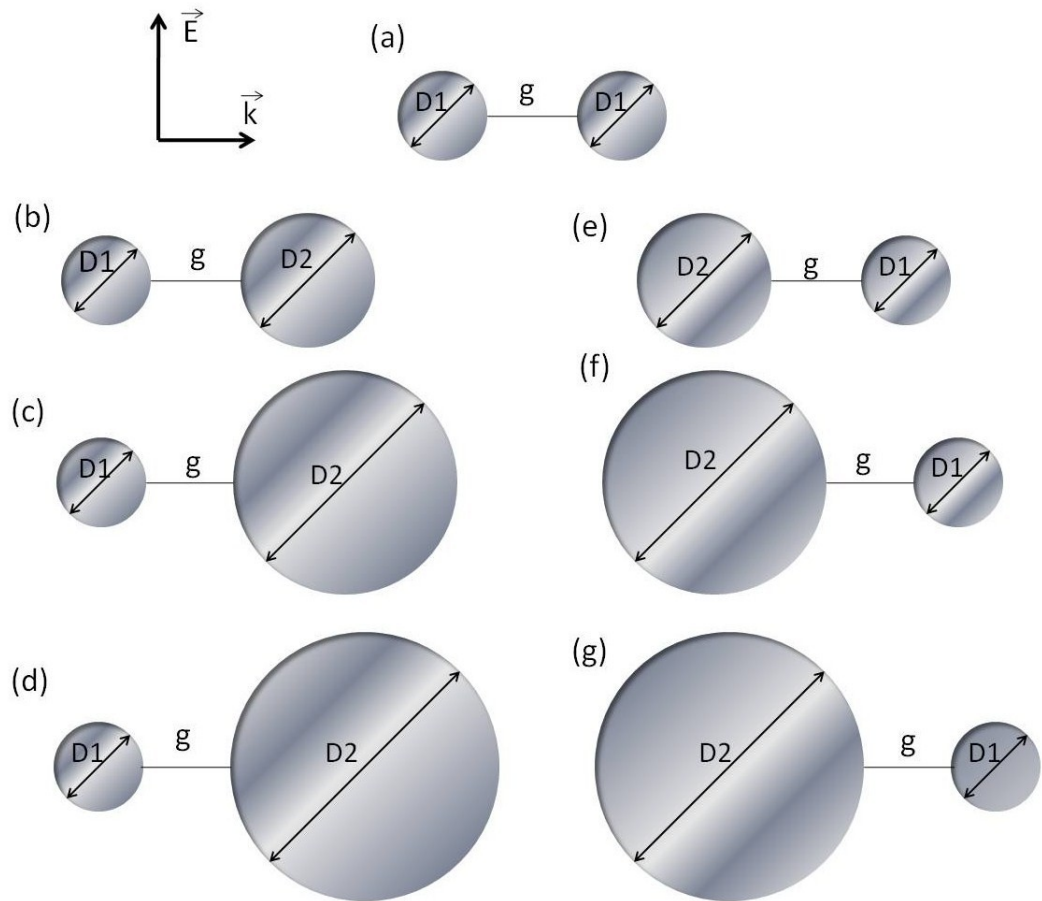


Figure 4.4: Two spheres next to each other. The small sphere with 20 nm diameter and the bigger sphere 30 nm (cases b and e), 50 nm (cases c and f) and 60 nm (cases d and g) diameter

Hawes et al. showed that if the conditions about the threshold interaction time between the probe and the particle and the probe height requirements for the particle to melt or evaporate are satisfied, it is possible to melt and evaporate nanosized gold particles in a targeted area using SPR and an AFM probe in the near field [27].

The purpose of this case study is to experience if it is possible to observe this kind of behavior in nanoparticles by using DDSCAT. If that can be done it may be possible to test the cases before experimenting them so that sources are used in a more effective way.

Of course it is not possible to see the melting or evaporation of particles or the time required to melt the particles by DDSCAT. Yet still some information related with this can be achieved.

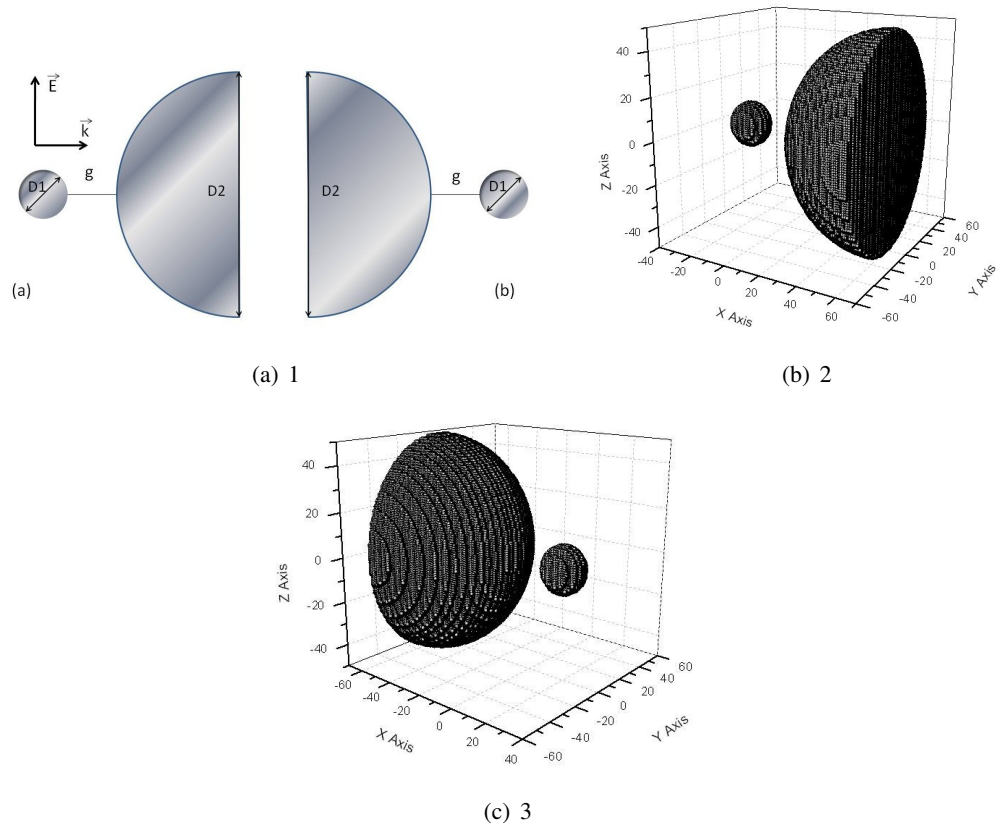


Figure 4.5: Dipole representation of a 20 nm diameter sphere and 100 nm diameter half sphere.

For example absorption efficiency of a nanoparticle is a good indicator about its evaporation or melting behavior.

Dipole locations of the prescribed shapes by DDSCAT7.0 can be obtained by executing CALLTARGET option described before. When it is executed user chooses one of the dipole generation routines for prescribed geometries and enters the dimensions as well as the orientation. The program gives the dipole locations of the geometry introduced as an output.

Dipole locations of a conical tip with a capped end in Figure 4.6 is obtained by modifying an existing routine called CYLNDRCAP that creates the dipole representation of a homogeneous, isotropic finite cylinder with hemispherical end caps. Later the dipole representation of a single sphere is also obtained and these two files are superposed in a single file.

In this case study the effects of the probe material on the absorption spectra of the gold sphere are analyzed. The effects of probe dielectric constant (gold, silver or silicon) are discussed by

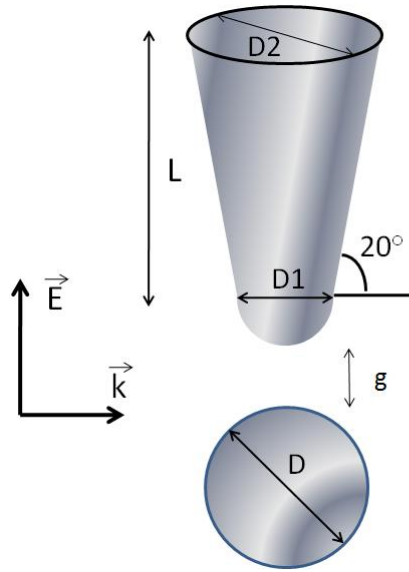


Figure 4.6: A representation of the AFM tip and nanosphere modeled in DDSCAT

Hawes [26] in her Ph.D. thesis. Here, the study is restricted to the silicon and gold probes, with $D_1 = 20$ nm and D_2 being 50, 100 and 150 nm.

CHAPTER 5

RESULTS AND DISCUSSION

To test the proposed methods, we have run a number of test cases. For these, simulations have been performed by running DDSCAT7.0 on an Intel Quad-Core 9550 2.83 GHz computer with 4 GB RAM. However, each simulation is performed by a single core since it is not possible to parallelize DDSCAT for single orientation calculations.

All the results presented below are original, and for that reason there was no way to compare them against any benchmark results. The objective here is to present the dependent absorption and scattering trends for these four selected cases.

5.1 Case I: Capped Gold Nanocylinders: Comparison with an Experiment

The absorption efficiencies of two capped gold nanocylinders for the incident light with parallel, perpendicular and 45 degree polarization are given in Figures 5.1, 5.2, 5.3. The polarization direction has a great importance in the field enhancements.

Figure 5.1 shows that at about 750 nm plasmon resonance occurs. This is due to plasmon oscillations along the long axis of the nanocylinders. Besides since there are two nanocylinders aligned vertically along the axis and along the polarization of the incident light, inter particle coupling effects enhance the near fields. For this reason, the absorption efficiency at the plasmon resonance is increased considerably.

Figure 5.2 indicates that at about 500 nm another plasmon resonance exist. This is due to plasmon oscillations along the short axis of the nanocylinders. However, unlike the parallel polarization, at perpendicular polarization the absorption efficiency even at the plasmon res-

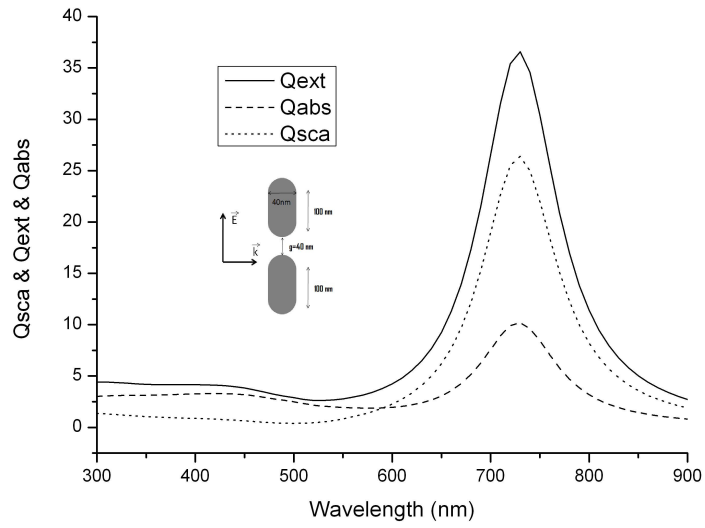


Figure 5.1: Scattering, absorption and extinction efficiencies of capped gold nanocylinders illuminated with light with polarization parallel to the long axis.

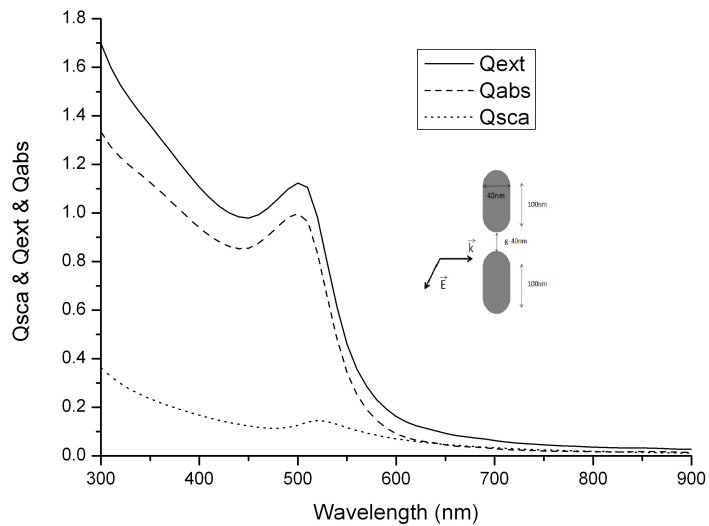


Figure 5.2: Scattering, absorption and extinction efficiencies of capped gold nanocylinders illuminated with light with polarization perpendicular to the long axis.

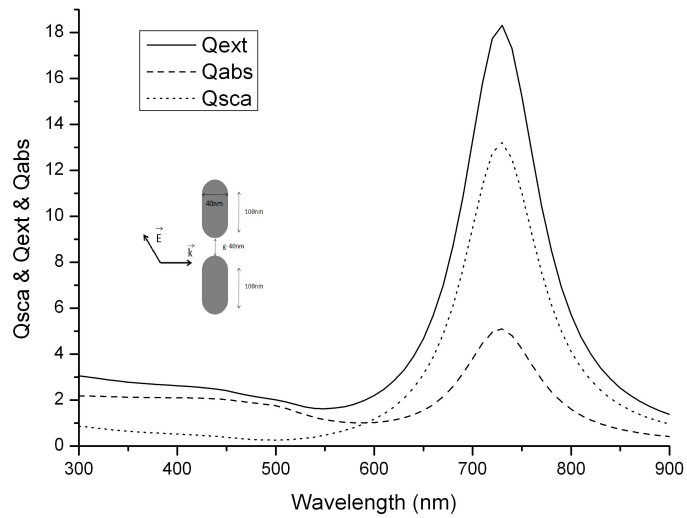


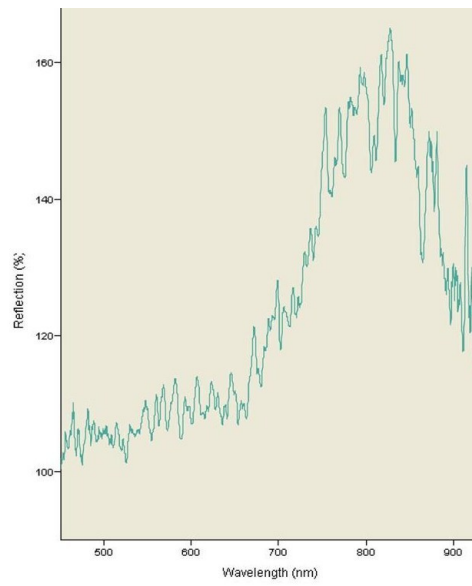
Figure 5.3: Scattering, absorption and extinction efficiencies of capped gold nanocylinders illuminated with light with polarization 45 degrees to the long axis.

onance is relatively small since there exist no interparticle coupling effects along the short axis.

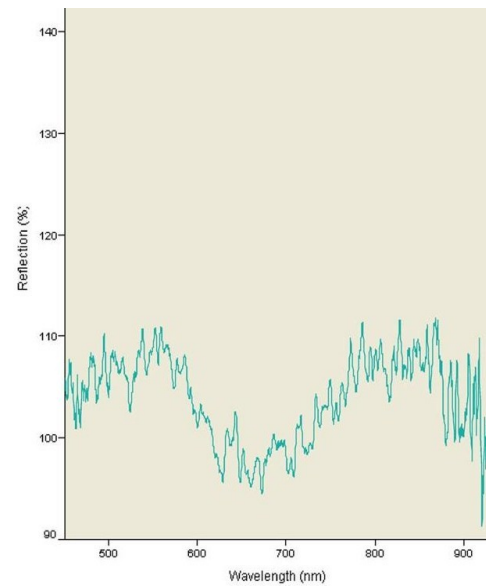
Figure 5.3 shows what happens when the light with 45 degree polarization is sent to the target of capped nanocylinders. 45 degrees polarization is nothing but the superposition of light beams with perpendicular and parallel polarizations. Thus, this figure contains features of both Figure 5.1 and Figure 5.2. From these figures it is obvious that maximum absorption occurs at parallelly polarized incident field then comes 45 degrees polarization and perpendicular polarization.

Figure 5.4 illustrates the experimental results for the reflection percentage.

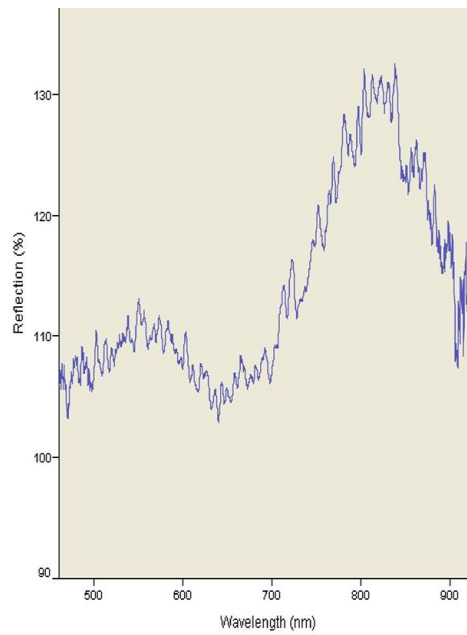
These results are similar to the trends obtained by the experimental studies performed by Eugene Donev, Todd Hastings and M. Pinar Mengüç from University of Kentucky. As stated before it is not reasonable to expect total resemblance of the results obtained by experimental and DDSCAT since it is not possible to model surface in DDSCAT (*Private communication Pinar Menguc - Todd Hastings from University of Kentucky*).



(a) Parallel Polarization



(b) Perpendicular Polarization



(c) Polarization 45 degrees

Figure 5.4: Experimental reflection percent of rounded gold rectangle array illuminated with light with parallel, perpendicular and 45 degrees (to the long axis) polarizations.

5.2 Case II: Two Identical Gold Spheres

Figure 5.5 shows the absorption efficiency of two gold nanospheres close to each other when the light with perpendicular or parallel polarization is sent to the particles. Figure 5.5(a) depicts that when the parallel polarization is sent to the particles the absorption efficiency of the target is increased compared to that of a single sphere with the size equal to the volume of two spheres being investigated ($r = a_{eff}$). This is an evidence to interparticle coupling effects. Besides as the gap between the particles is increased this effect reduces and thus the absorption spectra approaches the spectra of a single sphere with the effective radius. This is observed when the gap between the particles is at about 100 nm.

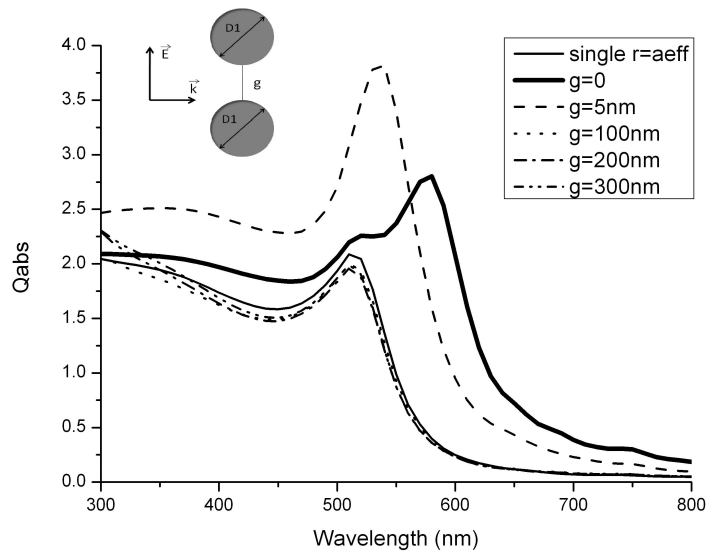
This is not surprising because Ivezic and Mengüç have already noted that *mutual interaction of the spheres does not affect the absorption when the ratio of their distance to radius $c = d/a$ is greater than 3*. For this problem case radius of the spheres is 30 nm and when the gap exceeds 90 nm the dependent scattering can not be observed.

Another important feature of the results is related to the polarization of the incident light. When the polarization of incident light is parallel to the axis connecting the spheres near field effects enhance the absorption, however when the polarization is perpendicular absorption efficiency is decreased by the destructive interference of near field fields.

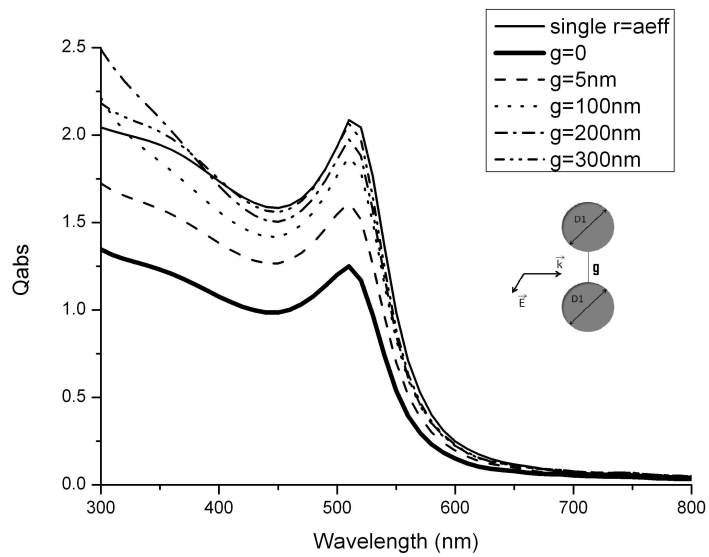
Figure 5.6 on the other hand displays the optical absorption spectra of one of the two spheres. It also includes the absorption spectra of a single sphere when no other particle exist. The absorption spectra of a single sphere supports the idea: inter-particle coupling effects cause the change of the absorption of a single sphere and this strongly depends on the polarization of the incident light with respect to the particle orientations.

5.3 Case III: Two Gold Spheres with Different Sizes: An Insight to Surface Effects

It is hard to model a surface in DDSCAT due to several limitations about dipole size and number in the target frame. Therefore, this case study is designed for understanding what happens when a small surface like structure is present near a nanoparticle.

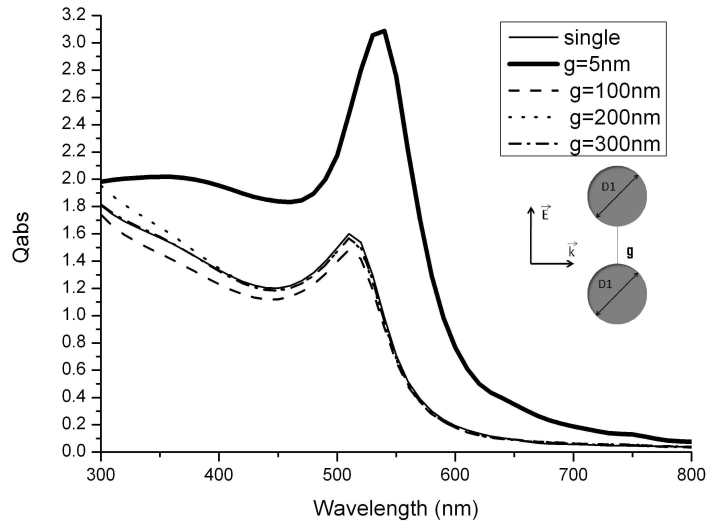


(a) Incident light is polarized parallel to the axis connecting the spheres.

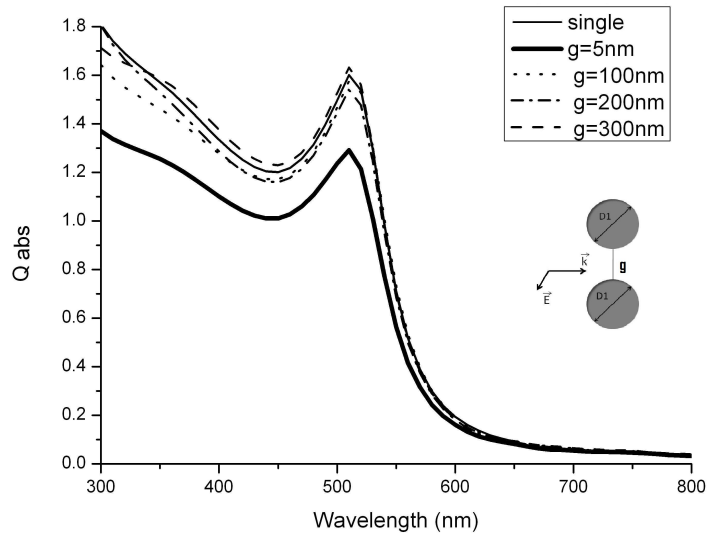


(b) Incident light is polarized perpendicular to the axis connecting the spheres.

Figure 5.5: Dependent absorption spectra of two identical gold nanospheres with varying interparticle distance (g) when the incident light is polarized parallel and perpendicular to the axis connecting the spheres.



(a) Incident light is polarized parallel to the axis connecting the spheres.



(b) Incident light is polarized perpendicular to the axis connecting the spheres.

Figure 5.6: Absorption spectra of one of the spheres calculated with Integrated Poynting Vector Approach when the incident light is polarized parallel and perpendicular to the axis connecting the spheres as the gap (g) between the particle changes.

This is done by slightly increasing the size of the second sphere that was present in the previous case study. This time, however the wave vector of the incident field \vec{k} , is not perpendicular to the axis connecting the two spheres but it is parallel. Besides, the analysis is done for single polarization state since the two orthogonal polarization states will be experienced exactly the same by the target particles due to symmetry of the target geometries.

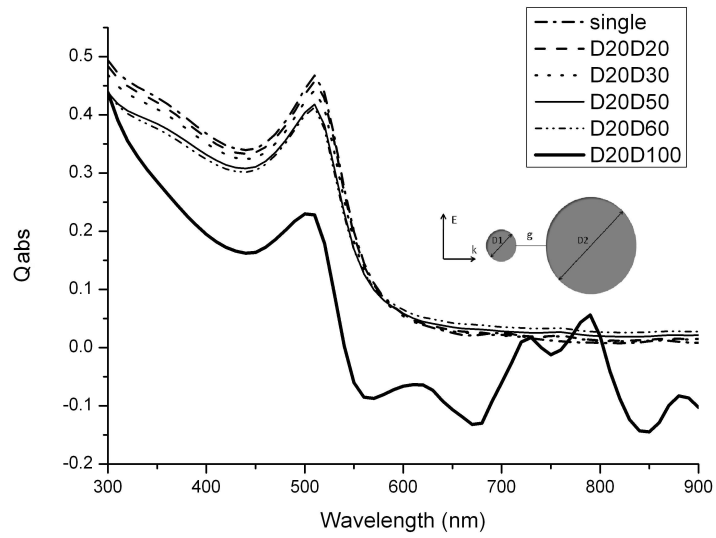
Figure 5.7 shows what happens to the absorption efficiency of the small sphere when the size of the sphere near to it changes. While Figure 5.7(a) presents the results for the case when the small sphere is placed before the larger one in the direction of the incident light. Figure 5.7(b) presents the results for the opposite configuration.

Figure 5.7(a) shows that when the small sphere is placed before, absorption efficiency of it decreases slightly as the size of the neighboring particle increases. This can be due to the backscattering effects of the bigger particle growing with the particle size.

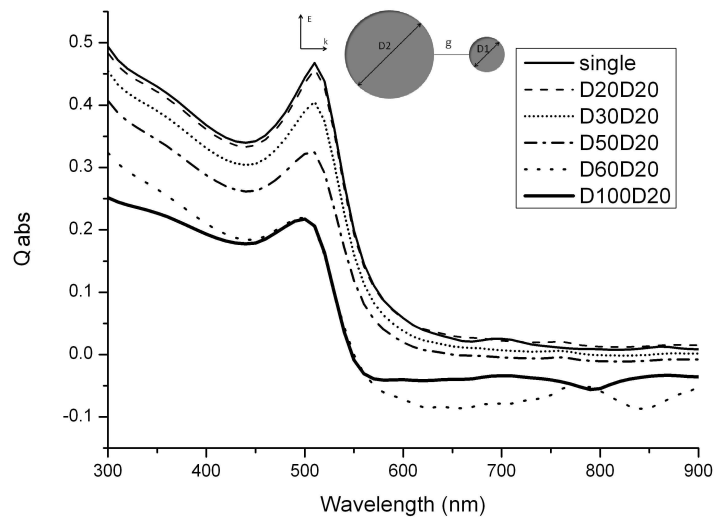
However, the effect of the bigger particle becomes more pronounced when it is placed before. This significantly reduces the absorption efficiency of the smaller particle as can be seen from Figure 5.7(b). The reason may be that not all of the incident light reaches small sphere as it is first scattered and absorbed by the bigger one. The intensity of the light reaching the small nanosphere decreases as the bigger sphere gets larger and larger since the amount of the absorbed and scattered light is directly related with the size.

The important fact about these two figures is that as the size of this second sphere increases a lot, negative values for the absorption efficiency is obtained. This can also be observed from figure 5.7. For these cases IPVA analysis is repeated by taking a bigger control surface around the investigated particle. However, no significant changes in the results is observed. Therefore, the possible reason for this error can be due to the accumulation of numerical errors especially as the size increases. This happens because the number of dipoles increases tremendously as the size of the target changes.

In order to check the possible reasons for this outcome an empty region close to the target in the solution domain is investigated with Poynting Integral Method. The absorption efficiency values of this region is found to be changing from positive to negative in that spectrum but in the order of 10^{-2} to 10^{-3} . However, when this region is chosen far away from the target absorption efficiency approaches to zero. This also supports the idea about numerical errors,



(a) The absorption efficiency of the smaller sphere when the small sphere is located before in the direction of incident light.



(b) The absorption efficiency of the smaller sphere when the bigger sphere is located before in the direction of incident light.

Figure 5.7: Absorption spectra of the small spheres calculated with Integrated Poynting Vector Approach when the incident light is polarized perpendicular to the axis connecting two spheres having different sizes.

because the effects of dipoles and the numerical errors related with them diminishes with the increasing distance.

Another reason may be related to definition of the absorption efficiency in the calculations. It is the ratio of the absorbed power to the incident power and the incident power is calculated by only considering the incident radiative flux. However, when working with systems of particles as in this case, scattered radiation from other particles must also be taken into account, since this can also be treated as an incident power coming from another source.

5.4 Case IV: A Gold Nanosphere and a Gold or Silicon AFM Tip

The effects of an AFM tip like structure on the absorption spectra of a gold nanosphere are investigated. Figure 5.8, 5.9, 5.10 refer to the cases when a gold tip is present and Figure 5.11, 5.12, 5.13 represent the cases when silicon tip is present.

In Figures 5.8, 5.9, 5.10 multiple resonance peaks can be observed. This is because the target is being composed of two geometries, a capped cone representing the AFM tip and a nanosphere. Of course these two geometries have different resonance wavelengths due to the shape effects as discussed before. The resonance at the longer wavelength is due to the longitudinal plasmon oscillations of the capped cone (AFM tip). This can easily be recognized because as the length of the cone increases this peak also moves to longer wavelengths.

In reality AFM tips are much longer than 150 nm. However, with DDSCAT it is not possible to model so long nanostructures due to significant increase in the number of dipoles required to model the target. Hence, the simulations are performed for 50, 100 and 150 nm tips. Thus, it is expected that the longitudinal resonance will vanish in real size AFM applications and this peak causing a very high absorption efficiency may be disregarded.

If analyzed carefully it is possible to see the new peaks arising when 150 nm tip is modeled. These peaks might be due to near field enhancements. Although the peaks are small compared to the resonance peak of a single sphere they might increase when the tips get longer.

Figures 5.11, 5.12, 5.13 have no other plasmon peaks on the other hand. This is because Si is not a metallic particle and does not show a strong resonance condition. However, again because of the inter particle coupling effects when the distance between the probe and the

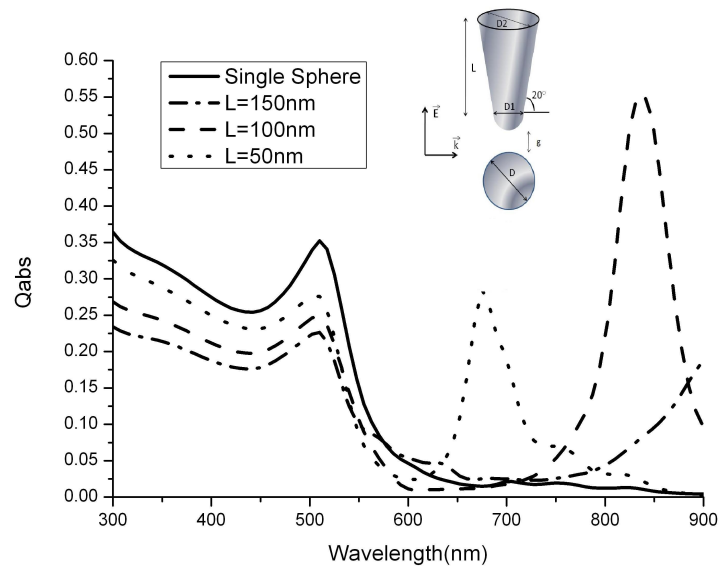


Figure 5.8: Q_{abs} of a $D = 15$ nm Au nanosphere calculated with IPVA when the Au tip is 10 nm away.

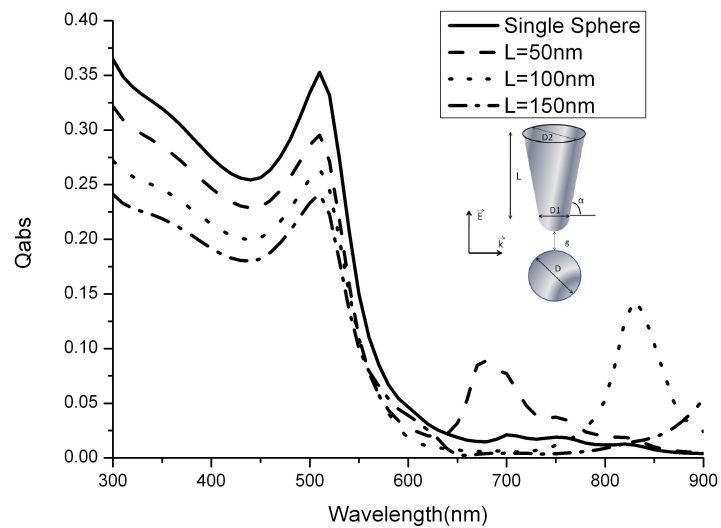


Figure 5.9: Q_{abs} of a $D = 15$ nm Au nanosphere calculated with IPVA when the Au tip is 20 nm away.

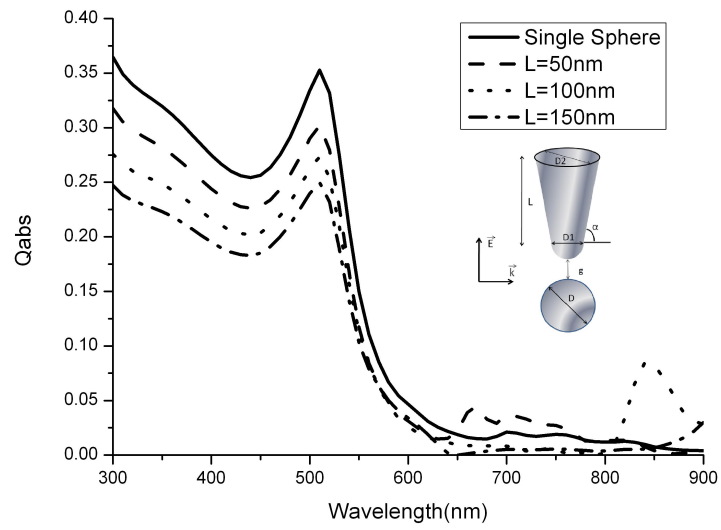


Figure 5.10: Q_{abs} of a $D = 15$ nm Au nanosphere calculated with IPVA when the Au tip is 30 nm away.

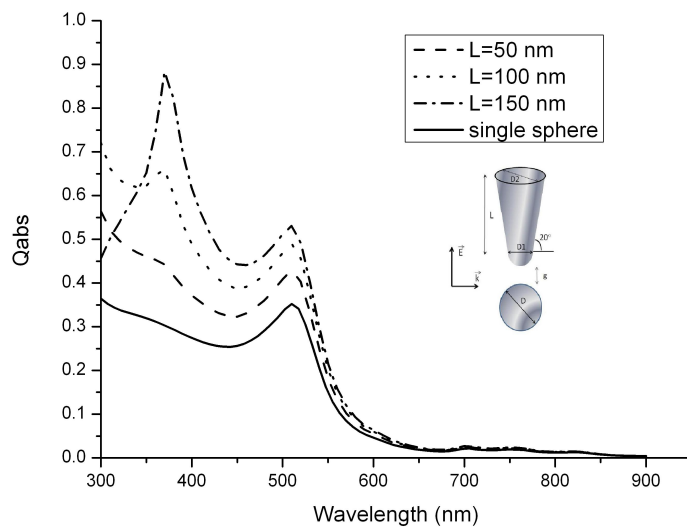


Figure 5.11: Q_{abs} of a $D = 15$ nm Au nanosphere calculated with IPVA when the Si tip is 10 nm away.

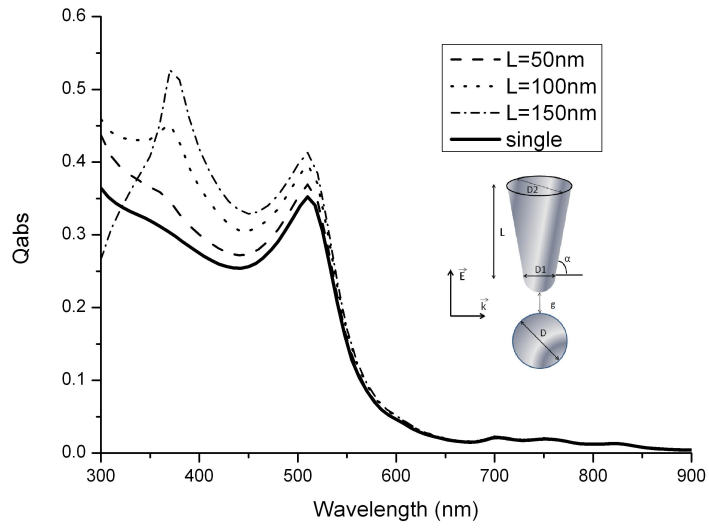


Figure 5.12: Q_{abs} of a $D = 15$ nm Au nanosphere calculated with IPVA when the Si tip is 20 nm away.

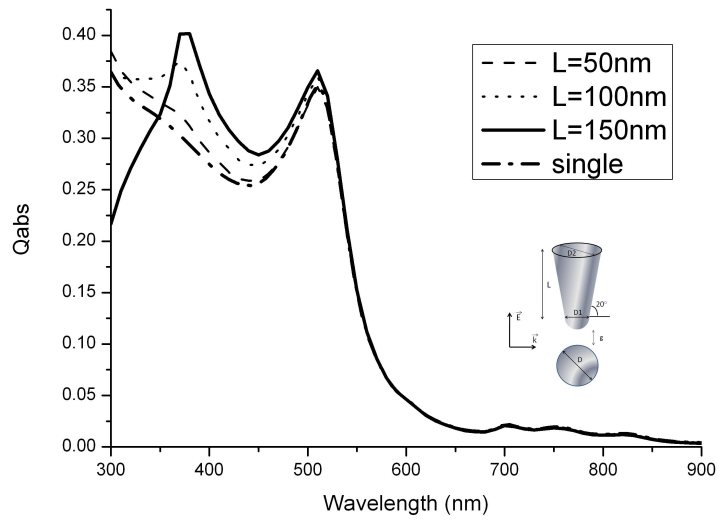


Figure 5.13: Q_{abs} of a $D = 15$ nm Au nanosphere calculated with IPVA when the Si tip is 30 nm away.

particle is small enough the absorption efficiency of a single gold nanosphere is increased, this can be seen from Figure 5.11. This effect reduces as the gap between the probe and the particle increase (see Figures 5.12 and 5.13).

CHAPTER 6

CONCLUSIONS

6.1 Summary

The plasmon resonance wavelength and the absorption efficiency of the individual particles depend on polarization and direction of the incident light, shape and size of the surrounding particles, distance between them, and their orientation with respect to each other and incident radiation.

The solutions obtained with DDSCAT7.0 and Integrated Poynting Vector Approach show that DDSCAT can be used for the estimation of scattering and absorption of nanoparticles are affected by the near fields of other particles in their close proximity.

From our simulations, if the light with appropriate polarization is sent to the particles the absorption can be increased significantly by the near field effects of the neighboring particles. It is observed that as the distance between the particles increases however, dependent scattering becomes less pronounced.

Moreover the results showed how the the plasmon resonance excitation of particles affect the absorption of other particles by creating a near field effect. Although effects of dependent scattering was investigated by Ivezic and Menüç this effect of surface plasmon was not investigated [32].

DDSCAT used for numerical analysis in this study has some limitations. These are discussed in the next section. Recommendations for improving the method and some future research ideas are given in the next chapter.

6.2 Limitations

Applications involving light scattering from nanoparticles often deals with a particle positioned on a substrate. Therefore, it is essential to model the substrate in the numerical simulations. However, this kind of modeling results with a very large number of dipoles. Even a smallest slice of substrate in the shape of a rectangular prism having the dimensions of 500nmX500nmX30nm is modeled with 7,500,000 dipoles if the dipole size is chosen as 1nm. When compared to 1,000,000, which is the maximum number of dipoles that a model can contain given by the DDSCAT7.0 User's Guide, this number is unacceptable for the DDSCAT simulations. This limitation of number of dipoles is a results of the available RAM of computers of today's technology and DDSCAT does not allow parallel solution of a single problem with one orientation only. Possible solutions for these limitations and other recommendations are given in the next chapter.

CHAPTER 7

RECOMMENDATIONS

7.1 Solutions to the Limitations

The possible solutions for the limitations explained before are:

1. To enlarge the size of all dipoles.
2. To make some approximations to introduce the substrate.
3. To write a supplementary code to parallelize the DDSCAT code that will enable the solution of this type of problems.

The first suggestion is not a favorable solution for this problem, since with increasing dipole size the target geometry deviates from its real shape as the number of dipoles to model the geometry gets smaller. On the other hand, making dipoles with differing sizes in a single problem is not possible with current version of DDSCAT either. Therefore modeling surface with larger sized dipoles and the particles with smaller sized dipoles would not be possible.

In order to model the surface it is required to make some approximations or apply theories like image theory. However this requires in depth study of physics behind the particle surface interactions and is therefore not possible within the context of this study. Moreover it would be possible to model surface plasmon waves if the electromagnetic waves with changing intensity can be modeled in DDSCAT which is not possible with the current code.

Similarly developing a new code to enable parallel computations when the RAM is not enough is another challenge because it requires a very strong background on the codes of

DDSCAT7.0. Therefore, it is better to leave the development of this code to the authors of DDSCAT7.0.

It is essential to highlight one significant advantage of another DDA code, ADDA (Amsterdam DDA). Unlike DDSCAT, Amsterdam DDA allows the parallelization of a single DDA execution on a multiprocessor system, using MPI (message passing interface) [71]. Thus the size of the scatterer or the number of dipoles is no longer a limitation for light scattering calculations. On the other hand, ADDA manual states that DDA cannot be applied to particles that are not isolated from other scatterers. Hence, with ADDA it is not possible to investigate the dependent scattering effects. While the prescribed geometries of DDSCAT include multiple geometries in a single problem such as MLTBLOCKS(multiple blocks) or SPHERES_N(multiple spheres) ADDA's prescribed geometries do not involve targets composed of multiple particles.

Therefore it is not possible to use ADDA for the studies in the scope of this thesis. Hence it is suggested that either ADDA should develop its target options that accounts for the dependent scattering of the particles or DDSCAT should be improved with the inclusion of the codes that will enable the parallel computation of a single problem.

7.2 Possible Improvements for the Numerical Procedure

Being a numerical study, the present work involves some errors that might arise due to:

1. the numerical errors in the solution of the problem with DDSCAT.
2. the truncation errors due to DDFIELD in the calculation of electrical and magnetic fields that are used for the calculation of the Poynting vector.
3. the numerical errors arising in the numerical integration of the Poynting vector on an imaginary surface.

The numerical errors within DDSCAT can be reduced by choosing a small dipole size and high tolerance values. Moreover, particles with low dielectric constants should be investigated.

To eliminate the errors coming from the Integrated Poynting Vector Approach the surface grids must be kept small. By this way the summation of the Poynting vector over the control surface will be closer to the integral of the Poynting vector over that surface.

7.3 Future Prospects

With the development of the computational power of computers and the parallelized numerical codes it will be possible to model computationally demanding light scattering problems that can be faced in reality. Given that, in the future substrate and/or tip effects would be modeled rigorously.

DDSCAT does not have a user friendly interface. This might be improved and some other post-processing tools might be included. By this way the visualization of the generated target, the distribution of the electrical field inside and outside the particles and the interaction of particles become clearer.

Several groups tried to use the absorption of noble metal particles for such heating applications as heating of surrounding matrix or heating and fusing directly the metal particles.

It is important to note that at nanoscale the thermodynamic properties of the particles change as well, therefore, the correlation between the absorption and heating of the particles must be found. Only by this way the dependent absorption of the noble metal particles can be used for real heating applications.

7.4 Final Remarks

In this study dependent scattering solutions are performed with DDSCAT7.0. A new technique is introduced for the analysis of the absorption efficiency of the individual particles. Results show that the near field effects can easily be recognized from the absorption spectra of the whole system calculated by DDSCAT and of the individual particles obtained by the Integrated Poynting Vector Approach.

The **Integrated Poynting Vector Approach** can be improved by modifying the DDFIELD code of DDSCAT7.0. This may increase computational speed and sampling rate as well as

accuracy. Besides, to account for the surface effects DDSCAT should be modified and so that parallel computations will be possible as in ADDA.

Finally, dependent scattering effects with resonance have been studied, which is beyond what Ivezic and Menüç has accomplished [32]. Findings of this thesis on dependent scattering and absorption can be used for developing new technological applications ranging from nanomanufacturing to plasmonic solar cells and even to plasmonic cancer treatment applications.

Bibliography

- [1] http://www.ansci.wisc.edu/facstaff/Faculty/pages/albrecht/albrecht_web/Programs/microscopy/colloid.html(last visited in June 2009).
- [2] Alvarez, M. M., J. T. Khoury, T. G. Schaaff, M. N. Shafigullin, I. Vezmar, and R. L. Whetten (1997). Optical absorption spectra of nanocrystal gold molecules. *J. Chem. Phys.* *101*, 3706–3712.
- [3] Aslan, M. M., M. P. Menguc, and G. Videen (2005). Characterization of metallic nanoparticles via surface wave scattering: B. physical concept and numerical experiments. *JQSRT* *93*, 207–217.
- [4] Ayranci, I., N. Selcuk, and R. Vaillon (2007). Performance of discrete dipole approximation for prediction of amplitude and phase of electromagnetic scattering by particles. *JQSRT* *103*, 83–101.
- [5] Bohren, C. F. and D. R. Huffman (1983). *Absorption and Scattering of Light by Small Particles*. John Wiley & Sons.
- [6] Bondeson, A., T. Rylander, and P. Ingelstrom (2005). *Computational Electromagnetics*. Springer.
- [7] Brongersma, M. L. and P. G. Kik (2007). *Surface Plasmon Nanophotonics*. Springer.
- [8] Burda, C., X. Chen, R. Narayanan, and M. A. El-Sayed (2005). Chemistry and properties of nanocrystals of different shapes. *Chem. Rev.* *105*, 1025–1102.
- [9] Busnaina, A. (2006). *Nanomanufacturing Handbook*. CRC Press.
- [10] Canifield, L. R., G. Hass, and W. R. Hunter (1964). *J. Phys. (Paris)* *25*, 124.
- [11] Catchpole, K. R., S. Pillai, and K. L. Lin (2003). Novel applications in photovoltaics. *3rd world conference on photovoltaic energy conversion poster*, SIP–A7–09.

- [12] Charnigo, R., M. Francoeur, M. P. Menguc, A. Brock, M. Leichter, and C. Srinivasan (2007). Derivatives of scattering profiles: tools for nanoparticle characterization. *J. Opt. Soc. Am. A* 24, No. 9, 2578–2589.
- [13] Cortie, M. B. (2004). The weird world of nanoscale gold. *Gold Bulletin* 37, 12–19.
- [14] Doicu, A., T. Wriedt, and Y. A. Eremin (2006). *Light Scattering by Systems of Particles*. Springer.
- [15] Draine, B. T. (1988). The discrete dipole approximation and its application to interstellar graphite grains. *Ap. J.* 333, 848–872.
- [16] Draine, B. T. and P. J. Flatau (1994). Discrete dipole approximation for scattering calculations. *J Opt Soc Am A* 11-4, 1491–99.
- [17] Draine, B. T. and P. J. Flatau (2008a). The discrete dipole approximation for periodic targets: I. theory and tests. *J. Opt. Soc. Am. A* 25, 2693–2703.
- [18] Draine, B. T. and P. J. Flatau (2008b). *User Guide for the Discrete Dipole Approximation Code DDSCAT7.0*. <http://arxiv.org/abs/0809.0337v4> (last visited in June 2009).
- [19] Draine, B. T. and J. Goodman (1993). Beyond clausius-mossotti - wave propagation on a polarizable point lattice and the discrete dipole approximation. *Astrophysical Journal, Part 1* 405, 685–697.
- [20] Ekici, O., R. K. Harrison, N. J. Durr, D. S. Eversole, M. Lee, and A. B. Yakar (2008). Thermal analysis of gold nanorods heated with femtosecond laser pulses. *Journal of Physics D: Applied Physics* 41, 1–11.
- [21] El-Sayed, M. A. (2001). Some interesting properties of metals confined in time and nanometer space of different shapes. *Accounts of Chemical Research* 34, 257–264.
- [22] Feynman, R. P. (1959). Plenty of room at the bottom. <http://www.its.caltech.edu/~feynman/plenty.html> (last visited in June 2009).
- [23] Flatau, P. J., K. A. Fuller, and D. W. Mackowski (1993). Scattering by two spheres in contact: comparisons between discrete-dipole approximation and modal analysis. *Applied Optics* 32(18), 3302–3305.

- [24] Gimzewski, J. K. and C. Joachim (1999). Nanoscale science of single molecules using local probes. *Science* 283, 1683.
- [25] Hagemann, H.-J., W. Gudat, and C. Kunz (1975). Optical constants from the far infrared to the x-ray region. *J. Opt. Soc. Am.* 65, 742–744.
- [26] Hawes, E. (2007). *Selective Assembly of Nanoparticles by AFM-Based Nanomanufacturing*. Ph. D. thesis, University of Kentucky.
- [27] Hawes, E. (2008). Spatially selective melting and evaporation of nanosized gold particles. *Optics Letters* 33, 1383.
- [28] Hawes, E., J. Hastings, C. Crofcheck, and M. P. Menguc (2007). Spectrally selective heating of nanosized particles by surface plasmon resonance. *JQSRT* 104, 199–207.
- [29] Hoppe, H., N. Arnold, N. Sariciftci, and D. Meissner (2003). Modeling the optical absorption within conjugated polymer/fullerene-based bulk-heterojunction organic solar cells. *Solar Energy Materials and Solar Cells* 80, 105.
- [30] Huang, X., I. H. El-Sayed, W. Qian, and M. A. El-Sayed (2006). Cancer cell imaging and photothermal therapy in the near-infrared region by using gold nanorods. *Journal of the American Chemical Society* 128 (6), 2115–2120.
- [31] Irani, G. B., T. Huen, and F. Wooten (1971). Optical constants of silver and gold in the visible and vacuum ultraviolet. *J. Opt. Soc. Am. A* 61, 128–129.
- [32] Ivezic, Z. and M. P. Menguc (1996). An investigation of dependent/independent scattering regimes using a discrete dipole approximation. *International Journal of Heat Mass Transfer* Vol. 39, No. 4, 811–822.
- [33] Ivezic, Z., M. P. Menguc, and T. G. Knauer (1997). A procedure to determine the onset of soot agglomeration from multi-wavelength experiments. *JQSRT* 57(6), 859–865.
- [34] Kawata, S. (2002). *Nano-Optics*. Springer.
- [35] Kelly, K. L., E. Coronado, L. L. Zhao, and G. C. Schatz (2003). The optical properties of metal nanoparticles: The influence of size, shape, and dielectric environment. *Journal Physical Chemistry B* 107, 668–677.

- [36] Khlebtsov, B. N., V. A. Khanadeyev, and N. G. Khlebtsov (2008). Observation of extra-high depolarized light scattering spectra from gold nanorods. *Journal Physical Chemistry C 112*, 12760–12768.
- [37] Khlebtsov, N. G. (2008a). Determination of size and concentration of gold nanoparticles from extinction spectra. *Anal. Chem.* 80, 6620–6625.
- [38] Khlebtsov, N. G. (2008b). Optics and biophotonics of nanoparticles with a plasmon resonance. *Quantum Electronics 38(6)*, 504–529.
- [39] Kozan, M. (2007). *Characterization Of Colloidal Nanoparticle Aggregates Using Light Scattering Techniques*. Ph. D. thesis, University of Kentucky.
- [40] Kozan, M., J. Thangala, R. Bogale, M. P. Menguc, and M. K. Sunkara (2008). In-situ characterization of dispersion stability of WO_3 nanoparticles and nanowires. *Journal of Nanoparticle Research 10 (4)*, 599–612.
- [41] Landau, L. D., E. M. Lifshitz, and L. P. Pitaevskii (1984). *Electrodynamics of Continuous Media*. Pergamon Press.
- [42] Laven, P. (2008). Mieplot, www.philiplaven.com/mieplot.htm (last visited in June 2009).
- [43] Link, S. and M. A. El-Sayed (2003). Optical properties and ultrafast dynamics of metallic nanocrystals. *Annu. Rev. Phys. Chem.* 54, 331–66.
- [44] Marrian, C. R. K. and D. M. Tennant (2003). Nanofabrication. *Journal of Vacuum Science & Technology 21*, 207–215.
- [45] Merchiers, O. (2007). *A study of light scattering by aggregates*. Ph. D. thesis, Facultad de Ciencias Departamento de Física Aplicada.
- [46] Mishchenko, M. I., L. D. Travis, and A. A. Lacis (2002). *Scattering, Absorption, and Emission of Light by Small Particles*. Cambridge University Press.
- [47] Noguez, C. (2007). Surface plasmons on metal nanoparticles: The influence of shape and physical environment. *Journal Physical Chemistry C 111*, 3806–3819.
- [48] Novotny, L. and B. Hecht (2006). *Principles of Nano-Optics*. Cambridge University Press.
- [49] Ohtsu, M. and K. Kobayashi (2004). *Optical Near Fields*. Springer.

- [50] Otter, M. (1961). Optische konstanten massiver metalle. *Journal Zeitschrift für Physik A Hadrons and Nuclei* 161, 163–178.
- [51] P. B. Johnson, R. W. C. (1972). Optical constants of noble metals. *Physical Review B* 6, 4370–4379.
- [52] Palik, E. D. and G. Ghosh (1998). *Handbook of optical constants of solids*. Academic Press.
- [53] Penttillä, A., E. Zubko, K. Lumme, K. Muinonen, M. A. Yurkin, B. Draine, J. Rahola, A. G. Hoekstra, and Y. Shkuratov (2007). Comparison between discrete dipole implementations and exact techniques. *JQSRT* 106, 417–436.
- [54] Perez, J., I. P. Santos, L. M. Liz-Marzan, P. Mulvaney, and J. Perez (2005). Gold nanorods: Synthesis, characterization and applications. *Coordination Chemistry Reviews* 249, 1870–1901.
- [55] Prescott, S. W. and P. Mulvaney (2006). Gold nanorod extinction spectra. *Journal of Applied Physics* 99, 123504.
- [56] Purcell, E. M. and C. R. Pennypacker (1973). Scattering and absorption of light by nonspherical dielectric grains. *The Astrophysical Journal* 186, 705–714.
- [57] Roco, M. (2004). Nanoscale science and engineering: Unifying and transforming tools. *AIChE Journal* 50, 890–897.
- [58] Schulz, L. G. and F. Tangherlini (1954). Optical constants of silver, gold, copper, and aluminum. *J. Opt. Soc. Am.* 44, 362–367.
- [59] Sherry, L. J. (2007). *Studies of Single Nanoparticle Systems by Localized Surface Plasmon Resonance Spectroscopy, Atomic Force Microscopy, Transmission Electron Microscopy, and Combinations Thereof*. Ph. D. thesis, Northwestern University.
- [60] Sorensen, C. M. (2001). Light scattering by fractal aggregates. *Aerosol Science and Technology* 35, 648–687.
- [61] Sosa, I. O., C. Noguez, , and R. G. Barrera (2003). Optical properties of metal nanoparticles with arbitrary shapes. *Journal Physical Chemistry B* 107, 6269–6275.

- [62] Taubenblatt, M. A. and T. K. Tran (1993). Calculation of light scattering from particles and structures on a surface by the coupled dipole method. *J. Opt. Soc. Am. A* 10, 912–919.
- [63] Timp, G. (1998). *Nanotechnology*. Springer.
- [64] Tsang, L., J. A. Kong, K. H. Ding, and C. O. Ao (2001). *Scattering of Electromagnetic Waves: Numerical Simulations*. John Wiley & Sons.
- [65] Ulaby, F. T. (2006). *Fundamentals of Applied Electromagnetics*. Prentice Hall.
- [66] Venkata, P. G., M. M. Aslan, M. P. Menguc, and G. Videen (2007). Surface plasmon scattering by gold nanoparticles and two-dimensional agglomerates. *Journal of Heat Transfer* 129, 60–70.
- [67] Waterman, P. C. (1965). Matrix formulation of electromagnetic scattering. *Proc IEEE* 53, 805–812.
- [68] Weaver, J., C. Krafka, D. Lynch, and E. Koch (1981). Optical properties of metals. *Applied Optics* 20, 1124–1125.
- [69] Wong, B. T. and M. P. Menguc (2008). *Thermal Transport for Applications in Micro Nanomachining*. Springer.
- [70] Yang, W.-H., G. C. Schatz, and R. P. V. Duyne (1995). Discrete dipole approximation for calculating extinction and raman intensities for small particles with arbitrary shapes. *J. Chem. Phys.* 103, 869–875.
- [71] Yurkin, M. A. and A. G. Hoekstra (2008, April). *User Manual for the Discrete Dipole Approximation Code- Amsterdam DDA (version 0.78.2)*. <http://www.science.uva.nl/research/scs/Software/adda/index.html> (last visited in June 2009).
- [72] Yurkin, M. A., A. G. Hoekstra, and V. P. Maltsev (2007). The discrete dipole approximation for simulation of light scattering by particles much larger than the wavelength. *JQSRT* 106, 5465–57.

APPENDIX A

DIELECTRIC CONSTANTS

A.1 Gold

Table A.1: Dielectric Function of gold (Au) [51]

eV	$\lambda(\text{nm})$	n	k
0.64	1937.500000	0.92	13.78
0.77	1610.389610	0.56	11.21
0.89	1393.258427	0.43	9.519
1.02	1215.686275	0.35	8.145
1.14	1087.719298	0.27	7.150
1.26	984.1269841	0.22	6.350
1.39	892.0863309	0.17	5.663
1.51	821.1920530	0.16	5.083
1.64	756.0975610	0.14	4.542
1.76	704.5454545	0.13	4.103
1.88	659.5744681	0.14	3.697
2.01	616.9154229	0.21	3.272
2.13	582.1596244	0.29	2.863
2.26	548.6725664	0.43	2.455
2.38	521.0084034	0.62	2.081
2.50	496.0000000	1.04	1.833
2.63	471.4828897	1.31	1.849

Continued on Next Page...

eV	$\lambda(\text{nm})$	n	k
2.75	450.9090909	1.38	1.914
2.88	430.5555556	1.45	1.948
3.00	413.3333333	1.46	1.958
3.12	397.4358974	1.47	1.952
3.25	381.5384615	1.46	1.933
3.37	367.9525223	1.48	1.895
3.50	354.2857143	1.50	1.866
3.62	342.5414365	1.48	1.871
3.74	331.5508021	1.48	1.883
3.87	320.4134367	1.54	1.898
3.99	310.7769424	1.53	1.893
4.12	300.9708738	1.53	1.889
4.24	292.4528302	1.49	1.878
4.36	284.4036697	1.47	1.869
4.49	276.1692650	1.43	1.847
4.61	268.9804772	1.38	1.803
4.74	261.6033755	1.35	1.749
4.86	255.1440329	1.33	1.688
4.98	248.9959839	1.33	1.631
5.11	242.6614481	1.32	1.577
5.23	237.0936902	1.32	1.536
5.36	231.3432836	1.30	1.497
5.48	226.2773723	1.31	1.46
5.60	221.4285714	1.30	1.427
5.73	216.4048866	1.30	1.387
5.85	211.9658120	1.30	1.35
5.98	207.3578595	1.30	1.304
6.10	203.2786885	1.33	1.277
6.22	199.3569132	1.33	1.251

Continued on Next Page...

eV	$\lambda(\text{nm})$	n	k
6.35	195.2755906	1.34	1.226
6.47	191.6537867	1.32	1.203
6.60	187.8787879	1.28	1.188

A.2 Silicon

Table A.2: Dielectric Function of silicon (Si) [52]

$\lambda(\text{nm})$	n	k
200	1.00220000	2.90510000
210	1.13658520	3.06686336
220	1.29462404	3.27578987
230	1.56870000	3.45760000
240	1.69724999	3.46604710
250	1.68358679	3.70848976
260	1.80230000	4.16710000
270	2.17881451	4.77550909
280	3.10743504	5.40393856
290	4.54220000	5.15500000
300	5.15309329	4.14556283
310	5.14768478	3.55487125
320	5.16520000	3.26280000
330	5.23850895	3.07037485
340	5.35736760	2.93714665
350	5.56350000	2.88330000
360	6.08408829	2.83028870
370	6.90593920	2.04384552
380	6.59140000	0.84942000
390	5.99758223	0.43107671
400	5.59742773	0.28452651
410	5.32180000	0.20389000
420	5.10748664	0.14879314
430	4.93254987	0.11283128
440	4.78740000	0.09035500
450	4.66656982	0.07659401

Continued on Next Page...

$\lambda(\text{nm})$	n	k
460	4.56526405	0.06790192
470	4.47880000	0.06191400
480	4.40474546	0.05741546
490	4.34008131	0.05365979
500	4.28310000	0.05033200
510	4.23256810	0.04727595
520	4.18721790	0.04441066
530	4.14620000	0.04170700
540	4.10892069	0.03915245
550	4.07501014	0.03673648
560	4.04380000	0.03444800
570	4.01507002	0.03228099
580	3.98847755	0.03023947
590	3.96380000	0.02830800
600	3.94098385	0.02648798
610	3.91965104	0.02476998
620	3.89970000	0.02314700
630	3.88097488	0.02162594
640	3.86338508	0.02018655
650	3.84690000	0.01883400
660	3.83139150	0.01755538
670	3.81662332	0.01635826
680	3.80280000	0.01522700
690	3.78961930	0.01416174
700	3.77718893	0.01316626
710	3.76540000	0.01222700
720	3.75419268	0.01134115
730	3.74352947	0.01051156
740	3.73340000	0.00973310

Continued on Next Page...

$\lambda(\text{nm})$	n	k
750	3.72376794	0.00900231
760	3.71449294	0.00831610
770	3.70570000	0.00767250
780	3.69731092	0.00706891
790	3.68927367	0.00650331
800	3.68150000	0.00597350
810	3.67416130	0.00547825
820	3.66708828	0.00501461
830	3.66030000	0.00458170
840	3.65375481	0.00417660
850	3.64750527	0.00379977
860	3.64140000	0.00344930
870	3.63573296	0.00312536
880	3.63013824	0.00282412
890	3.62470000	0.00254320
900	3.61948166	0.00228096

APPENDIX B

PARAMETER AND OUTPUT FILES OF DDSCAT7.0

B.1 Sample Parameter File (ddscat.par)

```
===== Parameter file for v7.0.7 =====
**** Preliminaries ****
NOTORQ = CMTORQ*6 (NOTORQ, DOTORQ) -- either do or skip torque calculations
PBCGS2 = CMDSOL*6 (PBCGS2, PBCGST, PETRKP) -- select solution method
GPFAFT = CMDFFT*6 (GPFAFT, FFTMKL)
GKDLDR = CALPHA*6 (GKDLDR, LATDR)
NOTBIN = CBINFLAG (NOTBIN, ORIBIN, ALLBIN)
**** Initial Memory Allocation ****
100 100 100 = dimensioning allowance for target generation
**** Target Geometry and Composition ****
RCTGLPRSM = CSHAPE*9 shape directive
32 24 16 = shape parameters 1 - 3
1 = NCOMP = number of dielectric materials
diel.tab = file with refractive index 1
**** Error Tolerance ****
1.00e-5 = TOL = MAX ALLOWED (NORM OF |G>=AC|E>-ACA|X>)/(NORM OF AC|E>)
**** Interaction cutoff parameter for PBC calculations ****
5.00e-3 = GAMMA (1e-2 is normal, 3e-3 for greater accuracy)
**** Angular resolution for calculation of <cos>, etc. ****
0.5 = ETASCA (number of angles is proportional to [(3+x)/ETASCA]2 )
**** Wavelengths (micron) ****
6.283185 6.283185 1 LIN = wavelengths (first,last,how many,how=LIN,INV,LOG)
**** Effective Radii (micron) ****
2 2 1 LIN = aeff (first,last,how many,how=LIN,INV,LOG)
**** Define Incident Polarizations ****
(0,0) (1.,0.) (0.,0.) = Polarization state e01 (k along x axis)
2 = IORTH (=1 to do only pol. state e01; =2 to also do orth. pol. state)
```

```

**** Specify which output files to write ****
1 = IWRKSC (=0 to suppress, =1 to write ".sca" file for each target orient.
1 = IWRPOL (=0 to suppress, =1 to write ".pol" file for each (BETA,THETA)
**** Prescribe Target Rotations ****
0. 0. 1 = BETAMI, BETAMX, NBETA (beta=rotation around a1)
0. 90. 3 = THETMI, THETMX, NTHETA (theta=angle between a1 and k)
0. 0. 1 = PHIMIN, PHIMAX, NPHI (phi=rotation angle of a1 around k)
**** Specify first IWAV, IRAD, IORI (normally 0 0 0) ****
0 0 0 = first IWAV, first IRAD, first IORI (0 0 0 to begin fresh)
**** Select Elements of S_ij Matrix to Print ****
6 = NSMELTS = number of elements of S_ij to print (not more than 9)
11 12 21 22 31 41 = indices ij of elements to print
**** Specify Scattered Directions ****
LFRAME = CMDFRM (LFRAME, TFRAME for Lab Frame or Target Frame)
2 = NPLANES = number of scattering planes
0. 0. 180. 10 = phi, thetan_min, thetan_max, dtheta (in deg) for plane 1
90. 0. 180. 10 = phi, thetan_min, thetan_max, dtheta (in deg) for plane 2

```

B.2 Sample Output Files

B.2.1 wxxxryy.avg Files

This file contains the results for the first wavelength (w000) and first target radius(r00) averaged over orientations (.avg). The w000r00ori.avg file generated by the sample calculation should look like the following:

```

DDSCAT --- DDSCAT 7.0.7 [08.08.29]
TARGET --- Rectangular prism; NX,NY,NZ= 32 24 16
GPFAFT --- method of solution
GKDLDR --- prescription for polarizabilities
RCTGLPRSM --- shape
12288 = NAT0 = number of dipoles
0.06985579 = d/aeff for this target [d=dipole spacing]
0.139712 = d (physical units)
AEFF= 2.000000 = effective radius (physical units)
WAVE= 6.283185 = wavelength (physical units)
K*AEFF= 2.000000 = 2*pi*aeff/lambda
n= ( 1.3300 , 0.0100), eps.= ( 1.7688 , 0.0266) |m|kd= 0.1858 for subs. 1
TOL= 1.000E-05 = error tolerance for CCG method
( 1.00000 0.00000 0.00000) = target axis A1 in Target Frame

```

```

( 0.00000 1.00000 0.00000) = target axis A2 in Target Frame
NAVG= 603 = (theta,phi) values used in comp. of Qsca,g
( 0.13971 0.00000 0.00000) = k vector (latt. units) in Lab Frame
( 0.00000, 0.00000)( 1.00000, 0.00000)( 0.00000, 0.00000)=inc.pol.vec. 1 in LF
( 0.00000, 0.00000)( 0.00000, 0.00000)( 1.00000, 0.00000)=inc.pol.vec. 2 in LF
0.000 0.000 = beta_min, beta_max ; NBETA = 1
0.000 90.000 = theta_min, theta_max; NTHETA= 3
0.000 0.000 = phi_min, phi_max ; NPHI = 1
0.5000 = ETASCA = param. controlling # of scatt. dirs used to calculate <cos> etc.
Results averaged over 3 target orientations
and 2 incident polarizations
Qext Qabs Qsca g(1)=<cos> <cos2> Qbk Qpha
JO=1: 8.6320E-01 8.1923E-02 7.8128E-01 6.5932E-01 5.5093E-01 8.6216E-03 9.5911E-01
JO=2: 5.9773E-01 6.5842E-02 5.3189E-01 7.0837E-01 5.7263E-01 6.6332E-03 8.9157E-01
mean: 7.3047E-01 7.3882E-02 6.5659E-01 6.7919E-01 5.7263E-01 7.6274E-03 9.2534E-01
Qpol= 2.6547E-01 dQpha= 6.7534E-02
Qsca*g(1) Qsca*g(2) Qsca*g(3) iter mxiter Nsca
JO=1: 5.1512E-01 2.0999E-02 2.0275E-08 3 13 603
JO=2: 3.7677E-01 3.3543E-02 -4.5799E-09 3 13 603
mean: 4.4595E-01 2.7271E-02 7.8476E-09
Mueller matrix elements for selected scattering directions in Lab Frame
theta phi Pol. S_11 S_12 S_21 S_22 S_31 S_41
0.00 0.00 0.11122 3.9825E+00 4.4295E-01 4.430E-01 3.982E+00 -9.951E-09 -1.167E-08
10.00 0.00 0.09797 3.7743E+00 3.6976E-01 3.698E-01 3.774E+00 1.511E-09 -8.158E-09
20.00 0.00 0.06514 3.2121E+00 2.0924E-01 2.092E-01 3.212E+00 8.423E-09 -9.677E-09
30.00 0.00 0.01115 2.4761E+00 2.7618E-02 2.762E-02 2.476E+00 6.078E-08 1.683E-08
40.00 0.00 0.06519 1.7463E+00 -1.1383E-01 -1.138E-01 1.746E+00 -1.787E-08 2.854E-08
50.00 0.00 0.16289 1.1386E+00 -1.8546E-01 -1.855E-01 1.139E+00 -9.912E-09 -4.191E-08
60.00 0.00 0.27512 6.9235E-01 -1.9048E-01 -1.905E-01 6.923E-01 -1.481E-08 -1.639E-08
70.00 0.00 0.38377 3.9361E-01 -1.5106E-01 -1.511E-01 3.936E-01 2.248E-08 -6.877E-09
80.00 0.00 0.45466 2.0690E-01 -9.4071E-02 -9.407E-02 2.069E-01 1.167E-09 -2.473E-08
90.00 0.00 0.43502 9.7450E-02 -4.2393E-02 -4.239E-02 9.745E-02 -3.071E-09 4.950E-09
100.00 0.00 0.24195 4.0410E-02 -9.7771E-03 -9.777E-03 4.041E-02 -5.077E-09 -2.816E-08
110.00 0.00 0.09530 2.0545E-02 1.9580E-03 1.958E-03 2.054E-02 1.702E-09 -1.171E-08
120.00 0.00 0.03721 2.7014E-02 1.0051E-03 1.005E-03 2.701E-02 1.912E-10 7.689E-10
130.00 0.00 0.03732 4.8444E-02 -1.8079E-03 -1.808E-03 4.844E-02 -1.631E-09 -3.689E-09
140.00 0.00 0.00713 7.2647E-02 -5.1804E-04 -5.180E-04 7.265E-02 2.516E-09 1.104E-09
150.00 0.00 0.04843 9.0620E-02 4.3883E-03 4.388E-03 9.062E-02 -8.039E-10 2.467E-09
160.00 0.00 0.09683 9.9496E-02 9.6343E-03 9.634E-03 9.950E-02 4.170E-09 7.095E-10
170.00 0.00 0.12598 1.0070E-01 1.2687E-02 1.269E-02 1.007E-01 2.833E-09 -1.472E-09

```

```

180.00 0.00 0.13035 9.5849E-02 1.2494E-02 1.249E-02 9.585E-02 -2.431E-10 9.756E-11
0.00 90.00 0.11122 3.9825E+00 -4.4295E-01 -4.430E-01 3.982E+00 -3.742E-08 -1.576E-08
10.00 90.00 0.12297 3.8723E+00 -4.7608E-01 -4.760E-01 3.872E+00 -1.264E-02 -1.104E-02
20.00 90.00 0.15873 3.5536E+00 -5.6379E-01 -5.636E-01 3.553E+00 -2.351E-02 -2.020E-02
30.00 90.00 0.21988 3.0638E+00 -6.7334E-01 -6.730E-01 3.063E+00 -3.087E-02 -2.582E-02
40.00 90.00 0.30800 2.4662E+00 -7.5935E-01 -7.589E-01 2.466E+00 -3.336E-02 -2.685E-02
50.00 90.00 0.42330 1.8418E+00 -7.7949E-01 -7.790E-01 1.841E+00 -3.057E-02 -2.326E-02
60.00 90.00 0.56157 1.2701E+00 -7.1315E-01 -7.128E-01 1.270E+00 -2.348E-02 -1.624E-02
70.00 90.00 0.71013 8.0650E-01 -5.7261E-01 -5.725E-01 8.062E-01 -1.433E-02 -7.917E-03
80.00 90.00 0.84528 4.7037E-01 -3.9748E-01 -3.975E-01 4.702E-01 -5.730E-03 -5.546E-04
90.00 90.00 0.93786 2.5001E-01 -2.3444E-01 -2.345E-01 2.498E-01 3.705E-04 4.290E-03
100.00 90.00 0.96898 1.1900E-01 -1.1547E-01 -1.153E-01 1.186E-01 3.258E-03 6.211E-03
110.00 90.00 0.93364 5.0906E-02 -4.7946E-02 -4.740E-02 5.024E-02 3.410E-03 5.818E-03
120.00 90.00 0.76404 2.5253E-02 -1.9997E-02 -1.919E-02 2.437E-02 1.966E-03 4.206E-03
130.00 90.00 0.47038 2.6571E-02 -1.3386E-02 -1.250E-02 2.563E-02 1.256E-04 2.390E-03
140.00 90.00 0.31141 4.2301E-02 -1.3889E-02 -1.311E-02 4.150E-02 -1.273E-03 9.800E-04
150.00 90.00 0.22711 6.2453E-02 -1.4597E-02 -1.406E-02 6.190E-02 -1.874E-03 1.589E-04
160.00 90.00 0.17277 8.0205E-02 -1.4023E-02 -1.375E-02 7.993E-02 -1.704E-03 -1.593E-04
170.00 90.00 0.14092 9.1846E-02 -1.2978E-02 -1.290E-02 9.177E-02 -9.878E-04 -1.543E-04
180.00 90.00 0.13035 9.5849E-02 -1.2494E-02 -1.249E-02 9.585E-02 1.420E-09 4.482E-10

```

B.2.2 wxxxryyykzzz.sca Files

The w000r000k000.sca file contains the results for the first wavelength (w000), first target radius (r00), and first orientation (k000). The w000r000k000.sca file created by the sample calculation should look like the following:

```

DDSCAT --- DDSCAT 7.0.7 [08.08.29]
TARGET --- Rectangular prism; NX,NY,NZ= 32 24 16
GPFAFT --- method of solution
GKDLDR --- prescription for polarizabilities
RCTGLPRSM --- shape
12288 = NAT0 = number of dipoles
0.06985579 = d/aeff for this target [d=dipole spacing]
0.139712 = d (physical units)
----- physical extent of target volume in Target Frame -----
-4.470771 0.000000 = xmin,xmax (physical units)
-1.676539 1.676539 = ymin,ymax (physical units)
-1.117693 1.117693 = zmin,zmax (physical units)
AEFF= 2.000000 = effective radius (physical units)
WAVE= 6.283185 = wavelength (physical units)

```

```

K*AEFF= 2.000000 = 2*pi*aeff/lambda
n= ( 1.3300 , 0.0100), eps.= ( 1.7688 , 0.0266) |m|kd= 0.1858 for subs. 1
TOL= 1.000E-05 = error tolerance for CCG method
( 1.00000 0.00000 0.00000) = target axis A1 in Target Frame
( 0.00000 1.00000 0.00000) = target axis A2 in Target Frame
NAVG= 603 = (theta,phi) values used in comp. of Qsca,g
( 0.13971 0.00000 0.00000) = k vector (latt. units) in TF
( 0.00000, 0.00000)( 1.00000, 0.00000)( 0.00000, 0.00000)=inc.pol.vec. 1 in TF
( 0.00000, 0.00000)( 0.00000, 0.00000)( 1.00000, 0.00000)=inc.pol.vec. 2 in TF
( 1.00000 0.00000 0.00000) = target axis A1 in Lab Frame
( 0.00000 1.00000 0.00000) = target axis A2 in Lab Frame
( 0.13971 0.00000 0.00000) = k vector (latt. units) in Lab Frame
( 0.00000, 0.00000)( 1.00000, 0.00000)( 0.00000, 0.00000)=inc.pol.vec. 1 in LF
( 0.00000, 0.00000)( 0.00000, 0.00000)( 1.00000, 0.00000)=inc.pol.vec. 2 in LF
BETA = 0.000 = rotation of target around A1
THETA= 0.000 = angle between A1 and k
PHI = 0.000 = rotation of A1 around k
0.5000 = ETASCA = param. controlling # of scatt. dirs used to calculate <cos> etc.
Qext Qabs Qsca g(1)=<cos> <cos2> Qbk Qpha
JO=1: 9.0997E-01 8.6105E-02 8.2387E-01 6.4090E-01 5.8427E-01 2.5108E-02 9.7717E-01
JO=2: 6.9891E-01 7.0519E-02 6.2839E-01 6.5894E-01 6.0509E-01 1.9097E-02 9.1277E-01
mean: 8.0444E-01 7.8312E-02 7.2613E-01 6.4871E-01 5.9328E-01 2.2103E-02 9.4497E-01
Qpol= 2.1106E-01 dQpha= 6.4397E-02
Qsca*g(1) Qsca*g(2) Qsca*g(3) iter mxiter Nsca
JO=1: 5.2802E-01 -1.2657E-08 -1.6907E-08 3 13 603
JO=2: 4.1407E-01 -4.0495E-08 -1.0475E-09 3 13 603
mean: 4.7105E-01 -2.6576E-08 -8.9774E-09
Mueller matrix elements for selected scattering directions in Lab Frame
theta phi Pol. S_11 S_12 S_21 S_22 S_31 S_41
0.00 0.00 0.09758 4.2343E+00 4.1320E-01 4.132E-01 4.234E+00 3.953E-10 1.753E-10
10.00 0.00 0.08802 4.0521E+00 3.5667E-01 3.567E-01 4.052E+00 1.105E-08 -2.338E-08
20.00 0.00 0.05875 3.5445E+00 2.0822E-01 2.082E-01 3.544E+00 -1.771E-08 -3.568E-08
30.00 0.00 0.00810 2.8187E+00 2.2829E-02 2.283E-02 2.819E+00 3.923E-08 -1.997E-08
40.00 0.00 0.06619 2.0233E+00 -1.3391E-01 -1.339E-01 2.023E+00 -6.927E-08 1.304E-07
50.00 0.00 0.16569 1.3011E+00 -2.1558E-01 -2.156E-01 1.301E+00 -1.984E-08 -2.180E-08
60.00 0.00 0.28746 7.4420E-01 -2.1393E-01 -2.139E-01 7.442E-01 -5.892E-08 -1.007E-07
70.00 0.00 0.41470 3.7493E-01 -1.5549E-01 -1.555E-01 3.749E-01 6.340E-08 4.262E-08
80.00 0.00 0.49576 1.6262E-01 -8.0621E-02 -8.062E-02 1.626E-01 6.664E-09 -3.151E-08
90.00 0.00 0.38933 5.6897E-02 -2.2152E-02 -2.215E-02 5.690E-02 -1.247E-08 -1.200E-08
100.00 0.00 0.34694 1.4850E-02 5.1520E-03 5.152E-03 1.485E-02 -3.687E-09 -8.223E-10

```

```

110.00 0.00 0.39736 1.1368E-02 4.5172E-03 4.517E-03 1.137E-02 6.363E-09 -1.163E-09
120.00 0.00 0.25849 3.5576E-02 -9.1961E-03 -9.196E-03 3.558E-02 5.643E-09 1.226E-09
130.00 0.00 0.23722 8.1132E-02 -1.9246E-02 -1.925E-02 8.113E-02 3.549E-09 1.945E-09
140.00 0.00 0.11691 1.3870E-01 -1.6215E-02 -1.621E-02 1.387E-01 1.278E-09 -6.238E-09
150.00 0.00 0.00662 1.9560E-01 -1.2942E-03 -1.294E-03 1.956E-01 -4.405E-09 3.582E-10
160.00 0.00 0.07326 2.4079E-01 1.7640E-02 1.764E-02 2.408E-01 -4.924E-09 3.527E-09
170.00 0.00 0.12045 2.6855E-01 3.2348E-02 3.235E-02 2.686E-01 8.082E-10 -4.232E-09
180.00 0.00 0.13599 2.7775E-01 3.7772E-02 3.777E-02 2.778E-01 -1.008E-09 1.213E-10
0.00 90.00 0.09758 4.2343E+00 -4.1320E-01 -4.132E-01 4.234E+00 -4.178E-08 -2.828E-09
10.00 90.00 0.10911 4.1162E+00 -4.4912E-01 -4.491E-01 4.116E+00 -3.930E-08 1.198E-08
20.00 90.00 0.14420 3.7701E+00 -5.4364E-01 -5.436E-01 3.770E+00 -3.597E-08 4.652E-09
30.00 90.00 0.20414 3.2267E+00 -6.5869E-01 -6.587E-01 3.227E+00 -2.834E-08 -9.660E-10
40.00 90.00 0.29034 2.5486E+00 -7.3995E-01 -7.400E-01 2.549E+00 -1.776E-08 1.966E-08
50.00 90.00 0.40271 1.8295E+00 -7.3678E-01 -7.368E-01 1.830E+00 -6.937E-09 4.586E-09
60.00 90.00 0.53656 1.1717E+00 -6.2868E-01 -6.287E-01 1.172E+00 -1.026E-09 1.203E-08
70.00 90.00 0.67801 6.5188E-01 -4.4198E-01 -4.420E-01 6.519E-01 -2.419E-09 6.202E-09
80.00 90.00 0.79934 2.9924E-01 -2.3919E-01 -2.392E-01 2.992E-01 7.830E-10 7.416E-09
90.00 90.00 0.85269 9.9116E-02 -8.4516E-02 -8.452E-02 9.912E-02 5.458E-10 1.582E-09
100.00 90.00 0.60400 1.5341E-02 -9.2659E-03 -9.266E-03 1.534E-02 -4.916E-10 9.156E-10
110.00 90.00 0.19961 1.0545E-02 -2.1049E-03 -2.105E-03 1.055E-02 1.321E-10 -6.863E-10
120.00 90.00 0.51133 5.3315E-02 -2.7261E-02 -2.726E-02 5.332E-02 3.564E-10 -1.670E-09
130.00 90.00 0.44323 1.1701E-01 -5.1864E-02 -5.186E-02 1.170E-01 9.436E-10 -6.678E-10
140.00 90.00 0.34103 1.7989E-01 -6.1350E-02 -6.135E-02 1.799E-01 -2.355E-10 1.092E-10
150.00 90.00 0.25177 2.2835E-01 -5.7491E-02 -5.749E-02 2.283E-01 2.310E-09 4.675E-10
160.00 90.00 0.18698 2.5853E-01 -4.8340E-02 -4.834E-02 2.585E-01 4.504E-09 5.089E-10
170.00 90.00 0.14861 2.7346E-01 -4.0639E-02 -4.064E-02 2.735E-01 3.817E-09 3.120E-10
180.00 90.00 0.13599 2.7775E-01 -3.7772E-02 -3.777E-02 2.778E-01 3.076E-09 -1.357E-10

```

B.2.3 wxxxryyykzzz.poln Files

The w000r000k000.pol1 file contains the polarization solution for the first wavelength (w000), first target radius (r00), first orientation (k000), and first incident polarization (pol1). In order to limit the size of this file, it has been written as an unformatted file.

B.3 DDFIELD files

B.3.1 Sample DDFIELD.in file

w000r000k000.pol1 = name of file with stored polarization

```

5.00e-3 = gamma (interaction cutoff parameter)
-35. 0. 0. = x/d, y/d, z/d
-34. 0. 0.
-33. 0. 0.
-32.5 0. 0.
-32.4 0. 0.
-32.3 0. 0.
-32.2 0. 0.
-32.1 0. 0.
-32. 0. 0.
-31.9 0. 0.
-31.8 0. 0.
-31.7 0. 0.
-31.6 0. 0.
-31.5 0. 0.
-31. 0. 0.
-30. 0. 0.
-29. 0. 0.

```

B.3.2 Sample DDfield.E file

When the DDFIELD is executed with the DDFIELD.in file presented above and one of the .pol files. It produces two output files DDFIELD.E and DDFIELD.B that contains electrical and magnetic field information respectively.

The DDfield.E file contains the electrical field information for each of the points described in DDFIELD.in.

```

12288 = number of dipoles in Target
Extent of occupied lattice sites
1 32 = JXMIN,JXMAX
1 24 = JYMIN,JYMAX
1 16 = JZMIN,JZMAX
-33.000000 0.000000 = (x_TF/d)min,(x_TF/d)max
-12.000000 12.000000 = (y_TF/d)min,(y_TF/d)max
-8.000000 8.000000 = (z_TF/d)min,(z_TF/d)max
-4.610482 0.000000 = xmin(TF),xmax(TF) (phys. units)
-1.676539 1.676539 = ymin(TF),ymax(TF) (phys. units)
-1.117693 1.117693 = zmin(TF),zmax(TF) (phys. units)
0.139712 = d (phys units)
0.000000 0.000000 = PYD,PZD = period_y/dy, period_z/dz
0.000000 0.000000 = period_y, period_z (phys. units)

```

```

6.283185 = wavelength in ambient medium (phys units)
0.139712 = k_x*d for incident wave
0.000000 = k_y*d for incident wave
0.000000 = k_z*d for incident wave
5.000E-03 = gamma (parameter for summation cutoff)
0.000000 0.000000 = (Re,Im)E_inc,x(0,0,0)
1.000000 0.000000 = (Re,Im)E_inc,y(0,0,0)
0.000000 0.000000 = (Re,Im)E_inc,z(0,0,0)
x/d y/d z/d ----- E_x ----- E_y ----- E_z -----
-35.0000 0.0000 0.0000 0.000000 0.000000 0.18730 0.79489 0.00000 0.00000
-34.0000 0.0000 0.0000 0.000000 0.000000 0.02038 0.80327 0.00000 0.00000
-33.0000 0.0000 0.0000 0.000000 0.000000 -0.15115 0.79529 0.00000 0.00000
-32.5000 0.0000 0.0000 0.000000 0.000000 -0.24115 0.79072 0.00000 0.00000
-32.4000 0.0000 0.0000 0.000000 0.000000 -0.26138 0.79303 0.00000 0.00000
-32.3000 0.0000 0.0000 0.000000 0.000000 -0.28379 0.79883 0.00000 0.00000
-32.2000 0.0000 0.0000 0.000000 0.000000 -0.31030 0.81135 0.00000 0.00000
-32.1000 0.0000 0.0000 0.000000 0.000000 -0.34557 0.83835 0.00000 0.00000
-32.0000 0.0000 0.0000 0.000000 0.000000 -0.38043 0.86434 0.00000 0.00000
-31.9000 0.0000 0.0000 0.000000 0.000000 -0.41426 0.88827 0.00000 0.00000
-31.8000 0.0000 0.0000 0.000000 0.000000 -0.44627 0.90876 0.00000 0.00000
-31.7000 0.0000 0.0000 0.000000 0.000000 -0.47560 0.92430 0.00000 0.00000
-31.6000 0.0000 0.0000 0.000000 0.000000 -0.50149 0.93347 0.00000 0.00000
-31.5000 0.0000 0.0000 0.000000 0.000000 -0.52359 0.93550 0.00000 0.00000
-31.0000 0.0000 0.0000 0.000000 0.000000 -0.62995 0.90101 0.00000 0.00000
-30.0000 0.0000 0.0000 0.000000 0.000000 -0.83356 0.80658 0.00000 0.00000
-29.0000 0.0000 0.0000 0.000000 0.000000 -1.01850 0.68353 0.00000 0.00000

```

APPENDIX C

FORTRAN CODES

C.1 The Fortran Code for BHMIE Algorithm

```
SUBROUTINE BHMIE(X,REFREL,NANG,S1,S2,QEXT,QSCA,QBACK,GSCA)
IMPLICIT NONE\\
C Declare parameters:\\
C Note: important that MXNANG be consistent with dimension of S1 and S2\\
C      in calling routine!\\

      INTEGER MXNANG,NMXX\\
C      PARAMETER(MXNANG=1000,NMXX=15000)\\
      PARAMETER(MXNANG=1000,NMXX=15000)\\

C Arguments:\\

      INTEGER NANG\\
      REAL GSCA,QBACK,QEXT,QSCA,X\\
      COMPLEX REFREL\\
      COMPLEX S1(2*MXNANG-1),S2(2*MXNANG-1)\\
C Local variables:\\

      LOGICAL SINGLE\\
      INTEGER J,JJ,N,NSTOP,NMX,NN\\
      DOUBLE PRECISION CHI,CHI0,CHI1,DANG,DX,EN,FN,P,PII,PSI,PSI0,PSI1,\\
      $$ THETA,XSTOP,YMOD\\
      DOUBLE PRECISION\\
      $$ AMU(MXNANG),\\
      $$ PI(MXNANG),\\
      & PI0(MXNANG),\\
      & PI1(MXNANG),\\
```

```

& TAU(MXNANG)\
DOUBLE COMPLEX\
& DCXS1(2*MXNANG-1),\
& DCXS2(2*MXNANG-1)\

C*****\
C\
C Subroutine BHMIE is derived from the Bohren-Huffman Mie scattering\
C   subroutine to calculate scattering and absorption by a homogenous\
C   isotropic sphere.\
C Given:\
C   X = 2*pi*a/lambda\
C   REFREL = (complex refr. index of sphere)/(real index of medium)\
C   NANG = number of angles between 0 and 90 degrees\
C           (will calculate 2*NANG-1 directions from 0 to 180 deg.)\
C           if called with NANG<2, will set NANG=2 and will compute\
C           scattering for theta=0,90,180.\
C Returns:\
C   S1(1 - 2*NANG-1) = -i*f_22 (incid. E perp. to scatt. plane,\
C                               scatt. E perp. to scatt. plane)\
C   S2(1 - 2*NANG-1) = -i*f_11 (incid. E parr. to scatt. plane,\
C                               scatt. E parr. to scatt. plane)\
C   QEXT = C_ext/pi*a**2 = efficiency factor for extinction\
C   QSCA = C_sca/pi*a**2 = efficiency factor for scattering\
C   QBACK = 4.*pi*(dC_sca/domega)/pi*a**2
C           = backscattering efficiency
C   GSCA = <cos(theta)> for scattering
C
C S1 and S2 are the diagonal elements of the "amplitude scattering matrix"
C (see eq. 3.12 of Bohren & Huffman 1983) -- the off-diagonal elements
C vanish for a spherical target.
C For unpolarized incident light, the intensity of scattered light a
C distance r from the sphere is just
C
C   1
C   I_s = ----- * I_in * S_11
C         (kr)^2
C
C where k=2*pi/lambda
C and the "Muller matrix element" S_11 = 0.5*( |S_1|^2 + |S_2|^2 )
C

```

C for incident light polarized perp to the scattering plane,
C the scattered light is polarized perp to the scattering plane
C with intensity $I_s = I_{in} * |S_1|^2 / (kr)^2$
C
C for incident light polarized parallel to the scattering plane,
C the scattered light is polarized parallel to the scattering plane
C with intensity $I_s = I_{in} * |S_2|^2 / (kr)^2$
C
C History:
C Original program taken from Bohren and Huffman (1983),
C Modified by B.T.Draine, Princeton Univ. Obs., 90.10.26
C in order to compute <cos(theta)>
C 91.05.07 (BTD): Modified to allow NANG=1
C 91.08.15 (BTD): Corrected error (failure to initialize P)
C 91.08.15 (BTD): Modified to enhance vectorizability.
C 91.08.15 (BTD): Modified to make NANG=2 if called with NANG=1
C 91.08.15 (BTD): Changed definition of QBACK.
C 92.01.08 (BTD): Converted to full double precision and double complex
C eliminated 2 unneed lines of code
C eliminated redundant variables (e.g. APSI,APSI0)
C renamed RN -> EN = double precision N
C Note that DOUBLE COMPLEX and DCMLX are not part
C of f77 standard, so this version may not be fully
C portable. In event that portable version is
C needed, use src/bhmie_f77.f
C 93.06.01 (BTD): Changed AMAX1 to generic function MAX
C 98.09.17 (BTD): Added variable "SINGLE" and warning in event that
C code is used with single-precision arithmetic (i.e.,
C compiler does not support DOUBLE COMPLEX)
C 99.02.17 (BTD): Replaced calls to REAL() and IMAG() by
C REALPART() and IMAGPART() for compatibility with g77
C Note that when code is used with standard f77
C compilers, it is now necessary to enable two lines
C defining functions REALPART(X) and IMAGPART(X)
C 99.02.19 (BTD): added lines to be enabled to properly define
C REALPART() and IMAGPART() if NOT using g77
C ***see below!***
C 01.02.16 (BTD): added IMPLICIT NONE
C 01.02.27 (BTD): changed definition of QBACK back to convention of
C Bohren & Huffman and others:

```

C          Q_back = 4.*pi*(dC_sca/dOmega)/(pi*a^2) in backward
C          direction
c 02.03.09 (BTD): defined statement function REALPART_SP to
c          avoid warning regarding type conversion when taking
c          real part of S1(1) to evaluate QEXT
c          some cleanup regarding type conversion
c 02.05.30 (BTD): introduced internal double complex arrays DCXS1,DCXS2
c          to possibly increase accuracy during summations.
c          After summations, output scattering amplitudes
c          via single complex arrays S1,S2 as before.
c          Usage of this routine is unaffected by change.
c          Note: no longer need statement function REALPART_SP
c 02.09.18 (BTD): Error in evaluation of QBACK reported by Okada Yasuhiko
c          Was calculating QBACK using S1 rather than DCXS1
c          Corrected.
c 02.10.16 (BTD): Added comments explaining definition of S_1 and S_2 .
C end history
C
C*****
C
C This module is dependent on whether compiler supports double precision
C complex variables:
C
C If your compiler does NOT support double complex, comment out following
C three lines, and uncomment corresponding 3 lines further below
C
      DOUBLE COMPLEX AN,AN1,BN,BN1,DREFRL,XI,XI1,Y
      DOUBLE COMPLEX D(NMXX)
      PARAMETER(SINGLE=.FALSE.)

C      COMPLEX AN,AN1,BN,BN1,DREFRL,XI,XI1,Y
C      COMPLEX D(NMXX)
C      PARAMETER(SINGLE=.TRUE.)

C*****

C Following five statements should be enabled if NOT using g77.
C They assume that the compiler supports double complex, since the
C statements DBLE and DIMAG are used. If double complex is not available
C (see above) you will need to change DIMAG to AIMAG

```

```

C
C If using g77, following statements could be commented out, as
C REALPART and IMAGPART are g77 intrinsic functions
C However, they do not need to be commented out.

      DOUBLE COMPLEX DPCX
      DOUBLE PRECISION REALPART
      DOUBLE PRECISION IMAGPART
      REALPART(DPCX)=(DBLE(DPCX))
      IMAGPART(DPCX)=(DIMAG(DPCX))
C*****
C*** Safety checks
      IF(SINGLE)WRITE(0,*)'Warning: this version of bhmie uses only ',
&      'single precision complex numbers!'
      IF(NANG.GT.MXNANG)STOP'***Error: NANG > MXNANG in bhmie'
      IF(NANG.LT.2)NANG=2
C*** Obtain pi:
      PII=4.D0*ATAN(1.D0)
      DX=X
      DREFRL=REFREL
      Y=X*DREFRL
      YMOD=ABS(Y)
C*** Series expansion terminated after NSTOP terms
C   Logarithmic derivatives calculated from NMX on down
      XSTOP=X+4.*X**0.3333+2.
      NMX=NINT(MAX(XSTOP,YMOD))+15
C   BTd experiment 91.1.15: add one more term to series and compare results
C   NMX=MAX(XSTOP,YMOD)+16
C   test: compute 7001 wavelengths between .0001 and 1000 micron
C   for a=1.0micron SiC grain. When NMX increased by 1, only a single
C   computed number changed (out of 4*7001) and it only changed by 1/8387
C   conclusion: we are indeed retaining enough terms in series!
      NSTOP=NINT(XSTOP)
      IF(NMX.GT.NMXX)THEN
          WRITE(0,*)'Error: NMX > NMXX=',NMXX,' for |m|x=',YMOD
          STOP
      ENDIF
C*** Require NANG.GE.1 in order to calculate scattering intensities
      DANG=0.
      IF(NANG.GT.1)DANG=.5*PII/DBLE(NANG-1)

```

```

DO J=1,NANG
  THETA=DBLE(J-1)*DANG
  AMU(J)=COS(THETA)
ENDDO
DO J=1,NANG
  PI0(J)=0.
  PI1(J)=1.
ENDDO
NN=2*NANG-1
DO J=1,NN
  DCXS1(J)=(0.D0,0.D0)
  DCXS2(J)=(0.D0,0.D0)
ENDDO
C*** Logarithmic derivative D(J) calculated by downward recurrence
C beginning with initial value (0.,0.) at J=NMX
  D(NMX)=(0.,0.)
  NN=NMX-1
  DO N=1,NN
    EN=NMX-N+1
    D(NMX-N)=(EN/Y)-(1./(D(NMX-N+1)+EN/Y))
  ENDDO
C*** Riccati-Bessel functions with real argument X
C calculated by upward recurrence
  PSI0=COS(DX)
  PSI1=SIN(DX)
  CHI0=-SIN(DX)
  CHI1=COS(DX)
  XI1=DCMPLX(PSI1,-CHI1)
  QSCA=0.E0
  GSCA=0.E0
  P=-1.
  DO N=1,NSTOP
    EN=N
    FN=(2.E0*EN+1.)/(EN*(EN+1.))
C for given N, PSI = psi_n      CHI = chi_n
C           PSI1 = psi_{n-1}    CHI1 = chi_{n-1}
C           PSI0 = psi_{n-2}    CHI0 = chi_{n-2}
C Calculate psi_n and chi_n
  PSI=(2.E0*EN-1.)*PSI1/DX-PSI0
  CHI=(2.E0*EN-1.)*CHI1/DX-CHI0

```

```

        XI=DCMPLX(PHI,-CHI)
C*** Store previous values of AN and BN for use
C   in computation of g=<cos(theta)>
        IF(N.GT.1)THEN
                AN1=AN
                BN1=BN
        ENDIF
C*** Compute AN and BN:
        AN=(D(N)/DREFRL+EN/DX)*PHI-PHI1
        AN=AN/((D(N)/DREFRL+EN/DX)*XI-XI1)
        BN=(DREFRL*D(N)+EN/DX)*PHI-PHI1
        BN=BN/((DREFRL*D(N)+EN/DX)*XI-XI1)

C*** Augment sums for Qsca and g=<cos(theta)>

        QSCA=QSCA+REAL((2.*EN+1.)*(ABS(AN)**2+ABS(BN)**2))
        GSCA=GSCA+REAL(((2.*EN+1.)/(EN*(EN+1.)))*
&      (REALPART(AN)*REALPART(BN)+IMAGPART(AN)*IMAGPART(BN)))
        IF(N.GT.1)THEN
                GSCA=GSCA+REAL(((EN-1.)*(EN+1.)/EN)*
&      (REALPART(AN1)*REALPART(AN)+IMAGPART(AN1)*IMAGPART(AN)+
&      REALPART(BN1)*REALPART(BN)+IMAGPART(BN1)*IMAGPART(BN)))
        ENDIF
C*** Now calculate scattering intensity pattern
C   First do angles from 0 to 90
        DO J=1,NANG
                JJ=2*NANG-J
                PI(J)=PI1(J)
                TAU(J)=EN*AMU(J)*PI(J)-(EN+1.)*PI0(J)
                DCXS1(J)=DCXS1(J)+FN*(AN*PI(J)+BN*TAU(J))
                DCXS2(J)=DCXS2(J)+FN*(AN*TAU(J)+BN*PI(J))
        ENDDO
C*** Now do angles greater than 90 using PI and TAU from
C   angles less than 90.
C   P=1 for N=1,3,...; P=-1 for N=2,4,...
        P=-P
        DO J=1,NANG-1
                JJ=2*NANG-J
                DCXS1(JJ)=DCXS1(JJ)+FN*P*(AN*PI(J)-BN*TAU(J))
                DCXS2(JJ)=DCXS2(JJ)+FN*P*(BN*PI(J)-AN*TAU(J))

```

```

        ENDDO
        PSI0=PSI1
        PSI1=PSI
        CHI0=CHI1
        CHI1=CHI
        XI1=DCMPLX(PSI1,-CHI1)
C*** Compute pi_n for next value of n
C   For each angle J, compute pi_{n+1}
C   from PI = pi_n , PI0 = pi_{n-1}

        DO J=1,NANG
            PI1(J)=((2.*EN+1.)*AMU(J)*PI(J)-(EN+1.)*PI0(J))/EN
            PI0(J)=PI(J)
        ENDDO
    ENDDO
C*** Have summed sufficient terms.
C   Now compute QSCA,QEXT,QBACK,and GSCA

        GSCA=REAL(2.D0*GSCA/QSCA)
        QSCA=REAL((2.D0/(DX*DX))*QSCA)
        QEXT=REAL((4.D0/(DX*DX))*REALPART(DCXS1(1)))
        QBACK=REAL(4.D0*(ABS(DCXS1(2*NANG-1))/DX)**2)
C prepare single precision complex scattering amplitude for output

        DO J=1,2*NANG-1
            S1(J)=CMLPX(DCXS1(J))
            S2(J)=CMLPX(DCXS2(J))
        ENDDO
    RETURN
END

```